

NANOSTRUCTURED MAGNETIC RECORDING MEDIA BY PATTERNING
AND GLANCING ANGLE DEPOSITION

by

HAO SU

SUBHADRA GUPTA, COMMITTEE CHAIR

DAWEN LI
JINHUI SONG
MARK L. WEAVER
DERRICK R. DEAN

A DISSERTATION

Submitted in partial fulfillment of the requirements
for the degree of Doctor of Philosophy
in the Department of Metallurgical and Materials Engineering
in the Graduate School of
The University of Alabama

TUSCALOOSA, ALABAMA

2014

Copyright Hao Su 2014
ALL RIGHTS RESERVED

ABSTRACT

In order to solve the trilemma problems that perpendicular magnetic recording is facing, advanced approaches such as heat assisted magnetic recording and bit patterned media are being intensively researched. In this work, high coercivity magnetic materials have been studied in the form of nanostructured Co/Pd and FeB/Pt multilayers. Arrays of uniformly spaced nanopillars over large areas were formed by utilizing block copolymer patterning. Uniform nanorods were formed by glancing angle deposition, a unique single-step approach to bit-patterned media.

First, a detailed study on Co/Pd multilayered thin films was carried out to optimize the magnetic properties with respect to the thickness ratio, number of bilayers and seed layers. Then a statistical optimization of the patterning of Co/Pd multilayers by nanosphere lithography and block copolymer templating was carried out. The highest measured perpendicular anisotropy for Co/Pd films was 2.8×10^6 ergs/cm³. However, many of the M-H loops for Co/Pd were not saturated at the maximum field of 18 kOe, so the perpendicular anisotropy approaches 10^7 ergs/cm³. A unique single-step approach to nanostructuring these Co/Pd multilayers was developed: glancing angle deposition (GLAD), which produced Co/Pd nanorods with a coercivity as high as 2.9 kOe, a 123% increase over the flat multilayers.

For deposition of FeBPt based granular media, two different techniques were used to sputter FeB/Pt multilayers. A finely alternated layered structure was proven to be more effective in forming L1₀ structured B-doped FePt. The FeBPt films thus formed were also patterned by block copolymer templating, and their magnetic properties were studied as a function of ion milling and annealing conditions. The highest coercivity achieved for patterned and annealed B-doped FePt films was 14 kOe.

DEDICATION

This dissertation is dedicated to my family and friends who stood by me through this dissertation journey.

LIST OF ABBREVIATIONS AND SYMBOLS

<i>HDD</i>	Hard disk drive
<i>LMR</i>	Longitudinal magnetic recording
<i>PMR</i>	Perpendicular magnetic recording
<i>HAMR</i>	Heat assisted magnetic recording
<i>BPM</i>	Bit patterned media
<i>NSL</i>	Nanosphere lithography
<i>BCP</i>	Block copolymer templating
<i>GLAD</i>	Glancing angle deposition
<i>RIE</i>	Reactive ion etching
<i>MLs</i>	Multilayers
<i>PMA</i>	Perpendicular magnetic anisotropy
<i>AGM</i>	Alternating gradient magnetometer
<i>AFM</i>	Atomic force microscopy
<i>EDX</i>	Energy dispersive x-ray spectrum
<i>SEM</i>	Scanning electron microscope
<i>XRD</i>	X-ray diffraction
<i>XRR</i>	X-ray reflection
<i>SQUID</i>	Superconducting quantum interference device
<i>FIB</i>	Focused ion beam
<i>TEM</i>	Transmission electron microscope
<i>PPMS</i>	Physical Property Measurement System
<i>RTA</i>	Rapid thermal anneal
M_s	Saturation magnetization
M_r	Remanent magnetization
M_{eff}	Effective magnetization
S^*	Squareness

H_c	Coercive field
H	Applied magnetic field
H_k	Anisotropic field
SFD	Switching field distribution
β	full width at half maximum
θ	Incidence angle of X-ray
h	Planck's constant
d	Lattice spacing
k_B	Boltzmann constant
K_u	Anisotropy constant
K_u^{avg}	Average anisotropy constant
K_u^{bulk}	Bulk anisotropy constant

ACKNOWLEDGMENTS

I would like to take this opportunity to thank all of the people without whom the past few years would not have been possible and would certainly not have been so enjoyable. If I miss anyone out in this list of acknowledgments, my apologies.

First of all, I would like to thank my advisor, Professor Subhadra Gupta, for her continual guidance, encouragement, support and enthusiasm during the study and research and for the provision of excellent research facilities. The discussion with her was invaluable and guided me to passionately explore amazing science in this topic.

I would also like to thank my dissertation committee members Dr. Mark L. Weaver, Dr. Dawen Li, Dr. Jinhui Song, and Dr. Derrick R. Dean for their time, help and effort of serving in my committee.

I would like to thank Dr. Alton Highsmith and Dr. Anusha Natarajarathinam for their critical training while working in the UA-MFF lab. Thanks go to UA-MFF members, Mr. Billy Clark, Mr. Allen Owen, Mr. Amrital Singh, Mr. Samuel Schwarm, Mr. Robert Douglas, Ms. Angelique Montgomery, Mr. Tyler Miller, and Mr. Michael Carton for all their help in measurements, processing, valuable discussion and friendly support. Thanks also go to Z. Sun, X. Xu, Z. He and S. Keshavarz for valuable discussion and friendly support.

Mr. Rich Martens, Mr. Johnny Goodvin, Mr. John Hawkins, Mr. Jonathon Fink and Mr. Danny Whitcomb are acknowledged for their help on numerous occasions on the FIB, and for equipment issues in MINT and UA-MFF. G.Mankey and P.LeClair are acknowledged for the use of their customer built vacuum annealer. J. Song and C.Tang are acknowledged for the help and measurements of their AFM. Ms. Li Wan is thanked for help on TEM sample preparation.

I would like to acknowledge the financial supports from ECCS GOALI: NANOPATTERNED MEDIA (NSF ECCS 0901858) and DMREF project and teaching assistantship from Department of Metallurgical and Materials Engineering.

I would like to thank the faculty, staff and students of the Department of Metallurgical and Materials Engineering and Center for Materials for Information Technology (MINT) for the academic and technical support.

Finally, I would like to express my deepest love to my wife Yao who has encouraged and supported me. I would also like to express gratitude to my mother for her unconditional love and brother who never stopped encouraging me to persist.

CONTENTS

ABSTRACT	ii
DEDICATION.....	iii
LIST OF ABBREVIATIONS AND SYMBOLS	iv
ACKNOWLEDGMENTS	vi
LIST OF TABLES	xii
LIST OF FIGURES	xiii
Chapter 1 Introduction	1
1.1 Magnetic Recording.....	1
1.1.1Trilemma of Perpendicular Magnetic Recording	2
1.1.2 Heat Assisted Magnetic Recording (HAMR).....	3
1.1.3 Bit Patterned Media (BPM) by Conventional Method.....	6
1.1.4 Bit Patterned Media (BPM) by Glancing Angle Deposition (GLAD).....	8
1.1.5 Thin film Nucleation and Growth.....	9
1.2 Proposed Research Objectives	12
1.3 Dissertation Outline	13
Chapter 2 Experimental Techniques.....	14
2.1. Introduction	14
2.2 Fabrication Techniques	15
2.2.1 Sputtering.....	15
2.2.2 Plasma Treatment.....	16
2.2.3. Ion Milling	17
2.3 Morphologies and Structural Characterization	19

2.3.1 Atomic Force Microscopy (AFM)	19
2.3.2 Scanning Electron Microscopy (SEM).....	20
2.3.4 X-ray Diffraction/Reflectivity (XRD/XRR).....	21
2.3.5 Transmission Electron Microscopy.....	22
2.4 Magnetic Characterization	24
2.4.1. Alternating Gradient Magnetometer (AGM)	24
2.4.2 Superconducting Quantum Interference Device (SQUID) Magnetometer	25
Chapter 3 Co/Pd Multilayered Continuous Film.....	27
3.1 Introduction	27
3.2 Experiments.....	27
3.3 Results and Discussion	28
3.3.1 Magnetic Property Dependence on Co and Pd Thickness.....	28
3.3.1.1 Co thickness fixed, Pd thickness varied.....	28
3.3.1.2 Pd thickness fixed, Co thickness varied.....	29
3.3.2 Effect of Seed Layers	32
3.3.3 Effect of Bilayer Numbers.....	34
3.3.4 Same Total Thickness Same Thickness Ratio, Bilayer Number Varied	35
3.3.5 Same Thickness Ratio, Same Bilayer Number, Bilayer Thickness Varied.....	36
3.4 Conclusions	37
Chapter 4 Nanopatterned Media by Nanosphere Lithography and Block Copolymer Lithography.....	38
4.1 Introduction	38
4.2 Experiments.....	39
4.3 Results and Discussion	40

4.3.1 Nanosphere Lithography	40
4.3.1.1 PS Self-assembly	41
4.3.1.2 Plasma Treatment	42
4.3.1.3 Pattern Transfer to Magnetic Layer	47
4.3.1.4 Magnetic Properties	47
4.3.2 Block Copolymer Assembly.....	49
4.3.2.1 Exposing PFS by Plasma	50
4.3.2.2 Pattern Transfer	50
4.3.2.3 Magnetic Properties	54
4.3.3 CoPt Patterned by BCP	57
4.3.4 Co/Pd MLs on PSS.....	58
4.4 Conclusions	60
Chapter 5 Nanorods Fabricated by Glancing Angle Deposition	62
5.1 Introduction	62
5.2 Experiments.....	63
5.3 Result and Discussion	64
5.3.1 CoPt-AlN	64
5.3.2 Co/Pd Multilayered Nanorods	67
5.3.3 Co/Pd Nanocolumn on Nanospheres.....	74
5.3.4 FeB/Pt Multilayered Nanorods and FeBPt Composite Nanorods.....	76
5.3.5 Co Nanorods	81
5.4 Conclusions	81
Chapter 6 Microstructure Evolution and Magnetic Properties of Fe(B)/Pt Multilayered and Fe(B)Pt Thin Film	83

6.1 Introduction	83
6.2 Experiments.....	83
6.3 Results and Discussion	86
6.3.1 Sequential and Co-sputtered FeB/Pt Multilayered Sample	86
6.3.1.1 Structural and Magnetic Properties of Sample Series A and B FeB/Pt Multilayered Films Annealed at 550 °C vs. Annealing Time.	86
6.3.1.2 Structural and Magnetic Properties of Sample Series A and B FeB/Pt Multilayered Films Annealed for one hour vs. Annealing Temperature.	88
6.3.1.3 Structural and Magnetic Properties of FeB/Pt Multilayered Films Annealed for one hour vs. Film Thickness.	92
6.3.2 Exchange Coupled Composite	94
6.3.3 Exploring Conditions for Fe/Pt Multilayers	96
6.4 Conclusions	99
Chapter 7 FeBPt Patterned by Block Copolymer Lithography	101
7.1 Introduction	101
7.2 Experiments.....	101
7.3 Results and Discussion	103
7.3.1 Series 1: Annealing to Form FeBPt after Patterning.....	103
7.3.2 Series 2 Annealing to Form FeBPt before Patterning	107
7.4 Conclusions	109
Chapter 8 Conclusions and Future Work	110
8.1 Conclusions	110
8.2 Future Work	113
References.....	114

LIST OF TABLES

Table 3. 1 Switching field distribution of Co/Pd MLs with various seed layers.....	33
Table 5. 1 Summary of squareness and coercivity of GLAD samples and Control samples.....	66
Table 5. 2 FeB/Pt sample details and annealing conditions	77
Table 6. 1 Sample list with details of stacks, processing conditions and analysis	85

LIST OF FIGURES

Figure 1. 1 Areal density trends for hard disk drives [Ref.9]	1
Figure 1. 2 Trilemma of Perpendicular Magnetic Recording [Ref. 9]	3
Figure 1. 3 Schematic of additive (prepattern and deposition) and subtractive (deposition and etching) patterning [Ref. 42]	8
Figure 1. 4 Archetypal GLAD fabricated microstructures, (a) tilted columns, (b) zig-zag columns, (c) helical columns, and (d) vertical columns. [Ref.52]	9
Figure 1. 5 Basic modes of thin-film growth [Ref. 67, 68]	10
Figure 1. 6 Structure zone model by Movchan and Demchishin. [Ref. 69]	11
Figure 1. 7 Schematic of nanorods growth by glancing angle deposition	12
Figure 2. 1 (a) Photo and (b) schematic of SFI Shamrock sputtering system in UA-MFF [Ref. 71].....	15
Figure 2. 2 Schematic of S-gun cathode assembly in Shamrock sputtering system. [Ref 72]	16
Figure 2. 3 Photo of STS-AOE and schematic of ICP etching chamber of STS_AOE [Ref. 73,74].....	17
Figure 2. 4 Intelvac ion-mill system in UA-MFF [Ref. 72]	18
Figure 2. 5 Photo (a) and schematic (b) of AFM [Ref. 76]	19
Figure 2. 6 (a) Photo of JEOL 7000F SEM and (b) schematic of its components [Ref. 71]	20
Figure 2. 7 (a) Philips X-ray diffractometer [Ref.79] and (b) its schematic [Ref. 80]	22
Figure 2. 8 Schematic of TEM show two basic operations of the TEM imaging system (a) diffraction mode and (b) image mode. [Ref. 81]	23
Figure 2. 9 (a) FIB (FEI Quanta 3D Dual Beam) in CAF and (b) demo procedure of TEM sample prepared by FIB [Ref. 82].	24
Figure 2. 10 (a) Princeton alternating gradient magnetometer [79] and (b) its schematic [83]	25
Figure 2. 11 (a) Quantum design -magnetic properties measurement system [Ref. 79] and (b) its schematic illustration [Ref. 84]	26

Figure 3. 1 Out-of-plane M-H loops of Co/Pd MLs with stacks of Ta5 /Pd5 /[Co0.2/Pd t_{Pd}] ₉ /Ta5 , where t_{Pd} varied from 0.4 to 1.2 nm	29
Figure 3. 2 H_c and S^* extracted from M-H loops of samples Ta5/Pd5/[Co t_{Co} /Pd t_{Pd}] ₉ /Ta5 , where t_{Co} varied from 0.2 to 0.45 nm and t_{Pd} varied from 0.4 to 1.2 nm.	29
Figure 3. 3 Out of plane (a) and in-plane (b) hysteresis loops of CPMLs with stack of Ta5/Pd5/[Co t_{Co} /Pd 0.4] ₉ /Ta5, where t_{Co} ranged from 0.2 to 0.45 nm. (c) showed K_u dependence on t_{Co}	30
Figure 3. 4 Plots of H_c (e) and M_{st} (f) for all the stacks of Ta5/Pd5/[Co t_{Co} /Pd t_{Pd}] ₉ /Ta5 where t_{Co} varied from 0.2 to 0.45and t_{Pd} from 0.4 to 1.2 nm.....	31
Figure 3. 5 Contour plot of coercivity H_c vs. thickness of Co and Pd	31
Figure 3. 6 (a) M-H loops and (b) SFD of Co/Pd MLs with different seed layers	32
Figure 3. 7 (a) XRD and (b) XRR spectra of CPMLs with different seeds.	33
Figure 3. 8 (a) Out of plane hysteresis loops of Co/Pd MLs with different bilayer numbers. (b) H_c and M_{st} dependence on bilayer numbers.....	34
Figure 3. 9 XRR spectra of CPMLs of Ta5/Pd5/[Co0.3/Pd1.0] _N /Ta5 with different bilayer number.....	35
Figure 3. 10 (a) Out-of-plane M-H loops of Co/Pd ML with different bilayer thickness and bilayer number. (b) The dependence of H_c on bilayer number and bilayer thickness.	36
Figure 3. 11 Out-of-plane M-H loops of Co/Pd ML with 20 bilayers but different bilayer thickness	36
Figure 4. 1 Schematic of nanodots fabrication by NSL. a) Depositing magnetic thin film; b) spin-coating monolayers of PS; c) tuning the PS size by RIE or O ₂ plasma ashing; d) Etching the film by RIE or ion-milling.....	41
Figure 4. 2 Typical SEM image of a closely packed monolayer of PS with diameter of 900nm, the inset is the SEM image at higher magnification of 12000. Scale bars are in 1 μm	41
Figure 4. 3 SEM images of 900nm PSS by oxygen plasma treatment of periods from 10s to 12 minutes at 80W, (a) 10s, (b) 30s, (c)60s,(d) 90s(e) 2minutes, (f) 4 minutes, (h) 8 minutes and (i) 12 minutes. All the scale bars are 1 μm	42
Figure 4. 4 Diameter variation of PS as a function of ashing time. The inset showed the variation of the PSS size normalized by the initial size as a function of O ₂ plasma time.	43
Figure 4. 5 SEM images of 900 nm PS beads treated by RIE with O ₂ at 350W for (a) 10s (b)20s (c)40s (d)60s (e)90s (f)120s (g)180s (h)240s and (i)300s. All the scale bars are 1 μm	44

Figure 4. 6 Size variations of PSS as a function of RIE time. The inset shows the size variation normalized by the initial size as a function of time.	45
Figure 4. 7 SEM images of 300 nm PS beads treated by RIE with O ₂ at 350W/0W for (a) 0s (b) 30s (c) 1min and (d) 2 min.	46
Figure 4. 8 Size variations as a function of RIE time.	46
Figure 4. 9 Side-view of SEM image of the sample with stacks of Pd 10/ [Co0.3 /Pd1.0] ₉ /Pt 5 nm etched at 50°,14W for 7 minute after 4 minutes' ashing in the oxygen plasma.	47
Figure 4. 10 Out-of-plane of M-H loops of (a) continuous film and (b) patterned film with stacks of Pd 10nm/[Co0.3 nm/Pd1.0nm] _{x9} /Pt 5nm	48
Figure 4. 11 Contour plots of coercivity as a function of beam power and etch angle.....	48
Figure 4. 12 Schematic of nanodots fabrication by BCP. a) Depositing magnetic thin film; b) spin-coating BCP of PS-b-PFS; c) Annealing to cause phase separation d) Exposing PFS spheres by RIE or O ₂ plasma; e) Etching the film by RIE or ion-milling.....	49
Figure 4. 13 SEM images of PS-PFS treated by RIE for (a) 5s, (b) 10s, (c) 15s and (d) 4 minutes, and by oxygen plasma asher for (e) 45s and (d)90s.	50
Figure 4. 14 SEM images of Co/Pd multilayered sample after etching at beam voltage 300V and etch angle of 55° and M-H loops for the same sample before and after ion-milling.	51
Figure 4. 15 DoE contour plot showing coercivity as a function of beam voltage and etch angle.	52
Figure 4. 16 SEM images of sample with stack of Ta5/Pd5/[Co0.3/Pd1.0] ₁₄ /Ta5 after ion-milled at 55° for (a)(d) 2minutes (b) (e) 2.5 minutes and (c)(f) 3 minutes . (a) (b) (c) are top-view and (d)(e)(f) are tilt-view. The inset in (c) shows the size distribution.	53
Figure 4. 17 SEM images of sample with stack of Ta5/Pd5/[Co0.25/Pd0.83] ₁₁ /Ta5 after ion-milled at 55° for (a) (d) 2minutes (b) (e) 2.5 minutes and (c) (f) 3 minutes. (a) (b) (c) are top-view and (d) (e) (f) are tilt-view. All the scale bars were 100nm.....	53
Figure 4. 18 (a) Top view and (b) tilt-view SEM micrograph of CPMLs with stack of Ta5/Pd5/[Co0.3/Pd1.0] ₂₀ /Ta5 after ion milling for 4 min.....	54
Figure 4. 19 (a) Out-of-plane and (b) H _c of samples with stack of Ta5/Pd5/[Co0.3/Pd1.0] ₁₄ /Ta5 as a function of etching time by ion-milling at 55°.	55
Figure 4. 20 (a) M-H loops and (b) H _c of samples with stack of Ta5/Pd5/[Co0.25/Pd0.83] ₁₁ /Ta5 as a function of etching time by ion-milling at 55°.	55
Figure 4. 21 Coercivity of ion milled samples before and after annealing as a function of ion milling etch time.	56

Figure 4. 22 (a) SEM image of CoPt dot array patterned with PFS-PS by ion-milling 45°-2min-80°-5min (b) out of plane M-H loops of as-deposited film, (c) out of plane and (d) in plane hysteresis loops of patterned sample.....	58
Figure 4. 23 SEM images of Co/Pd MLs on the PS which were ashed by oxygen plasma for (a) 0 s (b) 10s (c) 60s and (d) 120s.	58
Figure 4. 24 (a) out-of-plane M-H loops of Co/Pd MLs with stack of Ta5/Ru10/[Co0.5/Pd0.5] ₉ /Ta5 deposited on 900 nm PSS ashed for various time. (b) H _c as a function of ashing time; (c) H _c vs. PS diameter, corresponding to ashing time in (b).....	60
Figure 5. 1 Side-view SEM of GLAD samples of a) Ru 50/CoPt 350 nm and b) Ru 50/CoPt-AlN 350nm. The inset in Figure 5.1b showed nanorods in high magnification of 150,000.	64
Figure 5. 2 Side-view SEM of GLAD sample of Ta 5nm /Ru 50nm /CoPt-AlN(t nm)/Ta 5nm. (a) t=52 (b)t=39 (c) t=26	65
Figure 5. 3 EDX spectrum and composition of Ta 5nm /Ru 50nm /CoPt-AlN(39 nm)/Ta 5nm .	66
Figure 5. 4 (a) Out-of-plane and (b) in-plane of hysteresis loop normally deposited sample (t=39) and (c) out-of-plane and (d) in-plane of hysteresis loops of GLAD sample (t=39)	67
Figure 5. 5 SEM images of (a) and (d) side, (b) and (e) top, (c) and (f) cross sectional views of GLAD and normally deposited Co/Pd multilayered samples, respectively; (g) nanorod diameter distribution from Figure 5.5 b.	68
Figure 5. 6 AFM images of (a) normally deposited and (b) GLAD Co/Pd multilayered samples.....	69
Figure 5. 7 XRR spectra for normally deposited (○) and GLAD (■) Co/Pd multilayered samples.....	70
Figure 5. 8 X-ray θ -2 θ scan for normally deposited (○) and GLAD (■) Co/Pd multilayered samples.....	71
Figure 5. 9 Out-of-plane hysteresis loops for normally deposited (○) and GLAD (■) Co/Pd multilayered samples measured by AGM.	72
Figure 5. 10 Out of plane M-H loops of GLAD Co/Pd multilayered films with various thickness and bilayer number as indicated in the plot. Figure 5.10 d showed H _c extracted from b as a function of Co thickness.	73
Figure 5. 11 SEM images of nano-columns grown on PFS nanospheres and bare silicon. (a) Cross-sectional view and (b) plan-view on PFS nanospheres, (c) cross-sectional view and (d) plan-view SEM images on silicon. The inset pictures are corresponding pictures at high magnification. All the scale bars are in 100 nm.	75

Figure 5. 12 M-H loops of Co/Pd GLAD samples with stack of Ta5/Pd5/[Co0.3/Pd1.0]_{x20}/Ta5 (thickness in nm) deposited on the silicon substrates and PFS nanospheres, respectively. For comparison, the M-H loop of normally deposited sample with same stack was also plotted.....76

Figure 5. 13 SEM images of GLAD samples. Top-view of (a) GLAD-A as-deposited (b) GLAD-A 600°C1hr annealed and (c) GLAD-B as-deposited. (b)(d)(f) are corresponding tilt-view images.78

Figure 5. 14 In-plane M-H loops of (a) sample GLAD-A vs. annealing time at 550°C (b) GLAD-A annealed at different temperature (c) GLAD-B annealed at 550°C for different time and (d) GLAD-B annealed at different temperature for 1hr. (e) and (f) are coercivities extracted from (a)-(d) as functions of annealing time and annealing temperature, respectively.80

Figure 5. 15 In-plane M-H loops of (a) sample Normal-A vs. annealing time at 550°C (b) Normal-A annealed at different temperature (c) Normal-B annealed at 550°C for different time and (d) Normal-B annealed at different temperature for 1hr. (e) and (f) are coercivities extracted from (a)-(d) as functions of annealing time and annealing temperature, respectively.80

Figure 5. 16 Side-view SEM images of Co sputtered for 40min at 300W (a) stationary deposition and (b) planetary deposition81

Figure 6. 1 XRD patterns of (a) sample A and (b) sample B annealed at 550°C for various time (c) Grain size calculated by Sherrer equation as functions of annealing time for samples A and B.86

Figure 6. 2 In-plane magnetization curves of (a) sample A and (b) sample B annealed at 550°C for 0, 6,15,30 min and 1hr, respectively. (c) The dependence of Hc on annealing time at 550°C.....87

Figure 6. 3 XRD patterns of (a) sample A and (b) sample B annealed for 1hr for various temperatures, (c) sample A and B annealed at 600°C and 650°C for 1 hr. Grain size calculated by Sherrer equation as functions of annealing temperature for A and B.....88

Figure 6. 4 (a) Cross-sectional view of TEM image of as-deposited sample A with the inset showing high resolution. (b) STEM image of same sample in (a) with the scale bar of 20 nm. (c) Plan view and (d) cross-sectional view of TEM image of sample A annealed at 600 °C for 1hr. The inset in (c) shows electron diffraction pattern of the same sample. (e) high resolution TEM (HR-TEM) image from (d) shows fringes.....89

Figure 6. 5 Cross-sectional view of TEM image of sample B (a) as-deposited and (c) annealed at 600°C for 1hr. (b) and (d) shows high resolution TEM image from (a) and (c), respectively.90

Figure 6. 6 In-plane magnetization curves of (a) sample A and (b) sample B annealed at different temperatures for 1 hr, respectively. (c) The dependence of Hc on annealing temperatures for 1 hr is shown.....91

Figure 6. 7 In-plane M-H loops of (a) sample C vs. annealing time at 550°C; (b) sample C annealed at various temperatures; (c) sample D annealed at 550°C for various times and (d) sample D

annealed at various temperatures for 1hr; (e) and (f) are coercivities extracted from (a)-(d) and combined with Figure 6.2 (c) and Figure 6.6 (c) as functions of annealing time and annealing temperature, respectively.	93
Figure 6. 8 (a) In-plane M-H loop and (b) XRD pattern of sample with stack of FeB 9/Pt 10/[FeB0.9/Pt1.0] ₁₅ /Ta5 nm annealed at 600 °C for 1hr.	94
Figure 6. 9 In-plane M-H loops of sample E with FeB additions (a) before annealing and (b) annealed at 400°C for 30minutes; (c) coercivity as a function of FeB layer thickness.	95
Figure 6. 10 (a) In-plane and (b) out-of-plane M-H loops of sample F with stack of [Fe0.47/Pt0.4] ₁₂ lamp annealed at 550°C for 20s~12 min; (c) coercivities vs. annealing time.	96
Figure 6. 11 (a) In-plane and (b) out-of-plane M-H loops of sample G with stack of [Fe0.043/Pt0.036] _{11x12} , lamp annealed at 550°C for 20s-12 min ; (c) dependence of coercivities on annealing time.....	97
Figure 6. 12 (a) In-plane and (b) out-of-plane M-H loops of sample series H with a stack of Fe3/Pt3/ [Fe0.47/Pt0.4] ₁₂ , lamp annealed at 550°C for 20s~12 min by RTA; (c) dependence of coercivities on annealing time.	97
Figure 6. 13 M-H loops of samples with the same thickness but different configurations annealed at 550°C for 5 min by RTA. (a) sample I: [Fe0.5/Pt0.5] ₁₂ ; (b) sample J: [Fe1/Pt1] ₆ , and (c) sample K : Fe3/Pt3/[Fe0.5/Pt0.5] ₆ . (d) The plot compares the H _c and S* of samples I, J and K.	98
Figure 7. 1 Tilted view SEM (at about 45°) of (a) PFS nanospheres and (b) FeBPt nanopillars after ion milling at 55° for 5min.	103
Figure 7. 2 M-H loops of FeBPt ion milled at 55°, 65°, 75° and 85° for (a) 2 min, (b) 3min, (c) 4min, and (d) 5min. The coercivity, H _c , was plotted as functions of (e) etch time and (f) etch angle.....	104
Figure 7. 3 Contour plot of coercivity of FeBPt as functions of etch time and etch angle	105
Figure 7. 4 SEM image of FeBPt after ion milling at 85° for 5min.	105
Figure 7. 5 M-H loops of FeBPt samples ion-milled for 3min at 55°~85° and annealed 600°C for 1hr.....	106
Figure 7. 6 XRD spectra of continuous film and patterned sample being annealed 600°C1hr...106	
Figure 7. 7. 45° tilted view SEM images of FeBPt ion-milled at 55° for (a) 2 min, (b) 3min, (c) 4min, and (d) 5min.....	107
Figure 7. 8 XRD spectra of FeBPt continuous film and those ion-milled at 55° for 2~5min108	
Figure 7. 9 (a) In-plane and (b) out-of-plane of M-H loops of FeBPt ion-milled at 55° for 2, 3, 4 and 5minutes.....	109

Chapter 1 Introduction

1.1 Magnetic Recording

For the past several decades, hard disk drives (HDD) have been the primary storage devices for computers. The areal density and capacity of HDD have been increasing since the first drive RAMAC350 (Random Access Method of Accounting and Control) was produced by IBM in 1956 [1]. This is attributed to the technology breakthrough in recording media (from a single magnetic layer to antiferromagnetic composite media to exchange coupled composite or graded media), heads (from thin film heads to giant magnetoresistive heads to MgO-based tunneling magnetoresistance heads), servo systems, tribology etc. [2-8]. In particular, the transition from longitudinal magnetic recording (LMR) to perpendicular magnetic recording (PMR) yielded additional increase in the areal density. The areal density of PMR as high as 2Tb/in^2 or beyond is expected soon, as shown in Figure 1 [9].

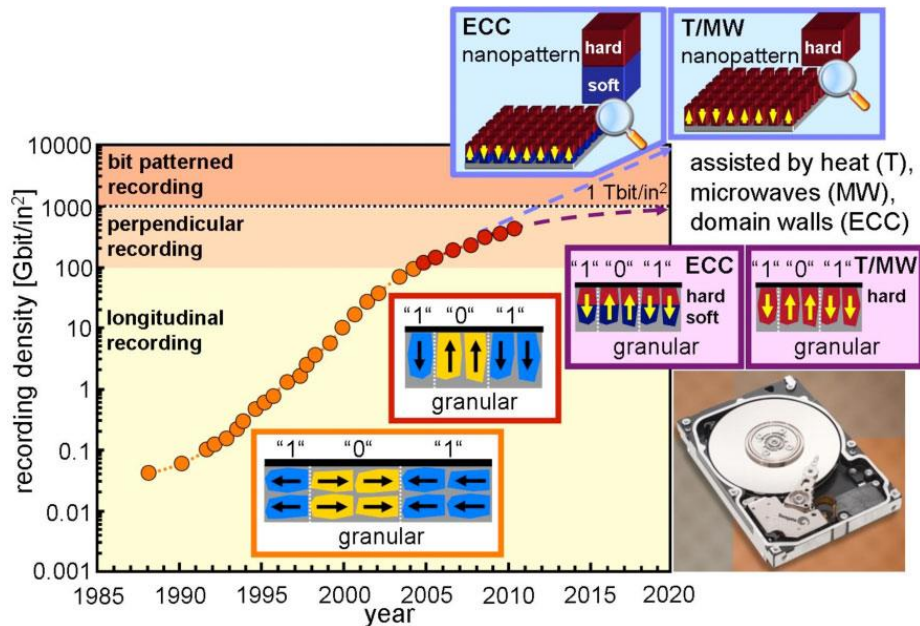


Figure 1. 1 Areal density trends for hard disk drives [Ref.9]

1.1.1 Trilemma of Perpendicular Magnetic Recording

In order to keep increasing the recording density up to 10 Tb/in² by 2018, as targeted by the data storage industry, however, a problem known as the “trilemma of PMR” remains to be solved. [8-10]. This problem refers to the difficulty of satisfying the conflicting requirements of high signal-noise-ratio (SNR), thermal stability and writability in order to achieve the higher areal density for HDDs. As seen in Figure 1.2, each bit is composed of several grains [10]. In order to increase the density, it needs to reduce the grain size or the number of grains N. Reducing N results in decreasing SNR, which is proportional to $\log_{10}N$. Reducing the grain size results in the shrinking of grain volume, hence the thermal stability, $\Delta = K_u V / k_B T$ decreases (K_u is the magnetic anisotropy constant, V is the grain volume, k_B is the Boltzmann constant and T is the temperature), and the system becomes thermally unstable. Meanwhile, the smaller size means a narrower track width, which in turn implies that the magnetic pole which writes should be narrower. As a result, the write field may decrease and thus be unable to write. In order to maintain high thermal stability, it is preferable to choose high anisotropy materials with high K_u , such as L1₀ structured FePt and CoPt. However, the problem with these materials is that the high anisotropy field requires a high write field, which is not achievable by the current write pole. Thus the writability remains an issue. In order to solve this problem, current industry employs shingled-mode write recording [11]; however, this technique can sustain increasing the PMR areal density only for a few more years, as seen in Figure 1. Technical breakthroughs need to be made soon to continue the dominance of PMR. New types of recording, for instance, graded media or exchange coupled composites, or heat assisted magnetic recording (HAMR) will be the next generation of recording media [13]. Bit patterned media (BPM) will be the generation after next, which may push the areal density of HDD as high as 10 Tb/in². [14]

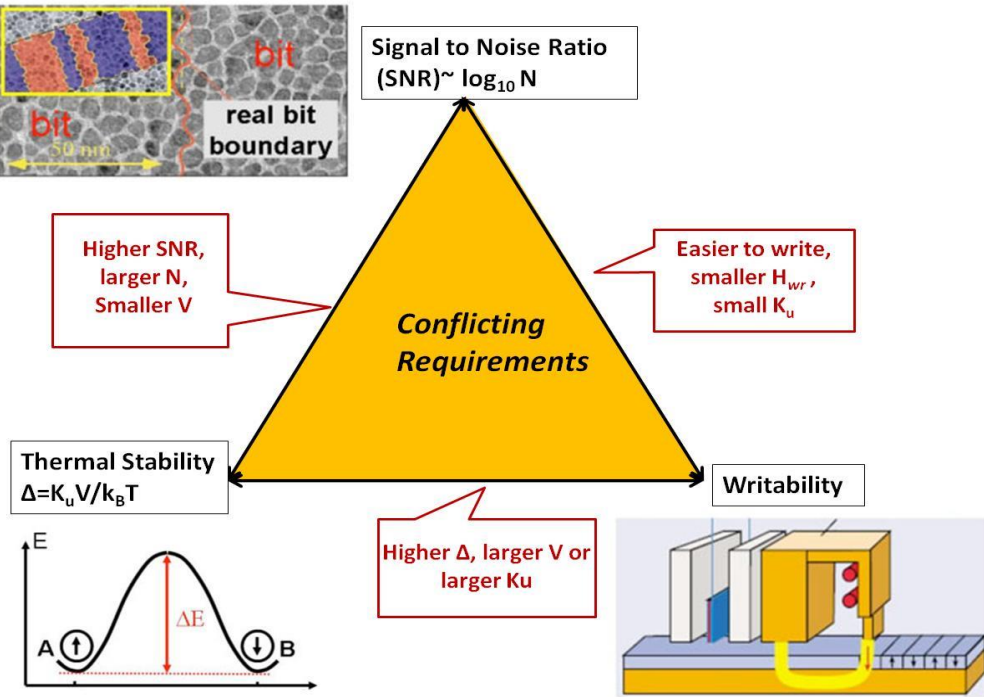


Figure 1.2 Trilemma of Perpendicular Magnetic Recording [Ref. 9]

1.1.2 Heat Assisted Magnetic Recording (HAMR)

Granular L₁₀ FePt is a leading candidate for next generation magnetic recording, in particular, heat assisted magnetic recording (HAMR). This is primarily because of its extremely high magnetocrystalline energy constant ($\sim 7.0 \times 10^7$ erg/cc), which can maintain thermal stability even with a grain size reduced to 3nm, and its corrosion resistance resulting from high Pt content. [13, 15, 16]. During the past decade, much progress has been made. However, significant challenges still exist in the deposition of L₁₀ FePt media, including reducing the ordering temperature, controlling the c-axis orientation and creating small, magnetically decoupled grains with narrow size distribution [16].

In order to transform the A1 disordered FePt (fcc) to the L₁₀ ordered structure (fct) at lower temperature, elements such as Ag, Au, B, Cu, and Ta have been used as dopants to promote ordering. [17-26]. Takahashi et al. [17] reported that the ordering temperature of an FePtCu film was reduced to 400 °C. It was found that the coercivity of this film was 8 kOe and the order

parameter was close to 1, while the undoped FePt remained soft when annealed at the same temperature. The authors suggested that the decrease of the annealing temperature for ordering was because the level of ordering was enhanced due to the higher diffusivity of Fe and Pt atoms in the lower melting point FePtCu alloy. Li reported that the L₁₀ phase can be obtained at 350 °C only for films with the ratio of FeCu to Pt being in the range of 1.1~1.2. A first-principles theoretical study by Chepulkii et al. [29] showed that Cu segregated to Fe sites at surfaces and preferentially substituted for Fe in the bulk. Gilbert et al. [27] reported that, as the Cu content was increased, the tetragonal distortion of the L₁₀ phase was also increased, and this significant change in microstructure resulted in the decrease of the saturation magnetization, M_s, and perpendicular magnetic anisotropy, K_u.

Other elements added to lower the ordering temperature include Ag and Au. Platt et al. [18] reported that FePt films with Ag or Au showed 1-2 kOe higher coercivity values compared to a pure FePt film after annealing at 450 °C. Ag and Au tended to diffuse out of the FePt lattice after annealing at high temperature. The study by You et al.[20] showed that additions of Ag and Au to the FePt film changed the microstructure from an interconnected network to a completely isolated island structure, and the coercivity also increased from 5.4 to 20.5 kOe.

Nonmagnetic materials such as oxides and nitrides are usually used to control the microstructure of magnetic thin films. The nonmagnetic matrix plays roles in decoupling the exchange interaction and reducing the grain size. [30]. The Laughlin group [31-33] reported that uniform and well-isolated columnar grains were obtained by co-sputtered FePt and SiO_x. SiO_x worked better than polycrystalline MgO, since the amorphous oxide segregates better. Perumal of the Hono group [34] found that adding a small amount of C (<12%) to a FePt (4nm) film resulted in interconnected FePt particles. A higher percentage of carbon addition led to the formation of

well-isolated L₁₀ FePt grains. When the thickness of the FePt-C film was larger than 6 nm, however, a double layer of FePt was seen [35]. FePt-TiO₂ granular films had columns with very fine particle size and low coercivity [35]. This was believed to be caused by dissolution of Ti into FePt, which suppresses the L₁₀ ordering. In the FePt-SiO₂ granular film, the phase separation tendency was reported by this group to be weak and not form a completely isolated columnar structure. Using FePt-C as a template, FePt-C+Oxide (SiO₂ or TiO₂) granular films were improved [35]. Granz et al.[28] studied FePt:X (x=Ag, C, B, SiO_x, TaO_x). Using a large volume of segregants creates a trade-off between the formation of small grain size and well-isolated columns and loss of ordering and perpendicular coercivity of the films. Introducing segregants into the FePt reduces ordering and grain size of the films. Ag was found to offset the reduction of ordering in the FePt:X films. TaO_x was found to produce the best exchange decoupling, thermal durability, and grain isolation. It also prevented grain coalescence better than B, C, or SiO_x.

The epitaxial growth of FePt (001) textured films requires a substrate or underlayers with similar lattice parameters to that of L₁₀ FePt. Single crystal MgO (100) is usually used to grow FePt films. However, single crystal MgO substrates are not viable for industry due to their high cost. Therefore, non-epitaxial growth of FePt on low cost substrates (glass or thermally oxidized Si) is required. A layer of MgO with thickness of 2-15 nm is typically sputtered as the seed layer to grow L₁₀ FePt by co-sputtering FePt alloy targets or Fe and Pt targets with segregants [28, 31-36]. In addition, a great deal of work has been done on the Fe/Pt multilayers (MLs) to promote the transformation of FePt from A₁ to L₁₀ structure [37-41]. Yan et al [37] obtained L₁₀ structured FePt by deposition of Fe/Pt multilayers (with thicknesses of 0.47nm/0.4nm) on glass followed by rapid thermal annealing (RTA) at 400 °C for 5s. Wu et al [38] reported that L₁₀ granular FePt-SiO₂ thin films with (001) orientation and well-separated grains, 5.14 nm in size, were obtained

by depositing atomic-scale Fe/Pt/SiO₂ MLs on glass and rapid thermal annealing (RTA) at 350 °C. It was believed that the interdiffusion distance was decreased due to the atomic scale deposition. The difference in the surface energies of FePt and SiO₂ drove the SiO₂ to diffuse to the grain boundaries to reduce the interfacial energy. This may have significantly accelerated the diffusion of Fe and Pt atoms. Gilbert et al [27] reported tuning the magnetic anisotropy in (001) oriented L1₀ FePtCu films by atomic-scale ML sputtering and RTA.

1.1.3 Bit Patterned Media (BPM) by Conventional Method

An alternative method for increasing areal density is bit patterned media (BPM), which stores a bit of information on a single domain island [14]. Generally speaking, BPM can be produced by two methods, additive and subtractive, as shown in Figure 1.3 [42]. In the additive method, magnetic materials are deposited on the substrate with patterns which have been predefined by lithographic methods, as shown in Figure 1.3 (a) and (b). In the subtractive process, the pre-deposited magnetic film is patterned and etched or milled to remove the unwanted parts and obtain separate bits. However, for any of these methods, patterning is the critical process. Typically, the following methods are utilized to pattern thin films: nanosphere lithography (NSL), electronbeam lithography (EBL), nanoimprinting, and block co-polymer (BCP) templating. [43-48]. Nanosphere lithography employs nanospheres such as polystyrene or silica as an etch mask to transfer patterns to magnetic films. It is a simple and economical process, which involves formation of a monolayer, size-tuning by plasma ashing and pattern transferring by ion-milling or sputter etch [43,44]. Li et al patterned a CoPt film into ~40 nm arrays [43] ; however, it is hard to get a uniform and sub-20 nm sized patterns over a large area. Electronbeam lithography is a direct writing process to define regular and uniform patterns with very small size distribution, one dot at a time. [46]. However, it is impossible to apply this technique directly to pattern films on a large

scale, since it is high cost and time consuming. [46]. Nanoimprinting takes similar concepts to those of reproducing CD-ROMs, which use expensive fabrication of a master and inexpensive replication [42]. A master mold is produced by EBL and replicated into many daughter molds, which imprint patterns [47]. This method has potential for scale-up of nanopatterning for industry as the cost is acceptable. Another choice is block copolymer (BCP) templating, which employs the phase separation of a di-block copolymer to form patterned arrays by selectively removing one phase and transferring patterns by etching.[48,49]. It is considered to be one of the most promising nanopatterning methods for industry, as it is an inexpensive process and capable of producing uniform patterns of sub-10 nanometer size over a large area. Cheng et al. reported that arrays of organometallic polyferrocenyldimethylsilane (PFS) spheres with diameter of 25 nm and periodicity of 50 nm were formed after O₂ plasma removed the exposed PS matrix. [48, 49]. Hellwig et al. reported BPM by depositing Co/Pd multilayers onto pre-patterned silicon substrates using PMMA-PS self-assembly [50] and patterning the Co/Pd multilayers on the silicon substrate with the same methods [51]. In both cases, the patterned Co/Pd multilayers showed well-defined size and spacing and narrow switching field distribution (SFD).

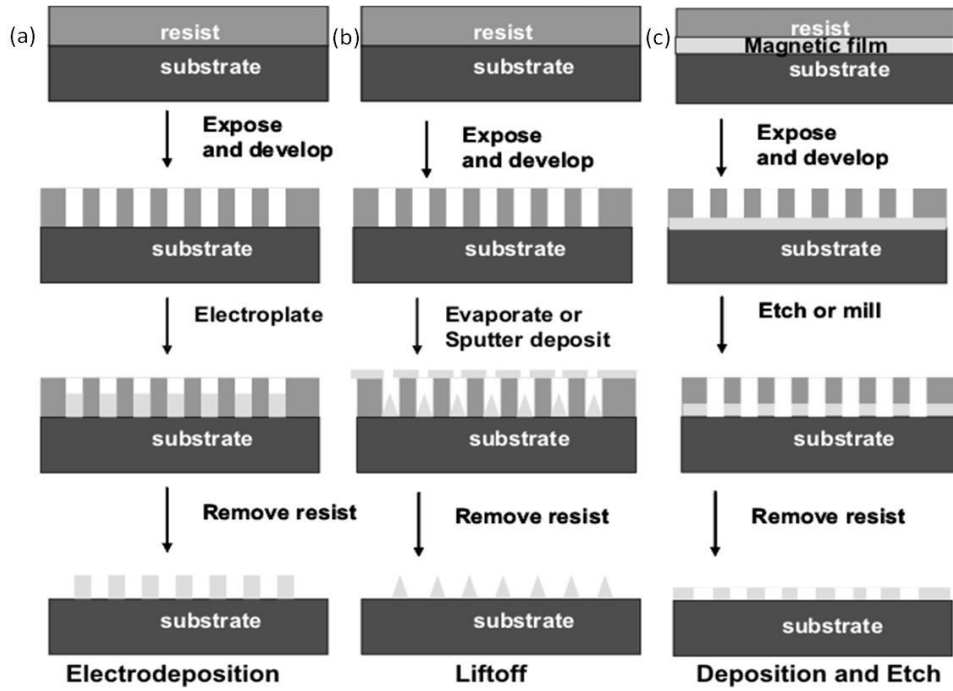


Figure 1.3 Schematic of additive (prepattern and deposition) and subtractive (deposition and etching) patterning [Ref. 42]

1.1.4 Bit Patterned Media (BPM) by Glancing Angle Deposition (GLAD)

Glancing angle deposition (GLAD) is a physical vapor deposition method in which the incoming flux from the source impinges on the substrate at oblique angles, causing increased shadowing compared to normal incidence [52,53]. By rotating the substrate at certain speeds, it can produce various nanostructures including nanopillars, zigzags Y-shape, helices, as shown Figure 3.[53-59] However, most of these studies have focused on nonmagnetic materials with the potential application for photonic crystals [60,61], sensors [62] and optical nanoemitters [63]. Few magnetic materials have been studied for the purpose of information storage [64-66]. It will be of great importance to magnetic nanopillars for the purpose of high density information storage as the formation of nanopillars is a single- step sputtering process.

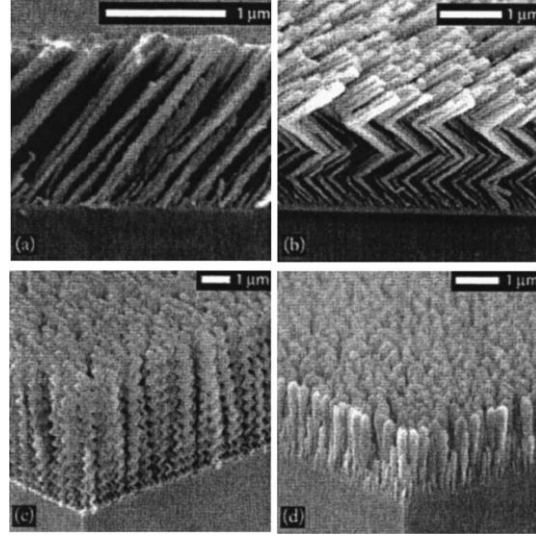


Figure 1.4 Archetypal GLAD fabricated microstructures, (a) tilted columns, (b) zig-zag columns, (c) helical columns, and (d) vertical columns. [Ref.52]

1.1.5 Thin film Nucleation and Growth

Thin film deposition involves nucleation and growth. Nucleation means a phase transition from vapor in the chamber to solid on the substrate.[67] After the initial stage of nucleation, thin film formation falls into following three modes: (1) Fran-van der Merwe (layer) Mode,(2) Volmer-Weber (island) and (3) Stranski-Krastanov (mix) Mode, which are illustrated in Figure 1.5. In Frank-van der Merwe mode, the atoms condensed or adatoms are bound to the substrate surface, rather than to each other. The adatoms fill up the terrace edges and form monolayer and continue to grow layer by layer. In Volmer-Weber mode, adatoms are more prone to bind to each other and form clusters and islands. Stranski-Krastanov mode combines characteristics from both other growth modes. In the beginning, one or more layers form. However, continuing layer growth cannot sustain and islands form.

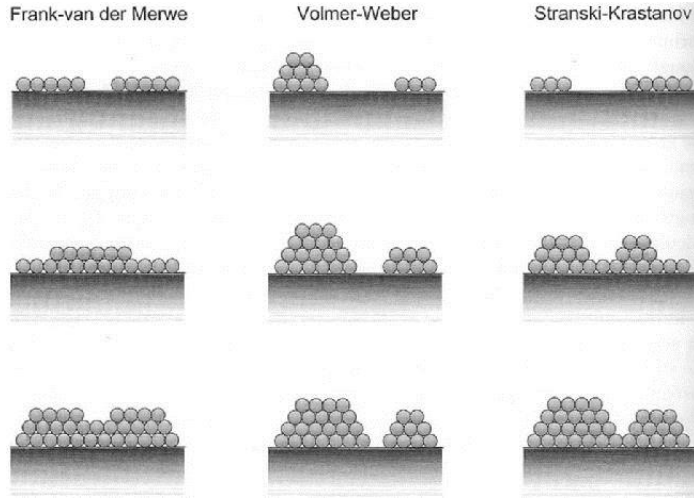


Figure 1.5 Basic modes of thin-film growth [Ref. 67, 68]

Movchan and Demchishin proposed a three region structure zone model (SZM) as shown in Figure 1.6 to predict microstructure on substrate temperature, which affects the surface diffusion of adatoms. In Zone I, T_s/T_m is below 0.3 (T_s is the substrate temperature and T_m the melting point of the materials), the temperature is too low for adatoms to diffuse in large scales. The film is mainly composed of tapered columns with voids. In Zone II, $0.3 < T_s/T_m < 0.5$, the film is denser and composed of columnar structure because of increased temperature increasing surface diffusion. In Zone III, $T_s/T_m > 0.5$, as the temperature is high enough for strong surface and bulk diffusion to occur, the films consist of equiaxed grains. Thornton proposed a revised SZM to discuss the effect of gas pressure. In addition to what described in above SZM, high gas pressure leads to large size columns with voids and lower gas pressure leads to small columnar structure. [70].

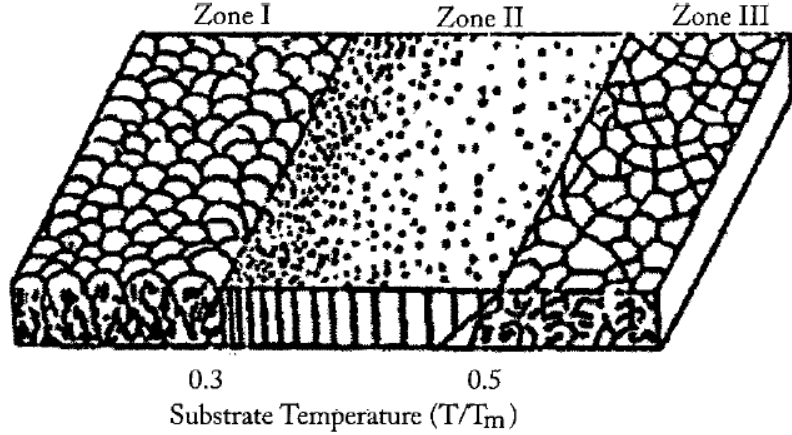


Figure 1.6 Structure zone model by Movchan and Demchishin. [Ref. 69]

For glancing angle deposition (GLAD), film growth mostly occurs in Zone I in the SZM, since the low temperature limits the surface diffusion and exemplifies the growth of columnar grains [53]. In addition, the shadowing effect is critical for the formation of the columnar structure. The incoming flux from the source impinges on the substrate at oblique angles; any non-planar surface will cause a ballistic shadowing effect. Even with a flat surface, shadowing effects can occur. It is because the nucleation roughens the surface and the nucleus captures more atoms than the shadowing area around it, as shown in Figure 1.7. With increasing deposition time, this effect is additive, and nanorods or columnar structures form.

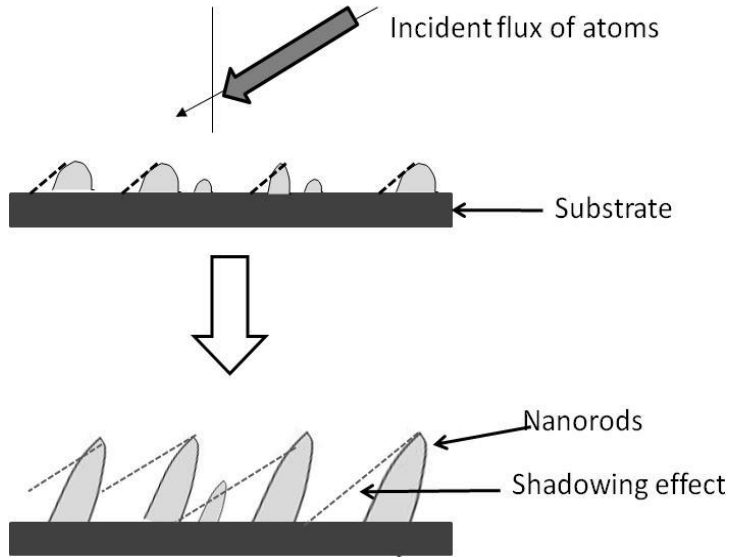


Figure 1. 7 Schematic of nanorods growth by glancing angle deposition

1.2 Proposed Research Objectives

The main objectives of this dissertation are to explore the different approaches to fabricate magnetic materials for advanced media. We have aimed our research towards the following areas of interest in this dissertation:

- (1) Study Co/Pd multilayered continuous films and understand the effects of individual thicknesses of Co and Pd, Co/Pd thickness ratio, number of bilayers, and type of underlayers on the magnetic properties.
- (2) Optimize Co/Pd multilayered nanopillars patterned by nanosphere lithography and block copolymer templating.
- (3) Investigate and optimize fabrication of nanopatterned media by a one-step process: glancing angle deposition
- (4) Study magnetic properties and microstructure of Fe(B)/Pt multilayered thin films by different sputtering approaches and pattern them by BCP templating.

1.3 Dissertation Outline

The current chapter briefly introduced the background of hard disk drives, the trilemma issues that PMR is facing, the study for heat assisted magnetic recording (HAMR) and bit patterned media (BPM). The novel glancing angle deposition (GLAD) method was also introduced for the fabrication of BPM. Chapter 2 introduces the basic principles and equipment of experiments. Chapter 3 details a systematic study on Co/Pd multilayered continuous films. Chapter 4 discusses the nanopatterning processes by nanosphere lithography and block copolymer templating. Statistical approaches of patterning by BCP will be addressed. Chapter 5 details the fabrication of nanorods by the GLAD one step-process. Chapter 6 explores the microstructural evolution and magnetic properties of Fe(B)/Pt multilayered films and Fe(B)Pt composite films. Chapter 7 discusses the B-doped FePt patterned by block copolymer templating. Finally, Chapter 8 concludes all the studies and provides a direction for future work.

Chapter 2 Experimental Techniques

2.1. Introduction

The main purpose of this research was to explore perpendicular magnetic anisotropy (PMA) material systems for application to advanced media. All the thin film multilayers were deposited in the UA Micro-Fabrication Facility (MFF) using a SFI Shamrock 7-gun planetary sputtering system. Characterization of the crystal structure and morphology of the thin film multilayers was carried out using X-ray diffraction (XRD) on a Philips X'pert X-ray diffractometer, transmission electron microscopy (TEM) on a TECNAI 20 FEG-TEM, scanning electron microscopy (SEM) using a JEOL 7000F FEG-SEM all located in the Central Analytical Facility (CAF) and the Center for Materials for Information Technology (MINT). Additionally, atomic force microscopy (AFM) was carried out on Dr. Jinhui Song's Park XE-70 instrument. Magnetic characterization was carried out using a Princeton Scientific Micromag 2900 alternating gradient magnetometer (AGM) in MINT and on Dr. Arunava Gupta's Quantum Design superconducting quantum interface device (SQUID). Nanopatterned magnetic arrays of dots were fabricated using a deep reactive ion etcher, the STS advanced oxide etcher (STS-AOE) and the Intelvac ion-mill with a Veeco ion source in UA-MFF. Vacuum annealing was carried out using a lamp array in the Shamrock system and also using a custom-built furnace annealer in MINT. In this chapter, all the equipment involved at different stages in growth, fabrication and analysis will be discussed.

2.2 Fabrication Techniques

2.2.1 Sputtering

Magnetron sputtering is a physical vapor deposition (PVD) process in which the ejected atoms of a source material (target) resulting from the bombardment of positive argon ions (plasma) deposit on the substrate [67]. In industry, sputtering is one of the most frequently used methods to deposit thin films for various applications, for instance, semiconductors, computer hard disk drives, wear-resistant coatings, and optical coatings [67]. The MFF is equipped with a Shamrock planetary sputter deposition system, as shown in Figure 2.1(a). All the depositions were carried out on this system. It is a fully automated, load-locked sputter-up system with six 3" diameter S-gun cathodes, and a lamp array used for in-situ heating before, during or after deposition. A batch of 4 substrates up to 6" in diameter can be processed as shown schematically in Figure 2.1 (b). The targets can be conductive, non-conductive, magnetic or nonmagnetic materials, with a choice of using DC, AC or RF modes. The ultimate base pressure of the process chamber can reach 10^{-9} torr. Our typical base pressures were in the range of $2-5 \times 10^{-8}$ torr.

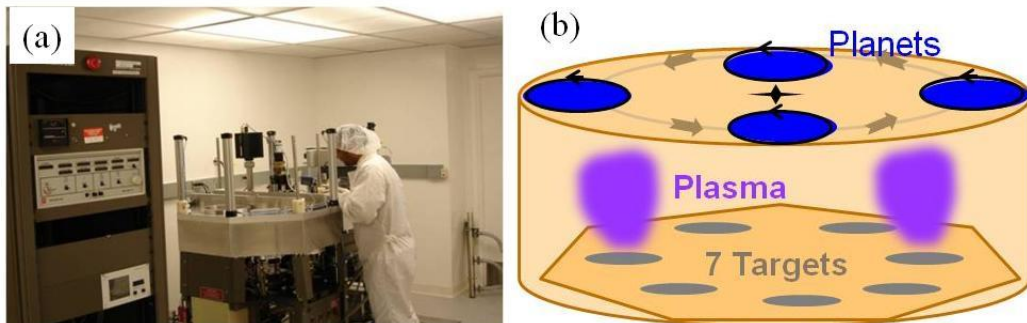


Figure 2. 1 (a) Photo and (b) schematic of SFI Shamrock sputtering system in UA-MFF [Ref. 71]

The S-gun cathode consists of 3 elements of a magnetron, an anode, a cathode and a magnetic field to confine the electrons. An array of permanent magnets are placed around the cathode such that the magnetic flux is parallel to the target surface and intercepts at two corners of the target as shown in the Figure 2.2. The magnetron field serves to confine the ions and electrons

close to the surface of the target, and they move around the area of heaviest target erosion (the erosion groove or “racetrack”) with a drift velocity proportional to the cross-product of the electric and magnetic fields, and perpendicular to both of them. The cathodes are powered by DC, AC or RF supplies. Reactive deposition of oxides and nitrides may be achieved from elemental targets by AC sputtering with a given partial pressure of O₂ or N₂.

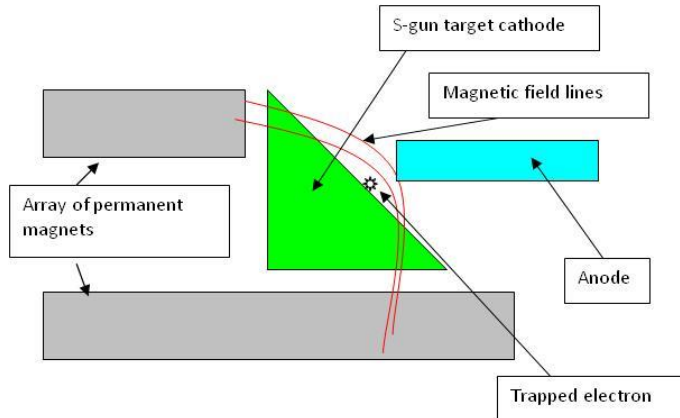


Figure 2. 2 Schematic of S-gun cathode assembly in Shamrock sputtering system. [Ref 72]

The main features of this sputtering tool are as follows:[72]

1. Load-locked, 6 cathodes, planetary deposition for multilayers with high uniformity and repeatability.
2. Radiant heat for rapid thermal annealing (RTA) for *in situ* annealing.
3. Recipe-driven software for complex deposition sequences.
4. Materials systems mentioned below are all developed using this system
 - a. Co/Pd, Fe/Pt, FeB/Pt MLs
 - b. Co/Pd, Fe(B)/Pt, CoPt nanorods
 - c. Co₄Pt, Co₃Pt, FePt, FeB/Pt multilayers and alloys
5. Sequential, simultaneous and glancing angle deposition processes developed

2.2.2 Plasma Treatment

For typical lithographic methods, plasma treatment and ion-milling are always used.

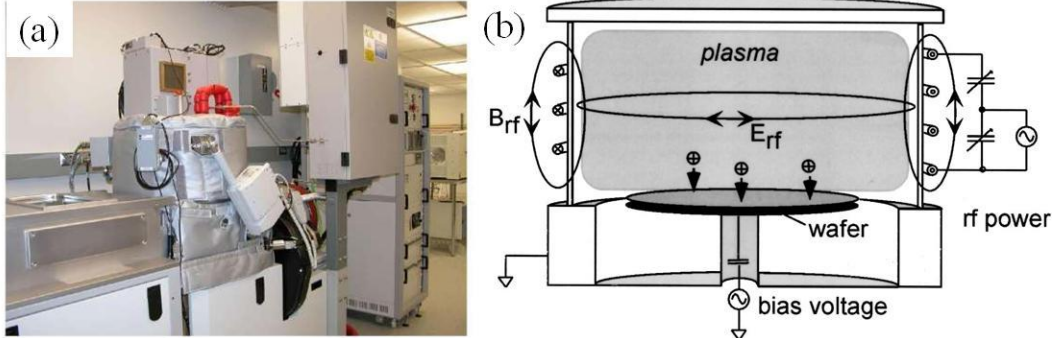


Figure 2.3 Photo of STS-AOE and schematic of ICP etching chamber of STS_AOE [Ref. 73,74]

The STS advanced oxide etcher (STS-AOE) is a loadlocked, high frequency inductively coupled plasma (ICP) etch system [75]. As shown in the schematic, a coil (planar source) that rests in the top of the chamber can produce high density plasmas. The system is configured for dielectric etching and O₂ cleaning. The operating frequency is 13.56 MHz. Independent energy control is achieved by biasing of the electrode (platen) via automatic power control and impedance matching. De-ionized water is used to cool the platen and helium is used to cool the backside of the substrate. Depending on the application, gases including O₂, C₄F₈, CF₄, H₂ (Hydrogen), He and Ar are configured. It can load a maximum of two 4" substrates manually. It can perform an extremely rapid, deep etch on glass, quartz and other oxides as well as polymers. It can also be used to etch metals. The main features are as follows. The load-lock reduces pumping time. The downstream process causes less substrate heating and damage. High density plasma (up to 10¹² ions/cm⁻³) results in high etch rate at low bias; low pressure process leads to good anisotropy and independent ion energy [73, 74]. We have used it to shrink nanospheres and remove polystyrene in the block copolymer (BCP) with an oxygen plasma.

2.2.3. Ion Milling

Ion milling is a plasma based etching process where anisotropic etching of the substrate can be achieved on the patterned wafer without forming any hazardous waste. Ion beam milling

can be viewed as an atomic sand blaster. Instead of actual sand grains, accelerated argon ions with high energy bombard the surface of the substrate inside a vacuum chamber and remove surface materials. The rotation of the stage where the substrate is mounted ensures uniform removal of waste material and results in straight side walls. As the mask is also under bombardment of Ar^+ ions, the key to a successful ion-milling process is that the etch mask can last long enough to protect the target materials. The main advantage of this type of plasma etching is that of high anisotropy compared to wet etching. This is highly directional, anisotropic and hence reduces undercuts. Figure 2.4 shows the Intelvac ion-mill system used in the UA-MFF to pattern Co/Pd multilayers and FeB/Pt composites with a polymer etch mask.

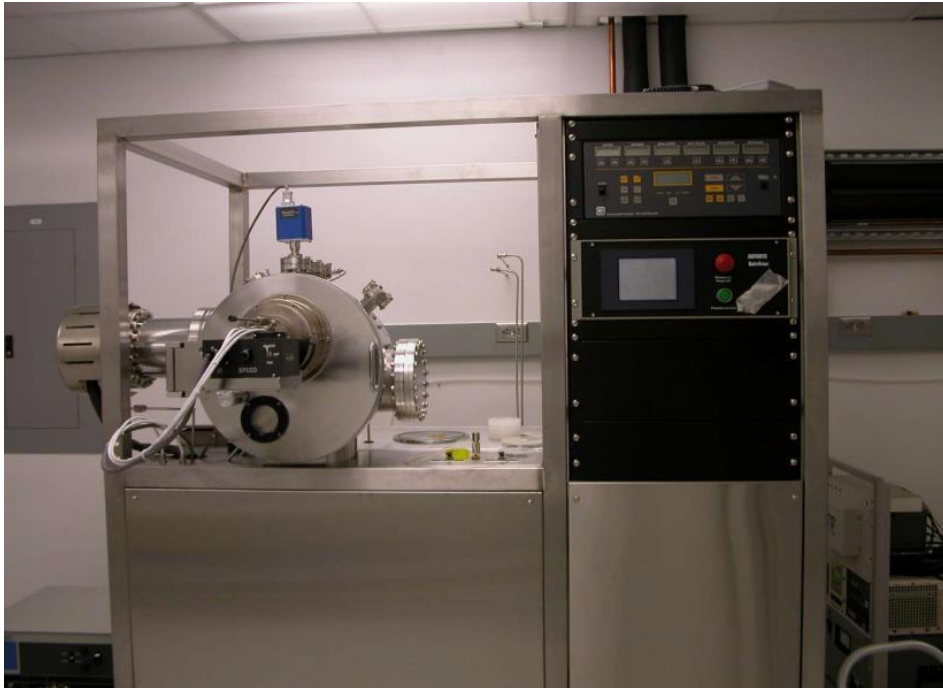


Figure 2. 4 Intelvac ion-mill system in UA-MFF [Ref. 72]

2.3 Morphologies and Structural Characterization

2.3.1 Atomic Force Microscopy (AFM)

Atomic force microscopy (Park System, Inc., model XE-70) was used to analyze film surface topography and roughness of films with the tapping mode. A photo and a schematic of AFM are shown in Figure 2.5. A very fine AFM tip attached to the end of an oscillating cantilever, which is vibrated by a piezo mounted above it, is brought into close proximity to the sample surface. An extremely small force between the probe tip and the surface of the sample bends the cantilever upwards. The amplitude of bending is detected by a laser spot reflected on to a split photo detector and used to calculate the force. The tip lightly “taps” on the stationary sample surface during scanning while the feedback loop maintains constant oscillation amplitude. The vertical movement of the tip follows the surface profile and the deflection of the cantilever is measured. A feedback loop is used to maintain a constant cantilever deflection [71]. These scans at each point are used to form a topographic image of the sample surface. As the films are magnetic, a different tip will be used to eliminate the effect of magnetic force on the topography.

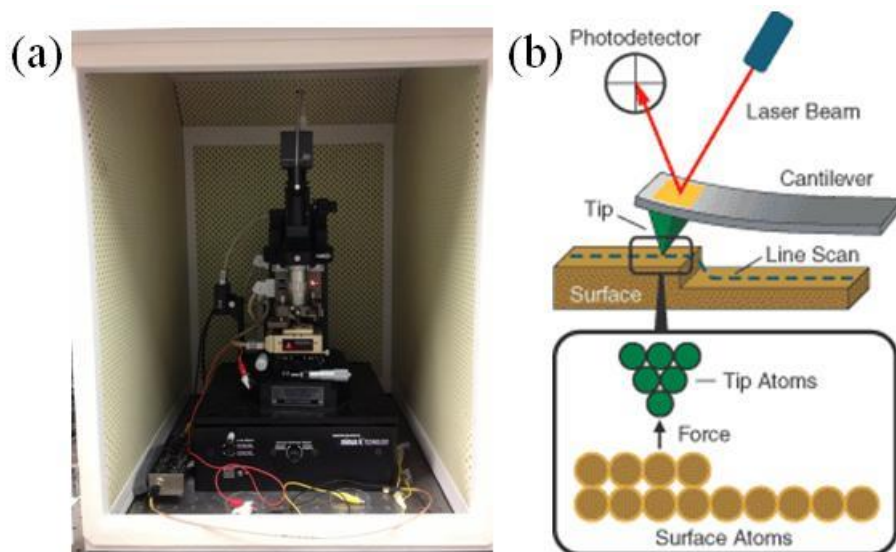


Figure 2. 5 Photo (a) and schematic (b) of AFM [Ref. 76]

2.3.2 Scanning Electron Microscopy (SEM)

A field emission gun scanning electron microscope (FEG-SEM) was used to image the films and nanostructured samples. The magnification is up to 300,000X and the resolution is as high as a few nm. It is also equipped with an Oxford detector for energy dispersive X-rays (EDX) analysis.

As can be seen in the schematic in Figure 2.6, there are a set of lenses along the path of electrons. These lens and coils control magnetic field to adjust the movement of electrons. The detector collects the secondary electrons or x-rays which are generated by the interaction of source electrons with the sample surface. It should be noted that the SEM is effective for observing the morphology, but not capable of detecting the microstructure of the samples.

The sample preparation was very easy for our samples since they were conductive. In most cases, the samples were imaged as “as-is” without special treatment.

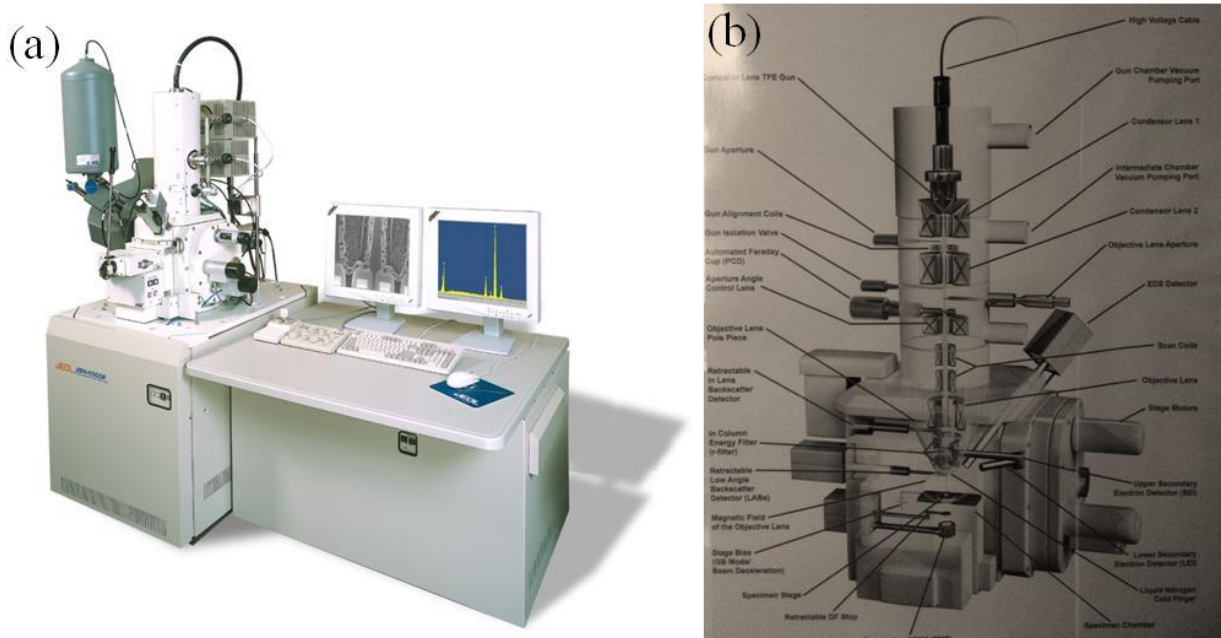


Figure 2.6 (a) Photo of JEOL 7000F SEM and (b) schematic of its components [Ref. 71]

2.3.4 X-ray Diffraction/Reflectivity (XRD/XRR):

X-ray diffraction is a non-destructive test technique which utilizes Bragg's law to get crystalline information of samples: [77]

$$2d\sin\theta = n\lambda$$

where n is the order of diffraction, an integer (1, 2, ..., n), λ is the X-ray wavelength, d is the interplanar spacing, and θ is the Bragg angle, the angle of incidence of the x-ray beam striking the sample surface. Cu-K α 1 radiation ($\lambda = 0.15406\text{nm}$) was used in characterizing the samples. Figure 2.7 shows a photo and schematic of the Philips X-Ray diffractometer. Basically, it contains three components, X-ray source, sample stage and X-ray detector. For our multilayers and alloys, this technique was used to characterize the crystal structure, while X-ray reflectivity (XRR) measurements were done to characterize the roughness and measure the thickness of the deposited films. The relative grain orientation or texture of the polycrystalline film can be detected by rocking curves. The grain size can be determined by Sherrer's equation $D = \frac{B\lambda}{\beta \cos\theta}$, where B is a constant, 0.89, λ is wavelength of the X-ray, β is the full width at half maximum (FWHM) measured from the XRD peaks, θ is the incident angle of X-ray. [78]. The thickness of the films was determined by XRR. The deposition rates were calculated by dividing the thickness by the deposition time.

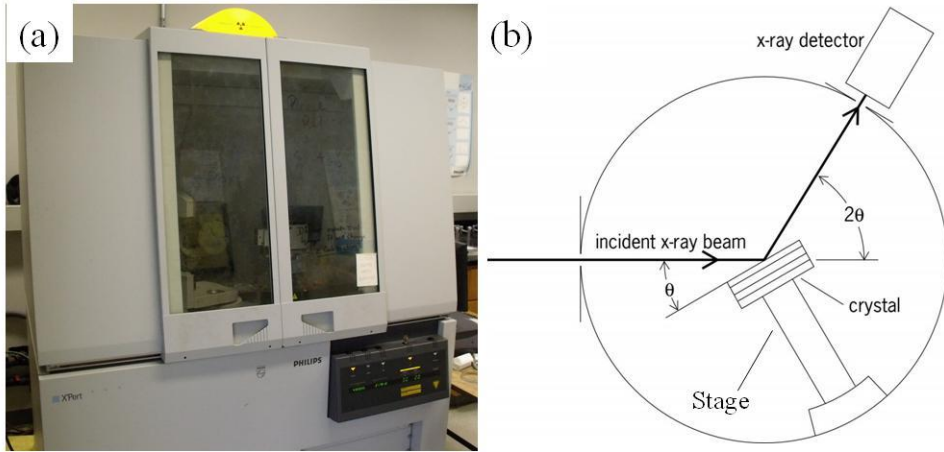


Figure 2.7 (a) Philips X-ray diffractometer [Ref.79] and (b) its schematic [Ref. 80]

2.3.5 Transmission Electron Microscopy

Transmission electron microscope (TEM) is the most important tool in the field of materials research. We can obtain microstructure, crystallographic information, and compositional information, as well as strain if equipped with other detectors [81]. The basic idea is that it shines a beam of electrons, which interacts with the ultrathin specimen and forms images or patterns, depending on the type of electrons the detector collects. Figure 2.8 shows a schematic of a TEM with two basic operation modes (a) diffraction, projecting the diffraction pattern onto the viewing screen and (b) image, projecting the image onto the screen. As seen in Figure 2.8 (a), an aperture is put in the path of the diffracted electron beam so that only the area of interest will be observed. The diffraction pattern can give in-plane crystallographic information, which is different from XRD. With this aperture in position, a dark field image can be produced. If the SAD aperture is removed as shown in Figure 2.8 (b), the direct beam and inelastic scattered beam can form bright field (BF) images, which give the information of phase and microstructure and grain orientation. In BF images, elements with larger atomic number are observed as dark areas if the thickness is the same. The resolution can go down to sub-nanometers. It should be noted that the imaging

systems shown here are highly simplified. Modern TEMs have more lenses which provide higher magnification and larger focusing range for both images and diffraction patterns. STEM was also performed to obtain the morphology of the samples.

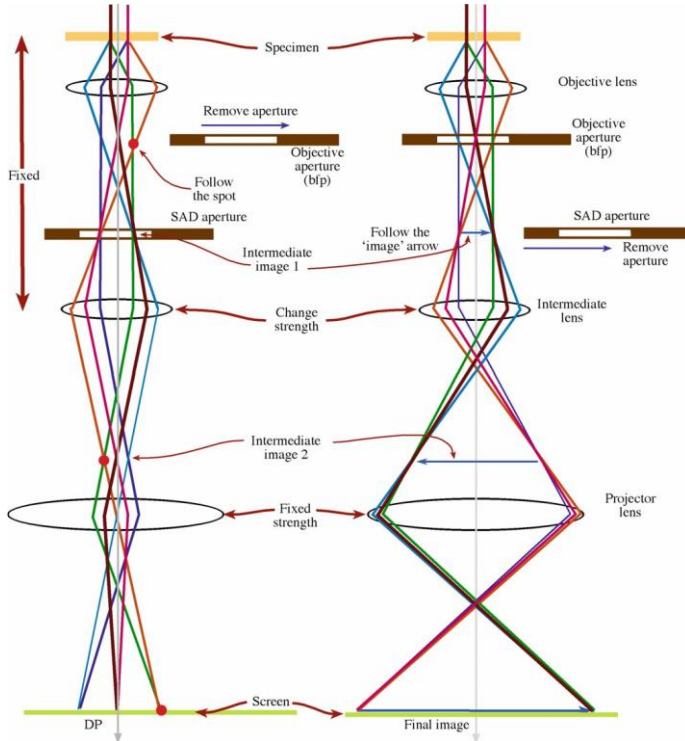


Figure 2.8 Schematic of TEM show two basic operations of the TEM imaging system (a) diffraction mode and (b) image mode. [Ref. 81]

To obtain good TEM images or patterns, extreme caution should be taken during the preparation as the thickness of the sample is less than 100 nm. For plan view and diffraction patterns, the samples were prepared by conventional methods, including grinding, polishing, dimpling and ion-milling. For the cross-sectional samples, they were produced by focus ion beam (FIB). Figure 2.9 shows the FIB in the CAF and a typical process of TEM sample preparation. It uses Ga as the ion source. A typical process is as follows: depositing Pt bar to protect the sample, cutting all sides of the bar by Ga ions and welding it to the probe tip by depositing some Pt at the

contact area, cutting the remaining part and welding it to the TEM grids, then thinning the sample to a few tens of nm by Ga ions.

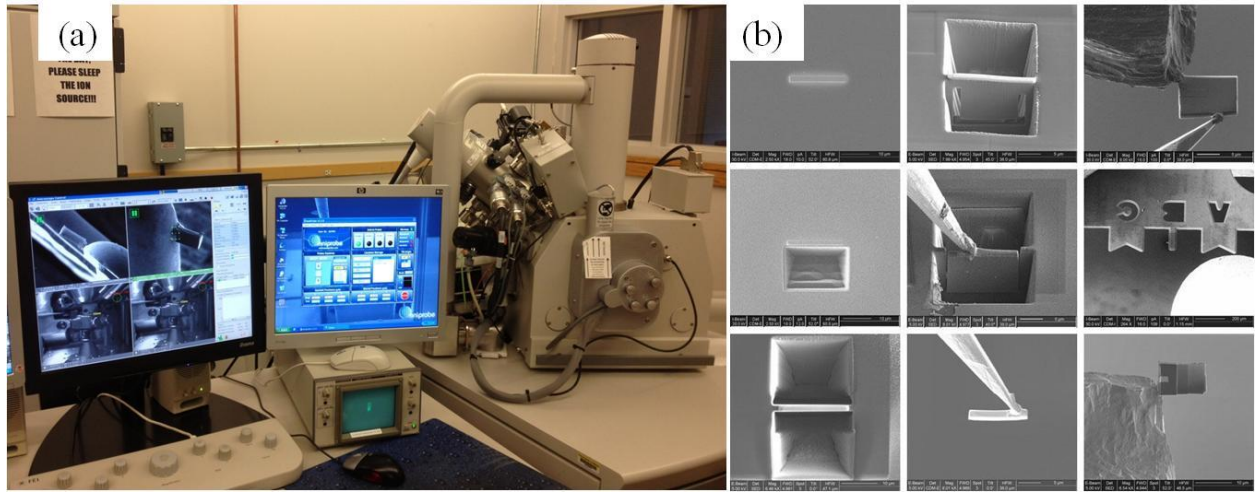


Figure 2.9 (a) FIB (FEI Quanta 3D Dual Beam) in CAF and (b) demo procedure of TEM sample prepared by FIB [Ref. 82].

2.4 Magnetic Characterization

2.4.1. Alternating Gradient Magnetometer (AGM)

An alternating gradient magnetometer (AGM) as shown in Figure 2.10 is used to measure the M-H loops of the magnetic thin film samples, from which the magnetization, coercivity and magnetic anisotropy can be determined. This method of measurement is fast and sensitive as it usually has a low noise level. In the measurement, the sample with a size of 5 mm x 5 mm or smaller is mounted on the tip of a vertical extension rod which is attached to a piezoelectric transducer at the top, as shown in Figure 2.10. The electromagnet produces a strong magnetic field up to 1.8 Tesla (18 kOe) to magnetize the sample. The gradient coils apply an AC gradient field which exerts an oscillatory force on the magnetized sample. This causes the bending of the transducer and produces a voltage proportional to the amplitude of the oscillation, which is proportional to the magnetic moment of the sample. The signal is optimized when the vibrating frequency of the sample reaches the resonance frequency of the cantilever system. The system

needs to be calibrated before each measurement with a standard magnet with known magnetic moment for accurate measurements. We used a standard yttrium iron garnet sample from NIST with a magnetic moment of 78.33 memu/cm³ for the calibration.

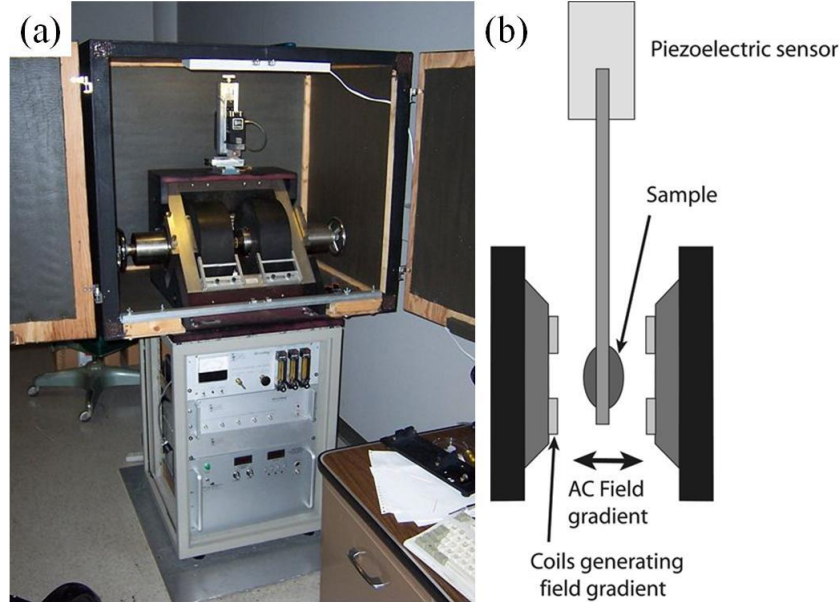


Figure 2. 10 (a) Princeton alternating gradient magnetometer [79] and (b) its schematic [83]

2.4.2 Superconducting Quantum Interference Device (SQUID) Magnetometer

A superconducting quantum interference device (SQUID) magnetometer with a maximum field of 5 Tesla as shown in Figure 2.11 was used to measure M-H loops for those samples which could not be saturated with a magnetic field of 1.8 Tesla (the maximum field of the AGM). The magnetic measurement can be done at temperatures ranging from 4.2K to 350K. The SQUID is thus ideally suitable for operation in a very high field at low temperature environment. As shown in Figure 2.11, the key part of the SQUID magnetometer consists of superconducting coils which are separated by thin insulating layers to form two parallel Josephson junctions. When a sample passed between the pick-up coils, the flux change caused by the magnetic sample, can be detected

and translated into hysteresis loops.[15] It is worth noting that the temperature is required to be highly stabilized during the measurement to avoid background effects.

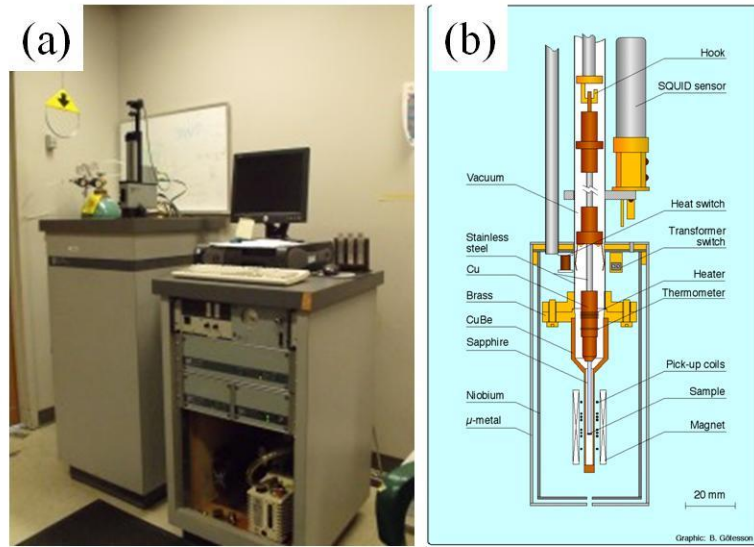


Figure 2. 11 (a) Quantum design -magnetic properties measurement system [Ref. 79] and (b) its schematic illustration [Ref. 84]

Chapter 3 Co/Pd Multilayered Continuous Film

3.1 Introduction

Multilayered materials, such as Co/Pd and Co/Pt, have been an attractive area of research because of their applications in the field of magnetic recording and spintronics. These multilayers have shown high perpendicular magnetic anisotropy (PMA) and high squareness which a single layer cannot have [85~87]. One of the most attractive properties of these multilayers is that the anisotropy and coercivity can be easily tuned by changing the thickness ratio of Co to Pd or Pt, or by changing the number of Co/Pd (Pt) bilayers [88].

In this chapter, the effects of changing various parameters, such as Co thickness, Pd thickness, the ratio of the thicknesses, number of bilayers, and types of seed layers, on the magnetic properties were systematically studied. The magnetic properties characterized were coercivity (H_c), squareness (S^*), perpendicular anisotropy (K_u) and switching field distribution (SFD).

3.2 Experiments

Based on a previous study by our group, [89,90] a series of Co/Pd multilayers (MLs) with the following stack: seed layers /[Co t_{Co} /Pd t_{Pd}] $_N$ /Ta5 nm were deposited onto (001) silicon substrates using the SFI Shamrock planetary magnetron sputtering system in the UA Micro-Fabrication Facility. The seed layers, t_{Co} , t_{Pd} and N were varied and will be detailed in each section. The base pressure prior to deposition was 5×10^{-8} Torr and the deposition pressure of Ar was maintained at 2 mTorr. The sputtering power ranged from 67 W to 279 W, which corresponded to deposition rates from 0.013 to 0.083 nm/s. The thickness of the metallic layer was determined by X-ray reflectivity (XRR). The deposition rate was thus accurately determined, and the desired thickness of material was deposited by varying the deposition time.

The morphologies of the samples were characterized by atomic force microscopy (AFM) and field-emission scanning electron microscopy (FE-SEM). The structures were characterized by X-ray diffraction (XRD) and roughness by X-ray reflectivity (XRR). The magnetic properties were studied by alternating gradient magnetometry (AGM) and a superconducting quantum interference device (SQUID).

3.3 Results and Discussion

3.3.1 Magnetic Property Dependence on Co and Pd Thickness

3.3.1.1 Co thickness fixed, Pd thickness varied

A series of Co/Pd MLs with a stack of Ta 5/Pd 5/[Co t_{Co} /Pd t_{Pd}]₉/Ta 5nm were deposited, where $t_{Co}=0.2, 0.25, 0.3, 0.35, 0.45$ nm and $t_{Pd}=0.4, 0.6, 0.7, 0.8, 0.9, 1.0, 1.2$ nm respectively. First, we fixed the thickness of Co, $t_{Co}=0.2, 0.25, 0.3, 0.35, 0.45$ nm, and then changed t_{Pd} for each thickness of Co. Typical hysteresis loops are shown in Figure 3.1, and corresponding H_c and S^* dependence on thickness of Pd are shown in Figure 3.2. The squareness S^* is defined as the ratio of remanent magnetization over saturation magnetization, that is, $S^*=M_r/M_s$ or $S^*=M_r t/M_s t$. As seen in Figure 3.1, out-of-plane M-H loops were very square. S^* for all the samples plotted in Figure 3.2 were larger than 0.9, close to unity, indicating strong perpendicular magnetic anisotropy (PMA) energy. [89~91]. We found that for the $t_{Co}=0.2$ nm and 0.45 nm, H_c began to decrease when t_{Pd} increased to 1.0 while for $t_{Co}=0.25, 0.3$ and 0.35 nm, H_c continued increasing in the whole range of Pd thicknesses from 0.4 to 1.2 nm.

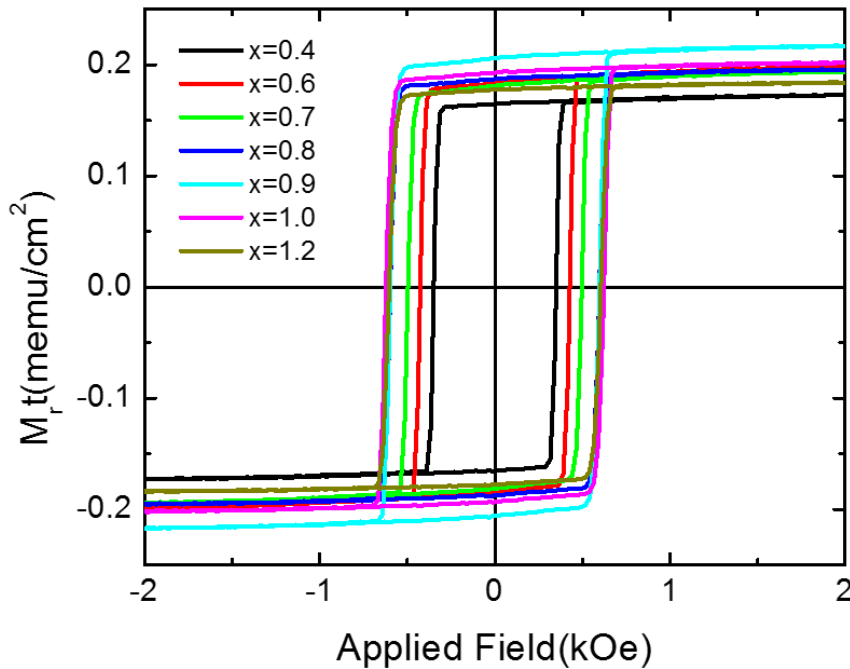


Figure 3. 1 1 Out-of-plane M-H loops of Co/Pd MLs with stacks of Ta5 /Pd5 /[Co0.2/Pd t_{Pd}]9/Ta5 , where t_{Pd} varied from 0.4 to 1.2 nm .

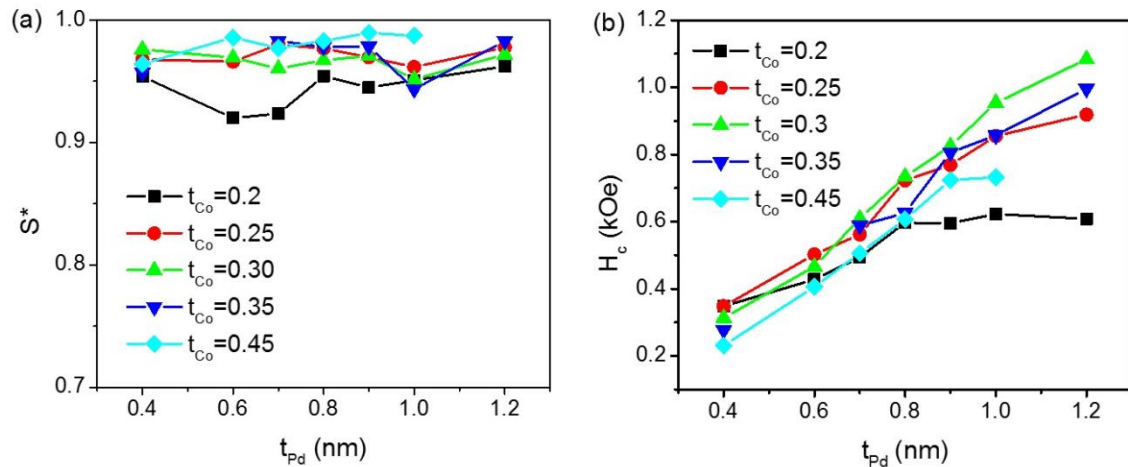


Figure 3. 2 H_c and S^* extracted from M-H loops of samples Ta5/Pd5/[Co t_{Co} /Pd t_{Pd}]9/Ta5 , where t_{Co} varied from 0.2 to 0.45 nm and t_{Pd} varied from 0.4 to 1.2 nm.

3.3.1.2 Pd thickness fixed, Co thickness varied

In addition to the out-of-plane M-H loops, the in-plane M-H loops for Co/Pd MLs with $t_{\text{Pd}}=0.4$ and t_{Co} ranging from 0.2 to 0.45 nm are shown in Figure 3.3. The M_{st} values increased

linearly with increase of Co thickness for all the samples with Pd thickness ranging from 0.4 nm to 1.2 nm. The in-plane loops showed hard-axis behavior. The perpendicular anisotropy for this type of material can be determined by $K_u \text{ eff} = M_s(H_k + 4\pi M_s)/2$, where M_s is the saturation magnetization of the entire ML from out-of-plane M-H loops. The total thickness is taken into account for the calculation of the magnetization because the Pd atoms adjacent to the interface were polarized and the anisotropy field H_k was estimated from the saturation field of the in-plane loop [87]. M_s ranged from 370~438 emu/cm³ for this set of samples, and $K_u \text{ eff}$ was in the range of 2.1~2.9x10⁶erg/cm³, as shown in Figure 3.3 (c), which was consistent with reports [86,87,92]. K_u increased first for low values of t_{Co} and then started to decrease when t_{Co} was larger than 0.35nm. It may be noted that, if M_s is replaced with the saturation magnetization of the Co layers only, the intrinsic anisotropy can be calculated with the same equation above. [87].

For the series of samples with Pd thickness of 0.4 nm, both out-of-plane and in-plane loops were measured. However, when the Pd thickness was larger than 0.6 nm, the in-plane loops could not be saturated with the maximum applied field of 18kOe in the AGM. However, it is reasonable to believe that the K_u values should be larger than those of Co/Pd MLs with $t_{Pd}=0.4$ nm.

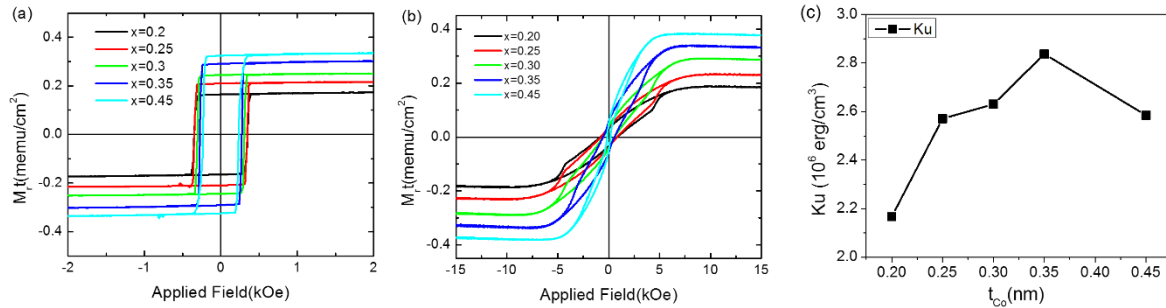


Figure 3.3 Out of plane (a) and in-plane (b) hysteresis loops of CPMLs with stack of Ta5/Pd5/[Co _{t_{Co}} /Pd 0.4]₉/Ta5, where t_{Co} ranged from 0.2 to 0.45 nm. (c) showed K_u dependence on t_{Co}

The dependence of H_c and M_{st} on t_{Co} is plotted in Figure 3.4. It was found that when the thickness of Pd was less than 0.6 nm, MLs with Co thickness of 0.25 nm had the maximum

coercivity. When the thickness of Pd was larger than 0.6 nm, the maximum coercivity was seen at a Co thickness of 0.3 nm, which may result from the increase in the demagnetization field as a consequence of higher Co concentration [91].

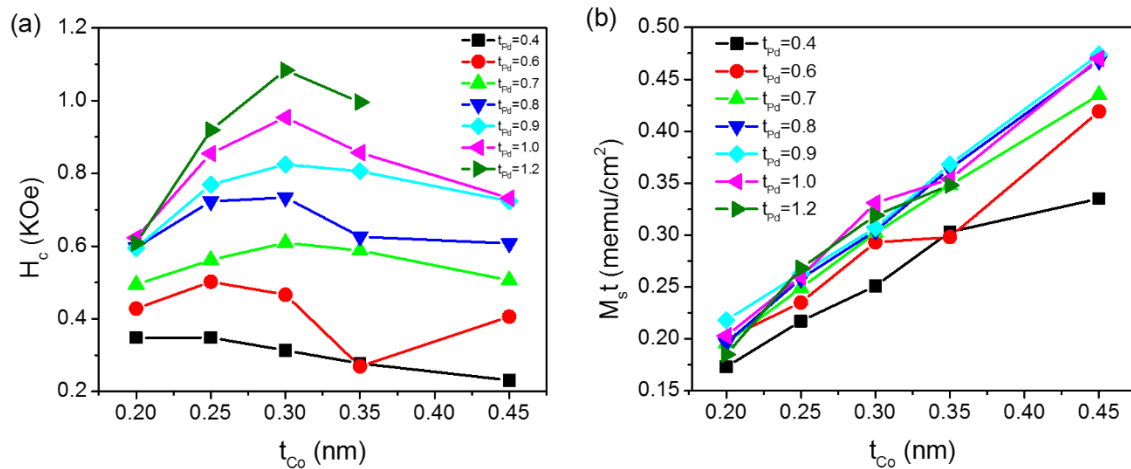


Figure 3.4 Plots of H_c (e) and $M_s t$ (f) for all the stacks of Ta5/Pd5/[Co t_{Co} /Pd t_{Pd}]₉/Ta5 where t_{Co} varied from 0.2 to 0.45 and t_{Pd} from 0.4 to 1.2 nm

The contour plot of coercivity as functions of Co thickness and Pd thickness in Figure 3.5 illustrated that samples with $t_{Co}=0.3$ nm and $t_{Pd}=1.0$ nm or $t_{Pd}=1.2$ nm have high coercivities. Therefore we chose bilayers of Co 0.3/Pd 1.0 nm or Co 0.3nm/Pd1.2 nm as the best combinations for further studies unless noted otherwise.

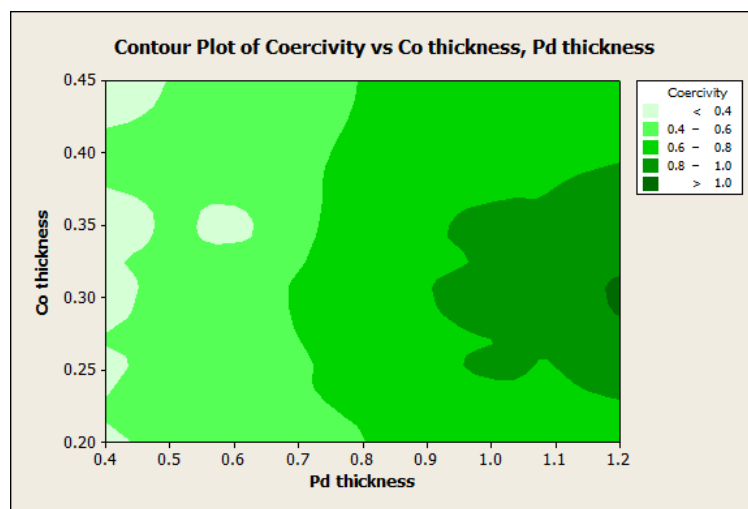


Figure 3.5 Contour plot of coercivity H_c vs. thickness of Co and Pd

3.3.2 Effect of Seed Layers

It has been reported that seed layers play a very important role for controlling magnetic properties of Co/Pd MLs with strong PMA. [2,3,8,16,17]. In our study, Co/Pd MLs with stacks of [Co0.3/Pd1.2]₉ were deposited on Si(100) substrates with the following seed layers: Ta10 nm, Pd10nm, Ta5 /Pd5 nm, Ta5 /Ru5 nm. M-H loops in Figure 3.6a show that all the films have strong PMA, since the loops are very square. Co/Pd ML with Ta5/Pd5 seed has the highest coercivity 1.1 kOe, while the others showed similar behavior. The determination of switching field distribution (SFD) was done by numerically differentiating the hysteresis loops and fitting it to a Gaussian distribution [93]. From the fitting, standard deviation σ (Oe) and average switching field H_{sf} ($\sim H_c$) were obtained and the relative SFD was calculated as $(\sigma/H_c) \times 100\%$. Figure 3b show the plots of dM/dH vs. H . SFD characteristics are listed in Table 3.1. It is evident that CoPd MLs with Ta5/Pd seed layers had smaller SFD, therefore, sharper switching characteristics.

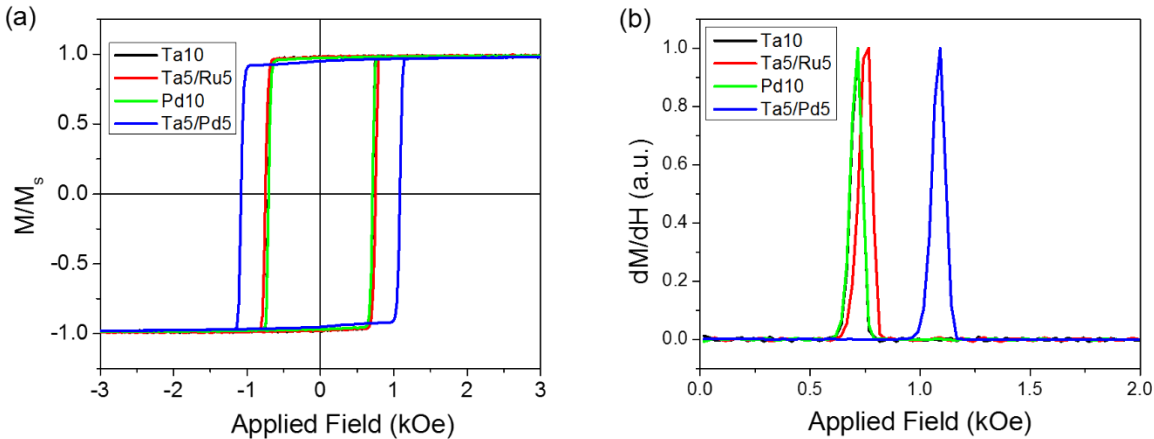


Figure 3. 6 (a) M-H loops and (b) SFD of Co/Pd MLs with different seed layers

Table 3. 1 Switching field distribution of Co/Pd MLs with various seed layers.

Seed layers	SFD(Oe)	Hc (Oe)	SFD (%)
Ta 10nm	30.9	722	4.3
Ta5/Ru5nm	29.2	723	4.0
Pd 10nm	31.3	757	4.1
Ta5/Pd 5nm	31.8	1092	2.9

Figure 3.7 shows XRD and XRR spectra for Co/Pd MLs with different seed layers. It can be seen that the Ta5/Pd5 sample had a strong Co/Pd (111) peak at $2\theta=40.7^\circ$, which is consistent with previous reports [87, 94, 95, 100, 101]. This peak was actually hcp α -Co(100), shifted from $2\theta=41.7$ and fcc Pd (111), shifted from $2\theta=40.4^\circ$, attributed to interfacial strain between ultrathin Co and Pd layers induced in the film during the deposition, which was believed to be the origin of high PMA. [93, 95]. Ta 10 nm, Ta5/Ru5 nm seed layers also promoted (111) texture, but not as strongly as the Ta5/Pd5 seed layer did, while the sample with Pd seed layer only showed a very weak (111) peak. From the XRR spectra in Figure 3.7 (b), it may be seen that all the samples showed regular fringes, indicating the multilayer structure. Carefully examination revealed that superlattice peaks were visible [96].

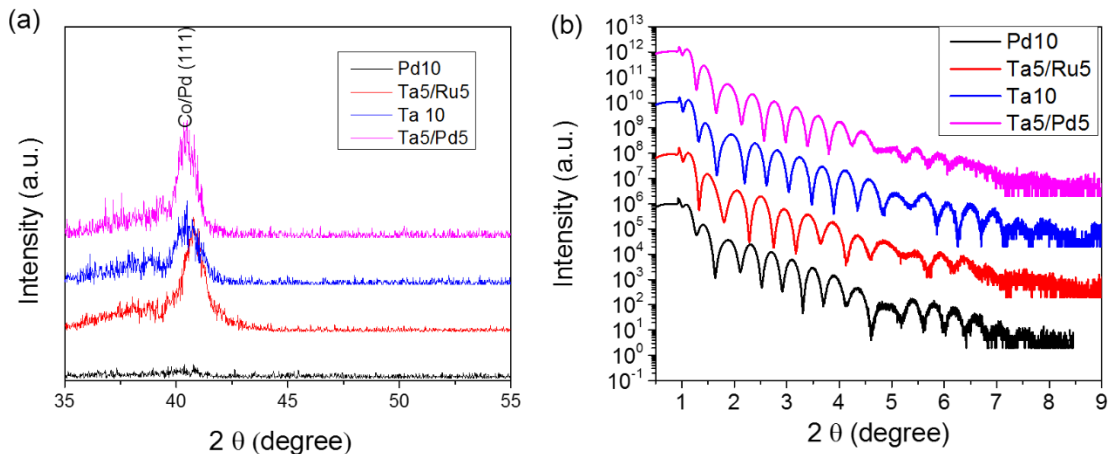


Figure 3. 7 (a) XRD and (b) XRR spectra of CPMLs with different seeds.

3.3.3 Effect of Bilayer Numbers

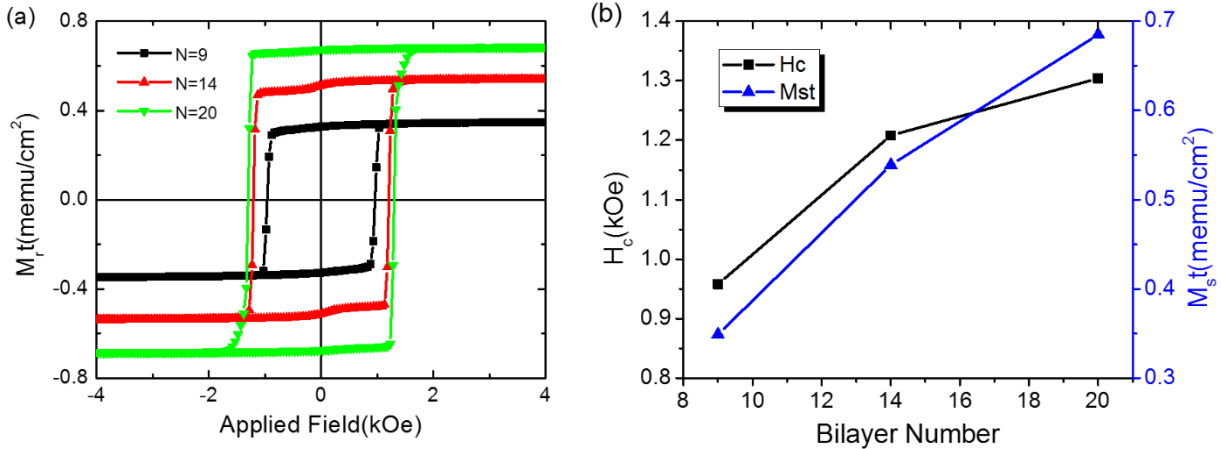


Figure 3.8 (a) Out of plane hysteresis loops of Co/Pd MLs with different bilayer numbers. (b) H_c and M_{st} dependence on bilayer numbers.

Out of plane hysteresis loops of Co/Pd MLs with a stack of Ta5/Pd5/[Co0.3/Pd1.0]_N/Ta 5, where N was varied, are shown in Figure 3.8. All the films showed strong PMA with square out-of-plane M-H loops. The coercivity H_c gradually increased with N. M_{st} increased linearly, as expected. The slopes of the loops below and above H_c represented the magnetization reversal process. For Co/Pd MLs with bilayers of 14 and 20, sharp magnetization was observed while a tail in the loop was observed when N=20. It was generally believed that two steps of magnetization reversal occurred, domain nucleation and domain wall motion. [86,87,97]. If the nucleation field H_n is lower than the wall propagation field H_p , reverse domains will nucleate with a reversal field of H_n . However, magnetization reversal will not be completed until the applied field reaches H_p . This is the case when N=20. If H_n were higher than H_p , the reversal would occur and be completed when the field reached H_n . [98]. Thus, only single step switching was observed for N=9. From XRR spectra shown in Figure 3.9, regular fringes were observed for all the samples, which was a good indication of the multilayered structure. With N increasing, the interfacial roughness increased and the conformality was lost. [96].

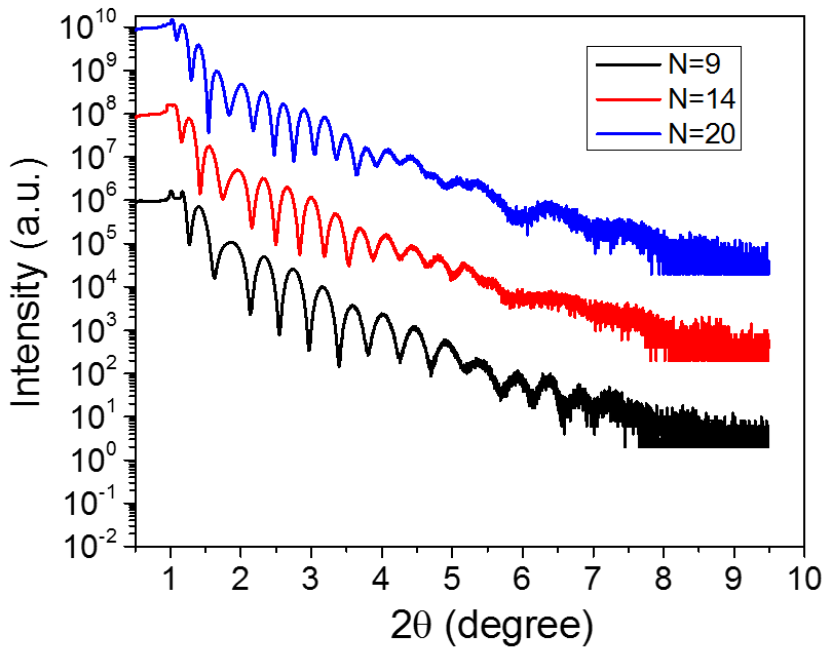


Figure 3.9 XRR spectra of CPMLs of Ta5/Pd5/[Co0.3/Pd1.0]_N/Ta5 with different bilayer number

3.3.4 Same Total Thickness Same Thickness Ratio, Bilayer Number Varied

In this section, we further studied effects of the number of bilayers, while keeping the Co/Pd thickness ratio and total thickness unchanged. The Co/Pd thickness ratio was maintained at 0.3 nm and the total thickness of Co/Pd MLs ranged from 11.7-12.9 nm. Co/Pd MLs with stacks of [Co 0.15/Pd 0.5]₁₈, [Co 0.2/Pd 0.7]₁₃, [Co 0.25/Pd 0.83]₁₁, [Co 0.3/Pd 0.9]₉, [Co 0.4/Pd 1.33]₇ and [Co 0.5/Pd 1.65]₆ were deposited on a Ta 5/Pd 5 nm seed layer on silicon substrates. A capping layer of 5 nm Ta was deposited on top of the Co/Pd MLs. The out-of-plane hysteresis loops shown in Figure 3.10 indicate the easy-axis features. It may be seen that the coercivity increased from 567Oe to 964 Oe with increasing numbers of bilayers, N, from 6 to 9, and then decreased with further increase of N. In other words, the coercivity increased with decreasing thickness of bilayers

from 2.15nm to 1.3nm and then decreased with a further decrease in thickness. Therefore, the coercivity depends not only on bilayer numbers but also on the thickness of each layer.

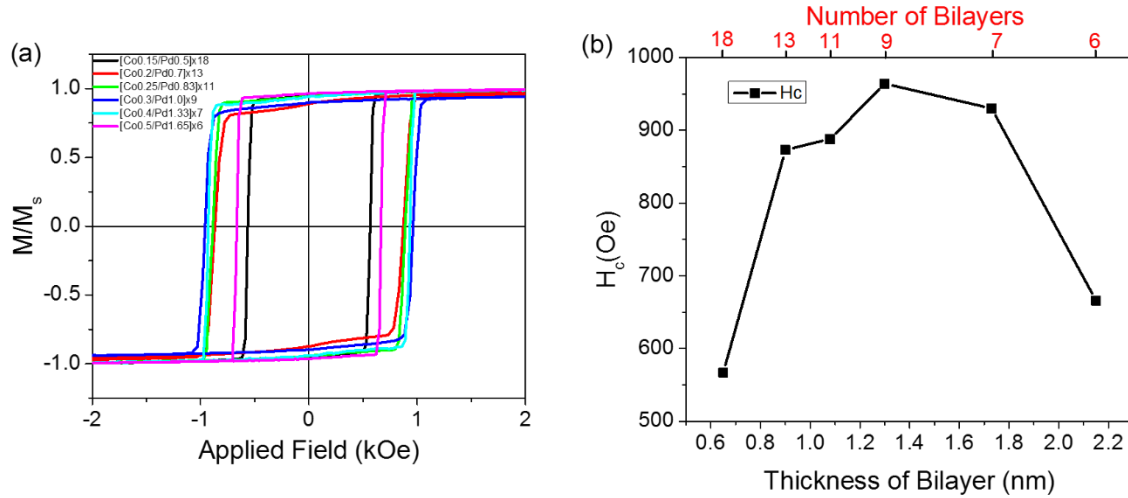


Figure 3. 10 (a) Out-of-plane M-H loops of Co/Pd ML with different bilayer thickness and bilayer number. (b) The dependence of H_c on bilayer number and bilayer thickness.

3.3.5 Same Thickness Ratio, Same Bilayer Number, Bilayer Thickness Varied

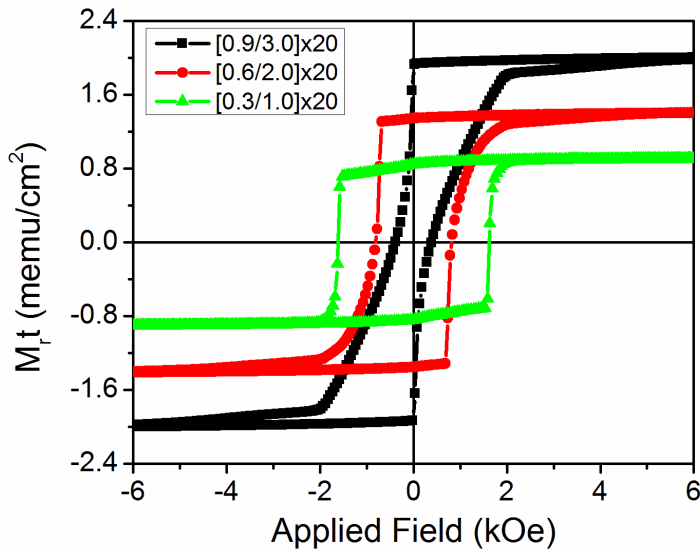


Figure 3. 11 Out-of-plane M-H loops of Co/Pd ML with 20 bilayers but different bilayer thickness

As seen in Figure 3.11, out-of-plane M-H loops of samples with stacks of Ta₅/Pd₅/[Co0.3/Pd1.0]₂₀/Ta₅, Ta₅/Pd₅/[Co0.6/Pd2.0]₂₀/Ta₅, Ta₅/Pd₅/[Co0.9/Pd3.0]₂₀/Ta₅ show PMA behavior, since S* is close to unity. With increasing the bilayer thickness, H_c decreased while M_{st} values increased as there were more Co in the samples. A great difference among the M-H loops was that thinner sample (Ta₅/Pd₅/[Co0.3/Pd1.0]₂₀/Ta₅) shows a sharp magnetization switching while the thicker sample (Ta₅/Pd₅/[Co0.6/Pd2.0]₂₀/Ta₅, Ta₅/Pd₅/[Co0.9/Pd3.0]₂₀/Ta₅) shows long tails in the hysteresis loops. It was believed that these tails originated from localized regions of residual domains that required higher magnetic field than H_c to annihilate [99].

3.4 Conclusions

In this chapter, a systematic study has been carried out to investigate the effects of Co thickness, Pd thickness, thickness ratio, seed layers and number of bilayers on the magnetic properties of Co/Pd MLs. The primary findings of this study are:

- 1) CoPd MLs with Co 0.3nm, Pd 1.0~1.2nm yielded the highest coercivity, while all the CoPd ML films with t_{Co} 0.2~0.45 and t_{Pd} 0.4~1.2 showed high squareness, which means high perpendicular anisotropy energy.
- 2) Ta 5/Pd 5 served as the best seed layer as it promoted more strongly (111) textured CoPd ML films than other seed layers and showed the smallest switching field distribution.
- 3) H_c increased with increasing bilayer number.
- 4) With the same total thickness of Co and Pd, magnetic properties depended not only on the bilayer numbers but also on each layer thickness.

Future work will focus on investigation of the dynamic properties of CoPd ML continuous films, as well as the effects of annealing and patterning.

Chapter 4 Nanopatterned Media by Nanosphere Lithography and Block Copolymer Lithography

4.1 Introduction

Bit patterned media (BPM) with high perpendicular magnetic anisotropy indicates great promise for overcoming the trade-off between thermal stability and recording writability to reach higher areal densities beyond traditional perpendicular continuous granular media [14,43,86]. In BPM each bit of data is stored in a discrete magnetic nanodot or nanopillar while a magnetic bit is composed of several grains in conventional recording media. A typical method to fabricate BPM is to pattern pre-deposited magnetic continuous films via lithographic methods, such as e-beam lithography, nanoimprinting, nanosphere lithography, block copolymer templating [44, 45, 47, 51]. In e-beam lithography, nanodots are defined by electron beam one by one. It has high precision, but it is time-consuming and expensive. In nanoimprinting, master molds are produced by e-beam lithography. In contrast, NSL and BCP templating are much more economical and highly accessible for media fabrication with large surface areas.

[Co/Pd] multilayers are very promising for BPM due to its high perpendicular magnetic anisotropy (PMA) and controllable magnetic properties [50, 88, 102]. Therefore, we used BCP and NSL processes to pattern magnetic Co/Pd multilayers. Starting with larger nanospheres of about 900nm and later focusing on BCP with 10~20nm size, we found that BCP is more suitable for higher density media. In addition, CoPt film was also patterned by BCP lithography. Co/Pd multilayers were also deposited on polystyrene spheres (PSS) of different sizes.

4.2 Experiments

Based on a previous study in our group [66, 90], Co/Pd multilayers with stacks of [Co0.3 nm /Pd 1.0 nm]₉, [Co0.25/Pd0.83]₁₁, [Co0.3/Pd1.0]₁₄ and [Co0.3/Pd1.0]₂₀ (thickness in nm) were deposited onto Si (001) substrate from elemental targets using a SFI Shamrock planetary sputtering system. The Si(100) substrates were used as received without further treatment. Ta 5nm/Pd 5nm bilayers were used as the seed layer to promote Co/Pd (111) texture structure and a 5 nm of Ta layer was used as a capping layer to prevent oxidation. The thickness of each layer was calculated by a pre-determined deposition rate. The base pressure prior to deposition was 5×10^{-8} Torr and the deposition pressure was fixed at 2 mT.

For NSL, in order to have uniform monolayers over a large area, we patterned grid lines to assist self-assembly of the polystyrene spheres (PSS). 3 μm wide grid lines, which were fabricated by the photolithography process, divided the surface into 300 $\mu\text{m} \times$ 300 μm areas. Then a PSS solution was prepared and spin-coated by a modified process from the literature [43, 103]. 100 μL Triton X-100 diluted by methanol (0.25 vol.%) and 0.2 ml PSS (D~900nm and 300 nm) solution with 1 ml methanol were spin-coated on these pre-cut 2 cm x 2 cm silicon wafer pieces or magnetic film with grids. Spin-coating was finished by a 3-step process [103]: 400 rpm for 10s to spread the PSS evenly, 1000rpm for 2 minutes to spread out the excess solution, 1600rpm for 10 s to spread away the excess beaded solution on the edge. The samples were then ashed in oxygen by a plasma ashing (referred to as ashing) or by a reactive ion etcher (referred to as RIE) to tune the size. These PSS with tuned size were used as etch masks during ion milling of the films.

For BCP, polystyrene (PS)-*block*-polyferrocenylidimethylsilane (PFS) (Polymer Source Inc.) was employed to pattern magnetic films, in which the organometallic PFS spheres were formed in a PS matrix. The PS-*b*-PFS have a molecular weight of 55 kg·mol⁻¹ for PS and 13 kg·mol⁻¹

¹ for PFS. Filtered PS-*b*-PFS solutions (1.5 wt. % in toluene) were spin-coated on magnetic films or silicon wafers at a speed of 4500 rpm and then annealed at 140 °C for 48 hours. The annealing caused phase separation of the block copolymer and formed a monolayer of PFS spheres in a PS matrix [49, 104]. Then the PS was partially removed using a reactive ion etch system with an oxygen plasma and the coil power/ platen power of 350W/0W to expose the PFS spheres as an etch mask. The magnetic films were etched to transfer the patterns by RIE and ion milling. For RIE etching, we used a gas mixture of O₂ and CF₄ or pure Ar, the coil power was set at 350W and the platen power was varied from 0 to 100W. For ion-milling, we used Ar⁺-ion milling in an Intelvac system using an 8 cm Veeco ion source. Beam voltages ranging from 100 V to 300 V were used, with the beam current set at 65.4 mA, and etch angles ranging from 30° to 80° in order to satisfy the requirements for the planned Design of Experiments (DoE), and etch times were set at 2.5 minutes. Continuous films as well as patterned ones were annealed at 300°C under a vacuum of 5x10⁻⁵ Torr to study the annealing effect.

The morphologies of nanospheres, PFS-PS and patterned films were examined by scanning electron microscopy (SEM, JEOL 7000). Magnetic properties of continuous magnetic films and patterned media were investigated using an alternating gradient force magnetometer (AGM, PMC Micromag 2900).

4.3 Results and Discussion

4.3.1 Nanosphere Lithography

Nanosphere lithography is an economic and highly accessible fabrication method which can produce nanostructures on a large scale. As shown in Figure 4.1, the steps for this method are: 1) depositing the magnetic Co/Pd multilayer 2) forming a monolayer of polystyrene

nanospheres 3) shrinking the size of the nanospheres 4) etching the film with reduced nanospheres as a mask to form magnetic pillar arrays.[43]

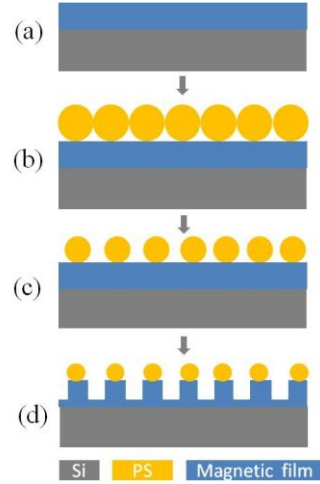


Figure 4. 1 Schematic of nanodots fabrication by NSL. a) Depositing magnetic thin film; b) spin-coating monolayers of PS; c) tuning the PS size by RIE or O₂ plasma asher; d) Etching the film by RIE or ion-milling.

4.3.1.1 PS Self-assembly

The typical morphologies of PS nanospheres with diameter of about 900nm are shown in Figure 4.2. The SEM data showed that the spin-coated beads were packed mostly as monolayers of hexagonally closed packed spheres in domains with size larger than 200 μm .

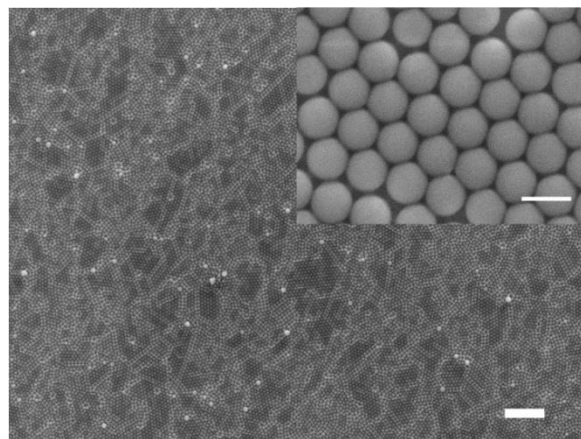


Figure 4. 2 Typical SEM image of a closely packed monolayer of PS with diameter of 900nm, the inset is the SEM image at higher magnification of 12000. Scale bars are in 1 μm .

4.3.1.2 Plasma Treatment

A plasma ash and reactive ion etcher were used to tune the size of PSS.

The samples were treated at 80W with oxygen flow rate of 2.5 sccm (sccm denotes standard cubic centimeter per minute) from 10s to 8 minutes. As shown in Figure 4.3, the PSS shrank as expected due to the oxygen plasma reacting with PS. In addition to the diameter variation, the nanospheres were found to interconnect with each other when etching 60s; however, the connection disappeared with further etching. In addition, the shape of PSS was changed to irregular shapes. This may be resulted from fragmentation of PSS and the minimization of the total free energy of PSS during the ashing. [44,102]. Figure 4.4 showed the diameter variation with oxygen plasma treatment time. As noted in the SEM pictures, the size decreased from their initial size with increasing time. However, it was found that etching rate decreased first and then increased. This is because during the initial etching, the nanospheres became flatter and the diameter became larger due to the roughening effect. Then the nanospheres were etched fast due to higher surface volume ratio.[43,103]

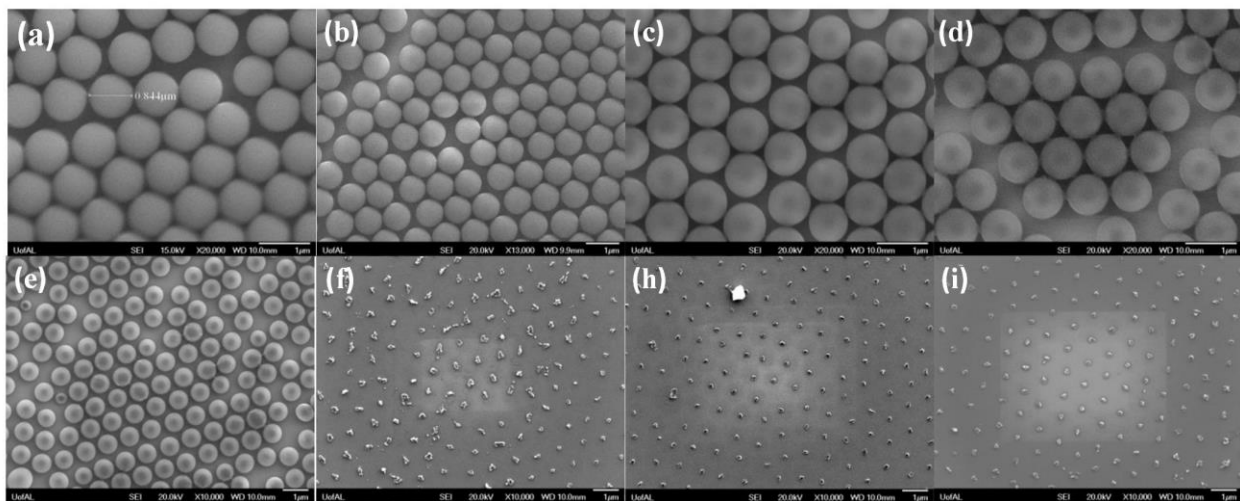


Figure 4. 3 SEM images of 900nm PSS by oxygen plasma treatment of periods from 10s to 12 minutes at 80W, (a) 10s, (b) 30s, (c)60s,(d) 90s(e) 2minutes, (f) 4 minutes, (h) 8 minutes and (i) 12 minutes. All the scale bars are 1 μ m.

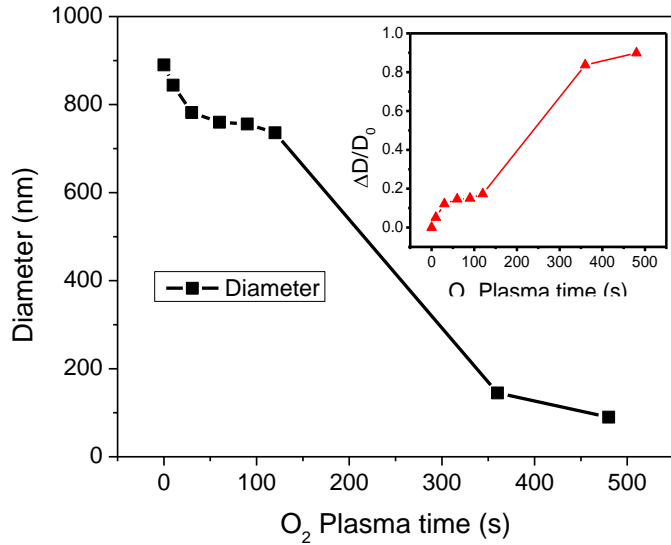


Figure 4.4 Diameter variation of PS as a function of ashing time. The inset showed the variation of the PSS size normalized by the initial size as a function of O₂ plasma time.

The PS beads were also tailored by reactive ion etcher (RIE) with coil power /platen power of 350W/0W and O₂ flow rate of 99 sccm. Figure 4.5 showed the SEM images of PSS changes with systematic increases in the RIE ashing time. In addition to what has been observed for PSS etched by O₂ plasma ashing, PSS were found to be hexagonal after 1 minute RIE. Further RIE etching made the PSS cupcake-like with diameter ~380 nm and then irregular shapes until removal. It was obvious that after 3 minutes RIE, the PSS were not able to serve as etching masks. Figure 4.7 showed size variation of PSS with RIE time while the inset showed $\Delta D/D_0$ as a function of RIE time. It was noted that the etching rate slightly increased with increasing RIE time, which is attributed to the increasing surface to volume ratio. [44, 103]

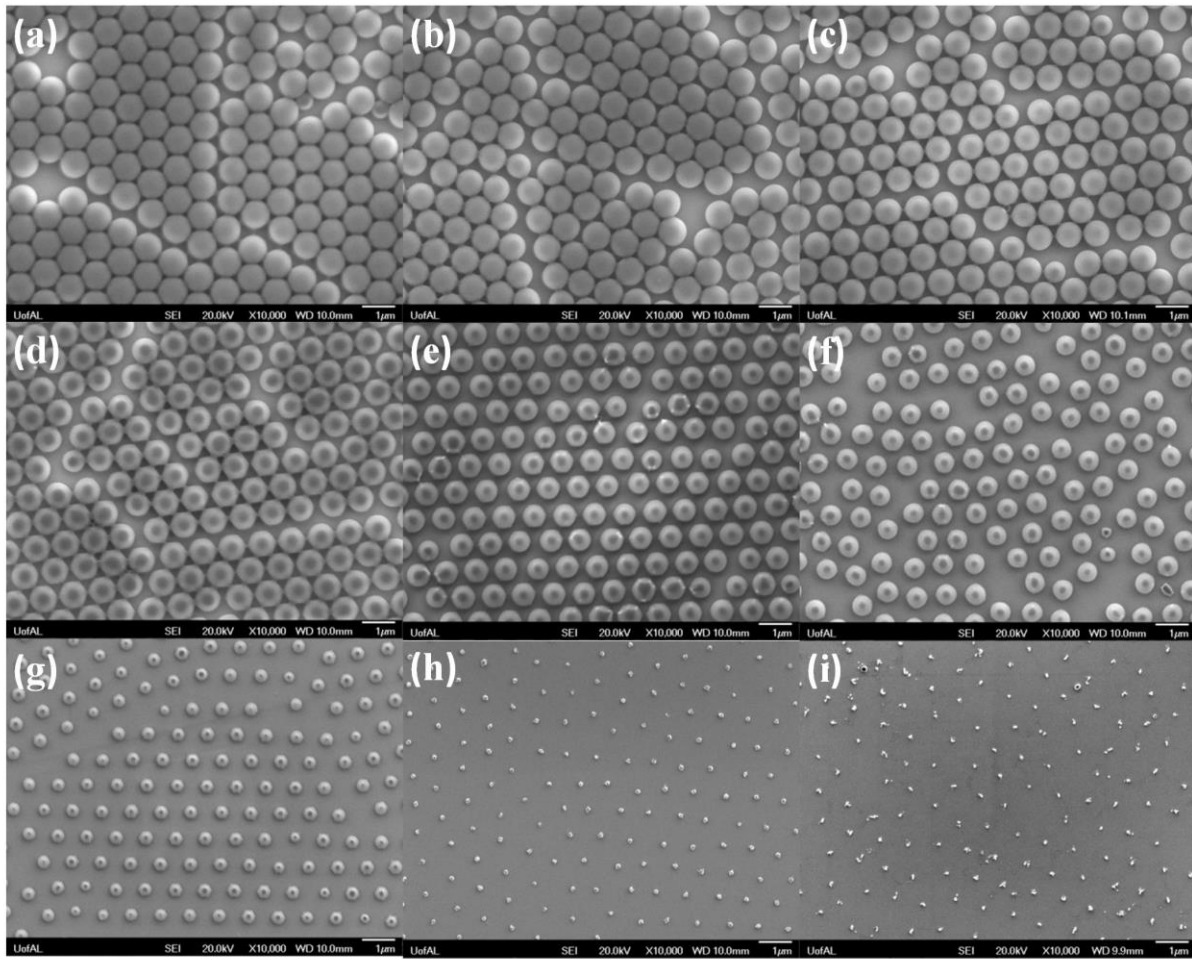


Figure 4. 5 SEM images of 900 nm PS beads treated by RIE with O₂ at 350W for (a) 10s (b)20s (c)40s (d)60s (e)90s (f)120s (g)180s (h)240s and (i)300s. All the scale bars are 1 μm.

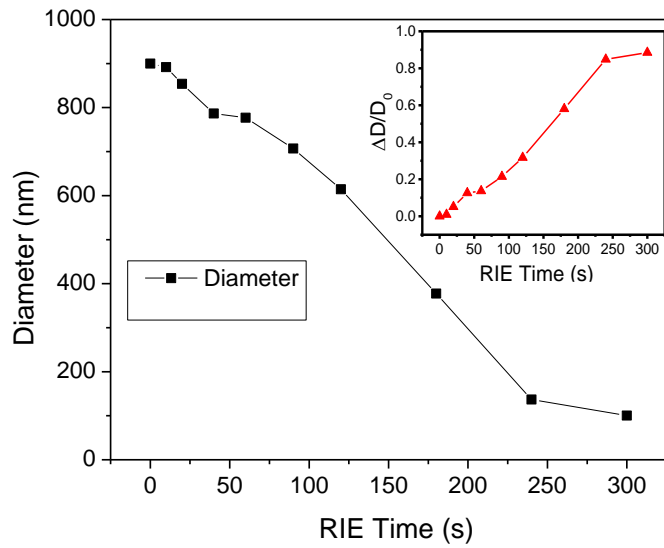


Figure 4.6 Size variations of PSS as a function of RIE time. The inset shows the size variation normalized by the initial size as a function of time.

PSS with diameter of 300nm were also used and tailored by RIE with coil power /platen power of 350W/0W. Similar morphologies were observed in Figure 4.7 and the size change as a function of RIE time was plotted in Figure 4.8. It can be seen that the change of size was almost linear and the ashing rate was about 2.1nm/s, which was roughly calculated from the slope of the plot.

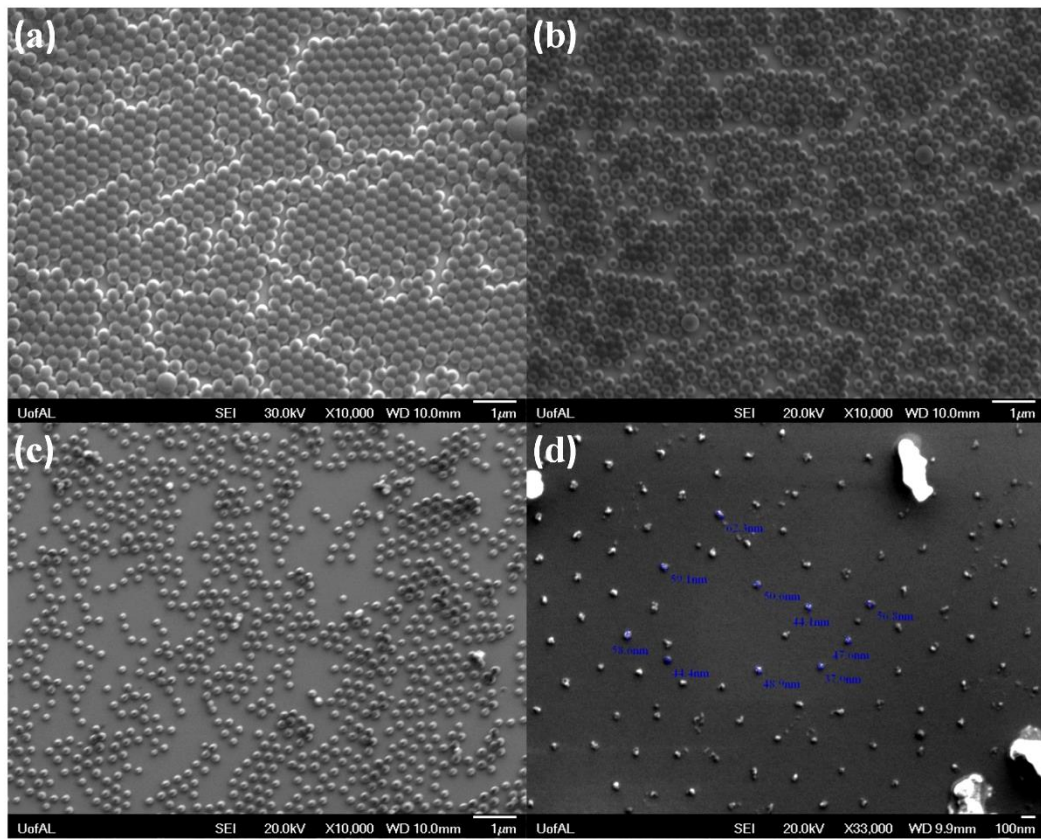


Figure 4. 7 SEM images of 300 nm PS beads treated by RIE with O₂ at 350W/0W for (a) 0s (b) 30s (c) 1min and (d) 2 min.

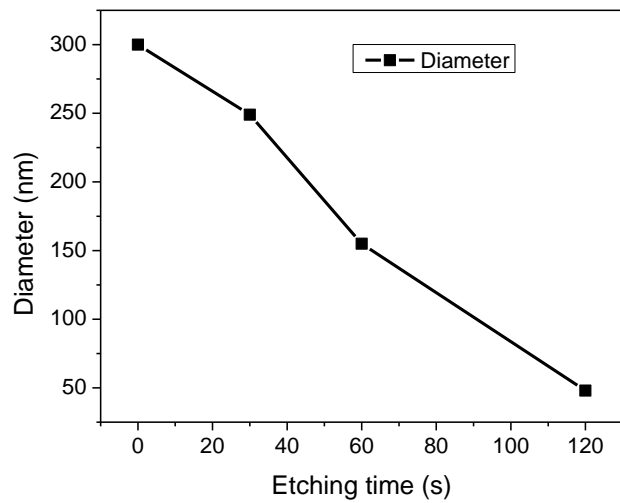


Figure 4. 8 Size variations as a function of RIE time.

Comparing the samples treated by oxygen plasma and RIE, we found that the RIE etched samples were reduced in a much more controllable way.

4.3.1.3 Pattern Transfer to Magnetic Layer

Following the oxygen plasma treatment of PSS, the samples were ion-milled at different beam power and etch angles. A typical SEM image of the sample, shown in Figure 7, which was ashed for 4 minutes by oxygen plasma in a plasma ashing and then ion-milled at 80 degree for 14W for 7 minutes, indicates the nanospheres were able to withstand the ion-milling, but were damaged into irregular shapes. The films were patterned to be nanobumps with a small aspect ratio, as the etch depth was very small compared to the diameter of the etch mask.

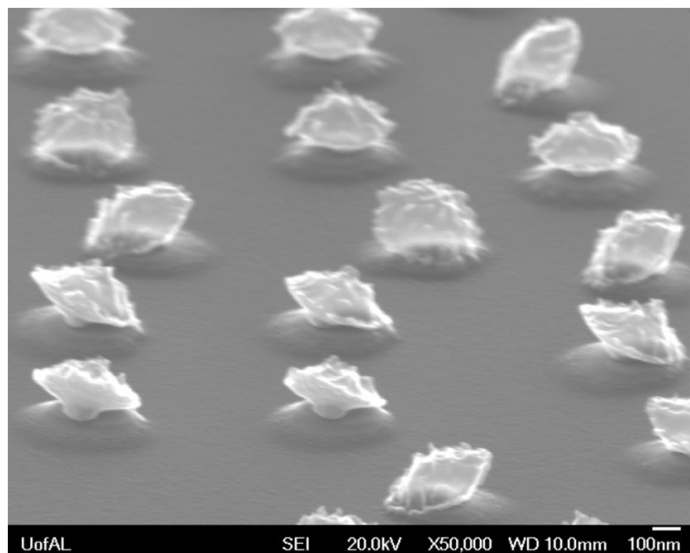


Figure 4. 9 Side-view of SEM image of the sample with stacks of Pd 10/ [Co0.3 /Pd1.0]₉/Pt 5 nm etched at 50°,14W for 7 minute after 4 minutes' ashing in the oxygen plasma.

4.3.1.4 Magnetic Properties

Magnetic properties were characterized by M-H loops which were measured by AGM. The as-deposited Co/Pd multilayered film with stack of [Co0.3nm/Pd1.0nm]₉ showed strong perpendicular anisotropy and a square M-H loop. After patterning, the M-H loops showed steps in

the coercivity, which may result from the shape of the nanopillar or the damage on the edge. The coercivity increased from 1.0 kOe to 2.0 kOe.

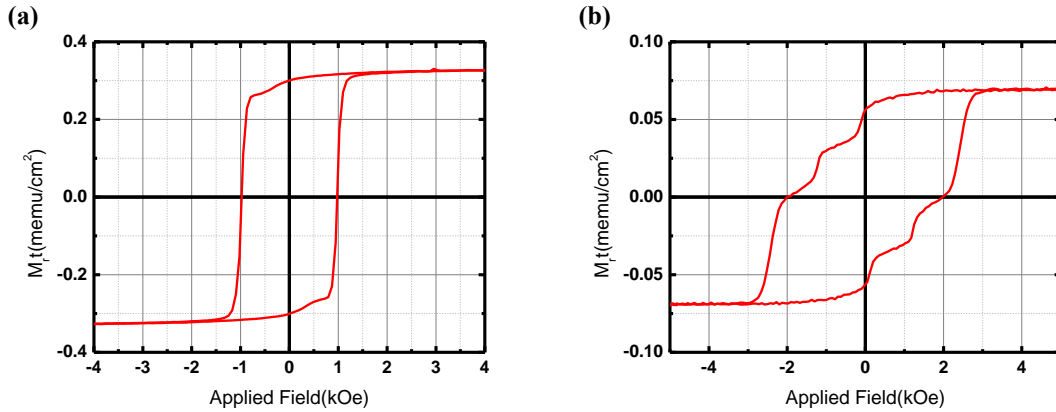


Figure 4.10 Out-of-plane of M-H loops of (a) continuous film and (b) patterned film with stacks of Pd 10nm/[Co0.3 nm/Pd1.0nm]_{x9}/Pt 5nm

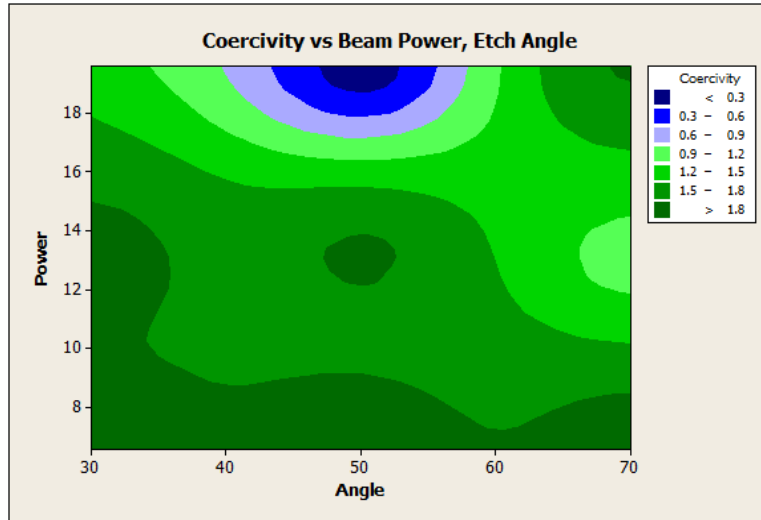


Figure 4.11 Contour plots of coercivity as a function of beam power and etch angle

A design of experiments (DoE) was carried out to determine the optimum combination of beam power and etch angle. The data extracted yielded the following contour plot (Figure 4.11). The plot indicated that low power or a combination of high power and high etch angle yielded high coercivities. This can be explained by etching rate and resistance of masks and the selectivity of etching between mask and film. The nanospheres used here were still very large, however. Using

PSS with 300nm and 100 nm is under investigation. Meanwhile block copolymer was employed to provide smaller masks.

4.3.2 Block Copolymer Assembly

Block copolymer self-assembly is also an inexpensive method for patterning. Similar to that of NSL, the steps for BCP are: 1) depositing the magnetic Co/Pd multilayer 2) Spin-coating a layer of BCP 3) Annealing to form PFS spheres in matrix of PS 4) Exposing PFS nanospheres by oxygen plasma treatment and 5) etching the film with PFS nanospheres as a mask to form magnetic pillar arrays. [49, 104]

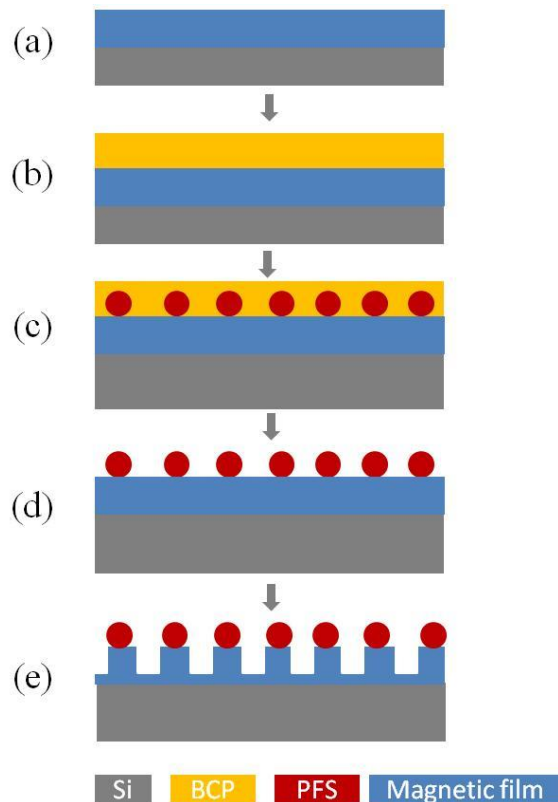


Figure 4. 12 Schematic of nanodots fabrication by BCP. a) Depositing magnetic thin film; b) spin-coating BCP of PS-b-PFS; c) Annealing to cause phase separation d) Exposing PFS spheres by O₂ plasma; e) Etching the film by RIE or ion-milling.

4.3.2.1 Exposing PFS by Plasma

We first removed the PS matrix partially by RIE for various times up to 4minutes, to expose the PFS spheres that were to be used as an etch mask. The SEM images in Figure 4.13 clearly showed that PFS nanospheres were exposed in the matrix of PS after 5s or longer time of RIE treatment in oxygen. The diameter of the PFS spheres was about 20 nm and the average center-to-center spacing was about 32 nm. It was noted that no significant change in the diameter of PFS was found when increasing RIE time in the test time periods from 5s to 4 minutes. Similar characteristics were found in the samples which were exposed by the oxygen plasma ashing, as shown in Figure 4.13 e and f. Therefore, it was confirmed that PFS effectively resisted the etching of the oxygen plasma so that only the PS matrix was removed.

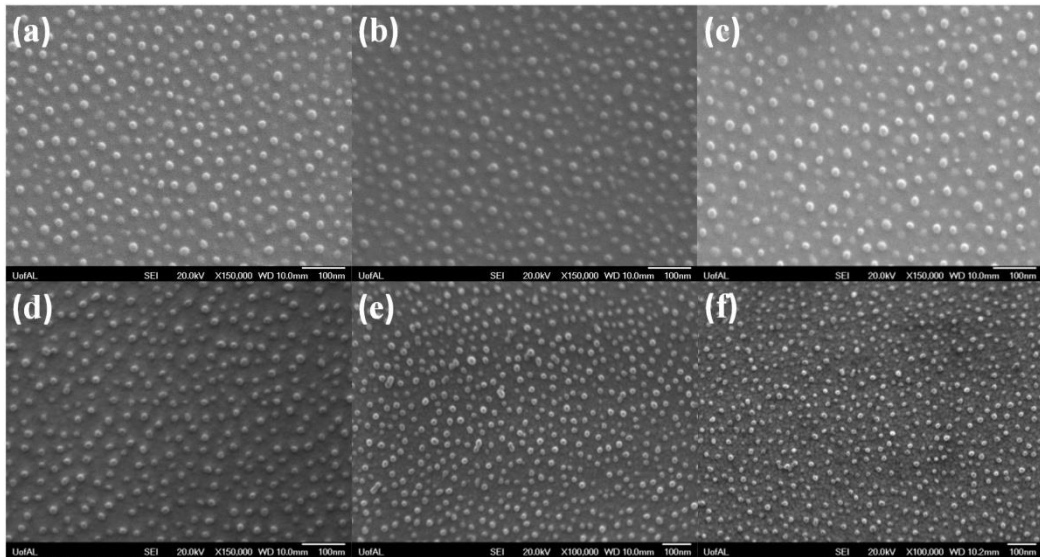


Figure 4. 13 SEM images of PS-PFS treated by RIE for (a) 5s, (b) 10s, (c) 15s and (d) 4 minutes, and by oxygen plasma ashing for (e) 45s and (d)90s.

4.3.2.2 Pattern Transfer

In order to determine the optimal ion-milling condition, a Design of Experiments (DoE) was carried out. Beam voltages ranged from 100 V to 300 V and etch angles ranged from 30° to 80°, and etch times were set at 2.5 minutes. As mentioned above, the PS matrix was first removed

from the film by oxygen plasma ashing to expose the PFS spheres that were to be used as an etch mask. Then the patterned film ion-milled at various conditions were imaged and measured to examine its magnetic properties. One sample was chosen to show the patterning and magnetometry, as seen in Figure 4.14. The PFS spheres did not appear to have survived the etching process as they were no longer visible; however they survived long enough to allow nanopillars to be fabricated. Ion milling at an angle of 55° , using a beam voltage of 300 V and 2.5 minutes, nanopillars of around 30 nm were obtained, which is larger than the 20 nm diameter nanosphere mask shown in Figure 13. This may be a result of the ion milling occurring at an angle, making the nanopillars more conical in shape. The increased size of the nanopillars could also be attributed to the disappearance of the PFS masks. [43]. The as-deposited Co/Pd multilayer film shows a very square out-of-plane loop with low coercivity of about 1.5 kOe while the coercivity of the etched sample increased to about 3.6 kOe. This also indicates that the film had been patterned into separate islands, resulting in exchange decoupling.

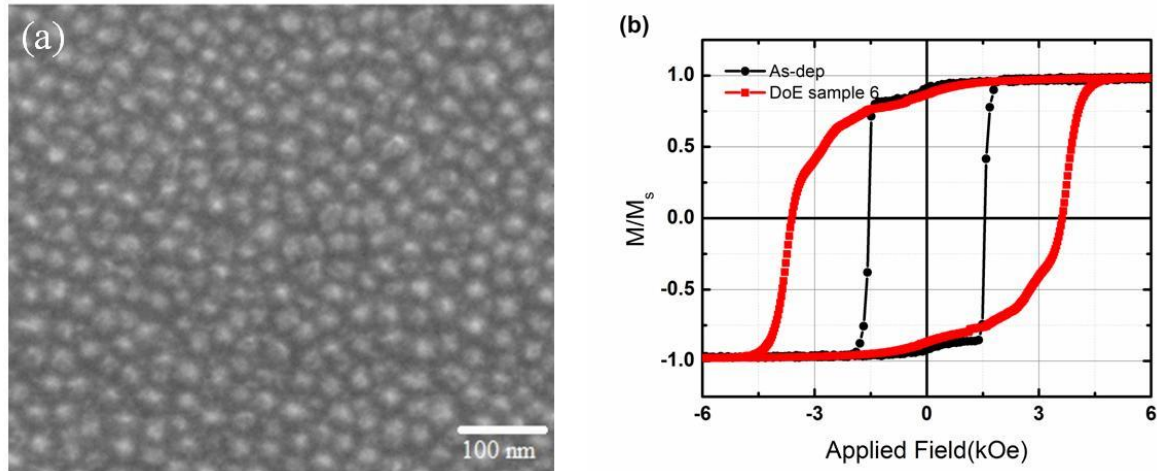


Figure 4. 14 SEM images of Co/Pd multilayered sample after etching at beam voltage 300V and etch angle of 55° and M-H loops for the same sample before and after ion-milling.

With all the samples measured and coercivities extracted from the hysteresis loops, the contour plot generated in Figure 4.15 shows that a coercivity greater than 3.5 kOe can be obtained

from a beam voltage of 300 V and an etch angle of 50°-60°. This corresponds with the maximum etch rate vs. angle, in agreement with theory.[106]

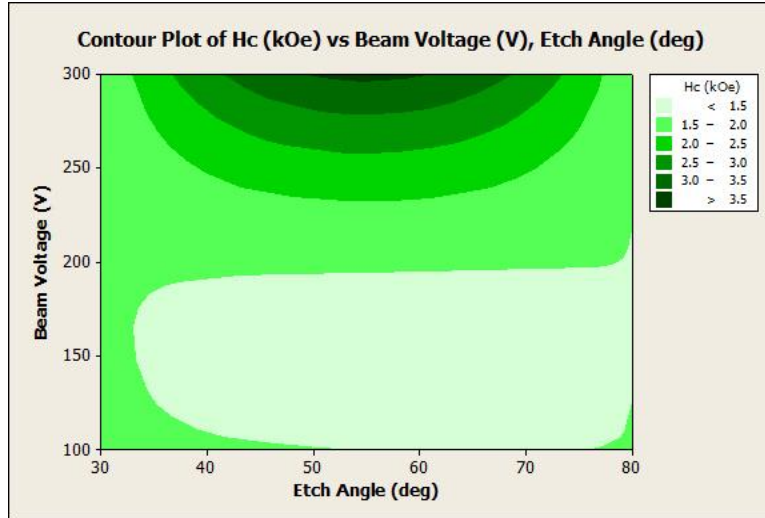


Figure 4. 15 DoE contour plot showing coercivity as a function of beam voltage and etch angle.

With the optimal ion-milling conditions, Co/Pd multilayered films with different stacks were ion-milled to study the evolution of morphologies and magnetic properties. Figure 4.16 showed the top-view and side view SEM images of films with stack of Ta5/Pd5/[Co0.3/Pd1.0]₁₄/Ta5 etched by ion-milling at 55° for different time. It can be seen clearly that after ion-milling, the patterns were successfully transferred to films. Nanopillars with conical shapes have been formed. The height of the nanopillars increased with etching time. It was also observed that the size of the nanodots was changed from 26±2.1nm for samples etched for 3minutes to 31.4±3.0nm for those etched for 3minutes, in agreement with report [43], which may result from the flatter mask with larger diameter features developed during etching.

Other Co/Pd multilayered films with different stacks, Ta5/Pd5/[Co0.25/Pd0.83]₁₁/Ta5 and Ta5/Pd5/[Co0.3/Pd1.0]₂₀/Ta5 were also patterned via the same procedure and similar morphologies were observed, as shown in Figure 4.17 and 4.18

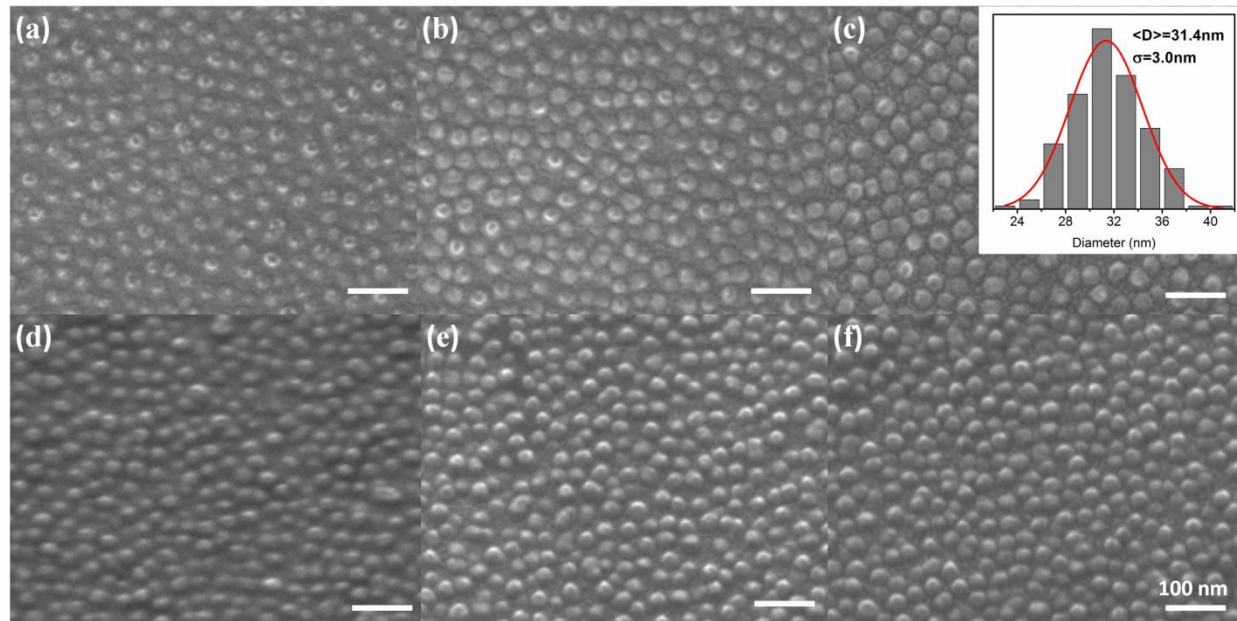


Figure 4. 16 SEM images of sample with stack of Ta5/Pd5/[Co0.3/Pd1.0]₁₄/Ta5 after ion-milled at 55° for (a)(d) 2minutes (b) (e) 2.5 minutes and (c)(f) 3 minutes . (a) (b) (c) are top-view and (d)(e)(f) are tilt-view. The inset in (c) shows the size distribution.

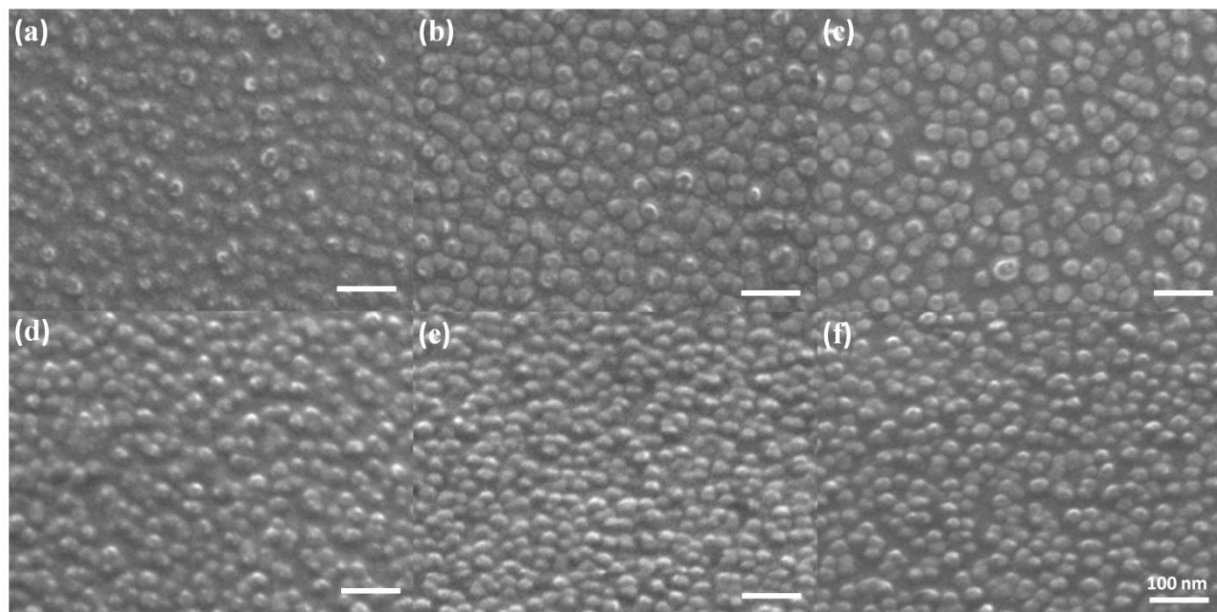


Figure 4. 17 SEM images of sample with stack of Ta5/Pd5/[Co0.25/Pd0.83]₁₁/Ta5 after ion-milled at 55° for (a) (d) 2minutes (b) (e) 2.5 minutes and (c) (f) 3 minutes. (a) (b) (c) are top-view and (d) (e) (f) are tilt-view. All the scale bars were 100nm.

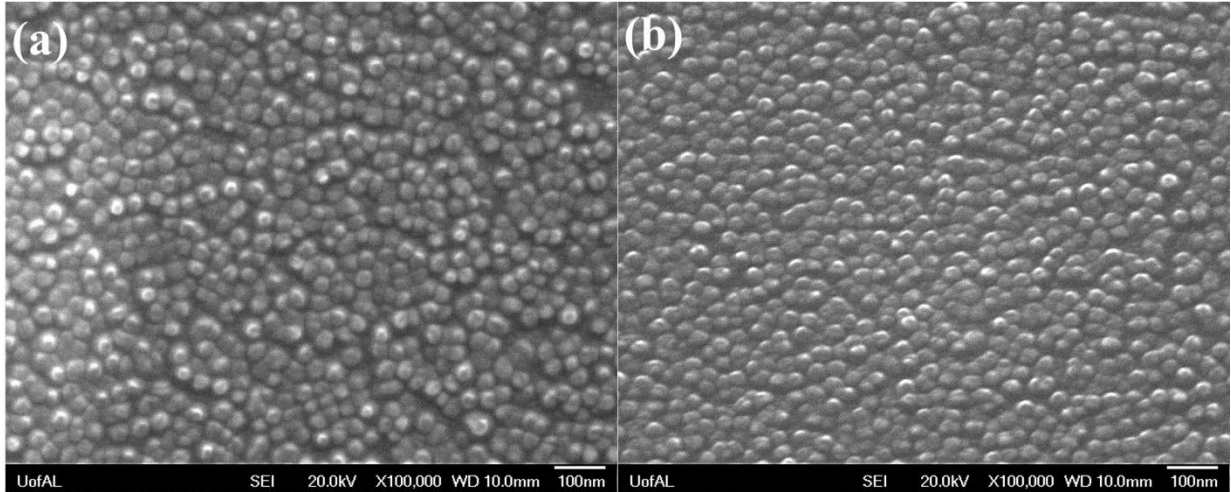


Figure 4.18 (a) Top view and (b) tilt-view SEM micrograph of CPMFs with stack of Ta5/Pd5/[Co0.3/Pd1.0]20/Ta5 after ion milling for 4 min.

4.3.2.3 Magnetic Properties

Out-of-plane hysteresis loops were measured and plotted in Figure 4.19 and 4.20. From Figure 4.19, it can be seen that the continuous film has a lower coercivity of 1.2 kOe and squareness of 1, due to the nucleation and domain wall motion switching mechanism [51,86]. After ion-milling 2 min, the coercivity increased slightly, although nanobumps have been observed, as shown in Figure 4.16. It is possible that only the capping layer of Ta was etched, so the switching mechanism for the film was not changed. The coercivity increased quickly and reached the maximum with one additional minute of ion-milling. Here it was believed that the switching mechanism of the film changed from domain wall motion to individual switching, resulting in high coercivity [86]. It was also noted that the switching field distribution increased, which may originate from the size distribution and anisotropy field distribution of these patterned magnetic nanopillars [99]. However, further ion-milling the sample did not continue to increase the coercivity, perhaps because the magnetic layer may be damaged by ion-irradiation.

Similar magnetic behaviors were observed, in Figure 4.20, that the coercivities of patterned film have been increased significantly from ~1.0 kOe to 4.6kOe. H_c increased with increasing

etching time and then decreased. The film was still continuous with initial etching and then became separated nanopillars while further etching removed all the magnetic materials or damaged them.

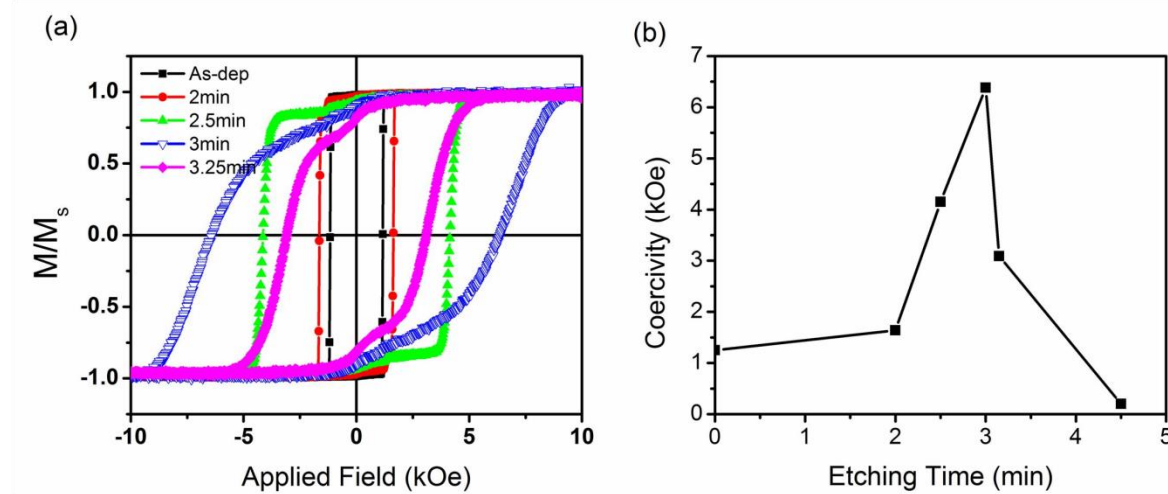


Figure 4. 19 (a) Out-of-plane and (b) H_c of samples with stack of $\text{Ta}_5/\text{Pd}_5/[\text{Co}_{0.3}/\text{Pd}_{1.0}]_{14}/\text{Ta}_5$ as a function of etching time by ion-milling at 55° .

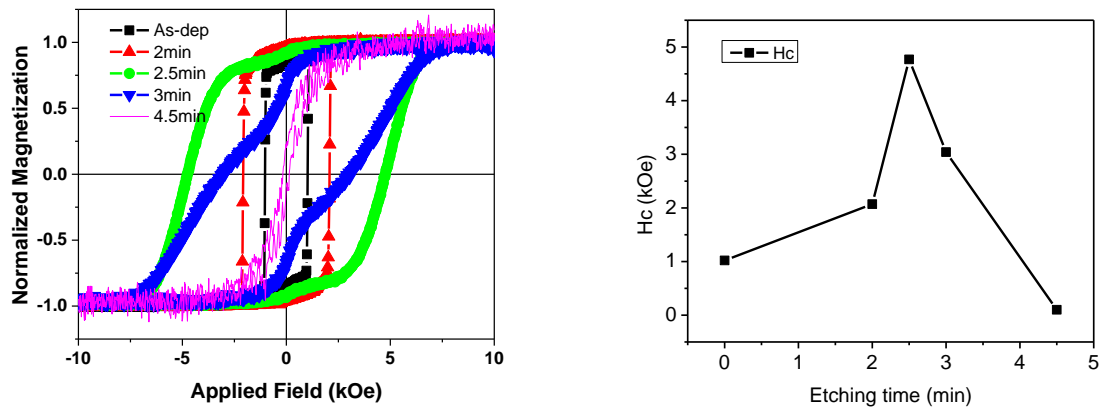


Figure 4. 20 (a) M-H loops and (b) H_c of samples with stack of $\text{Ta}_5/\text{Pd}_5/[\text{Co}_{0.25}/\text{Pd}_{0.83}]_{11}/\text{Ta}_5$ as a function of etching time by ion-milling at 55° .

In addition to studying the effect of longer ion milling times on the magnetic properties of the multilayer film, annealing effect was also studied. Several samples with 20 bilayers were ion milled using a beam voltage of 200 V, and an etch angle of 55° (for optimal etch rate and coercivity) with milling times ranging from 1 to 6 minutes. Samples milled for 1 to 4 minutes were annealed for 30 minutes at 300°C and a pressure of 4.5×10^{-5} Torr. The samples which displayed

decreased coercivity after ion milling, caused by excessive material removal, were excluded from the annealing. Figure 4.18 shows typical SEM images of Co/Pd multilayers with 20 bilayers after ion-milling. Magnetometry of the milled samples indicates that the coercivity reached a maximum at 4 minutes of milling, and then decreased, as shown in Figure 4.21. The post-annealing coercivity increased significantly compared to the as-milled samples for ion milling times of 1 to 3 minutes. It is possible that, after the Ta capping layer was etched away, the Co/Pd multilayers oxidized preferentially at the grain boundaries during annealing at 4.5×10^{-5} torr, leading to improved segregation of the nanopillars [107]. It is also possible that Co diffused into the Pd, which could also increase the coercivity [108]. However, there was no significant change seen after annealing for the sample milled for 4 minutes, which had the highest coercivity as-milled. The reason for this phenomenon is not clear. In order to achieve an increase in coercivity, a longer, higher temperature anneal may be needed. A statistically designed experiment on annealing, as well as rapid thermal annealing in high vacuum in the sputtering chamber, will be conducted in future.

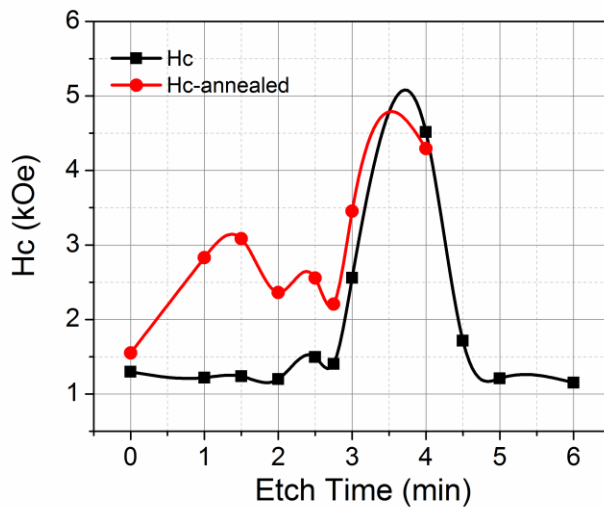


Figure 4. 21 Coercivity of ion milled samples before and after annealing as a function of ion milling etch time.

4.3.3 CoPt Patterned by BCP

Magnetic thin films with stacks of Ta5/ Ru50 / Co₄Pt 20/Ta5 were deposited by the Shamrock sputtering system [43]. CoPt was sputtered from an alloy target while others were from elemental targets. In order to identify the etching rates of each layer at the angle of 45° with voltage of 200V and current of 65mA, Ta, CoPt and Ru layers were deposited on silicon substrates, respectively. Then these samples were etched by ion-milling for different times. By measuring the resistance, the film thickness can be calculated according to $\rho = R_s \times t$ where ρ is in $\Omega\cdot\text{cm}$, R_s in Ω/sq and thickness in cm, assuming the resistivity was the same as the bulk value [109]. Then it was found that the etching rate under the condition of 45°, 200V and 65.4mA was 1.7nm/min for Ta, 3.7nm/min for CoPt and 5.2 nm/min for Ru.

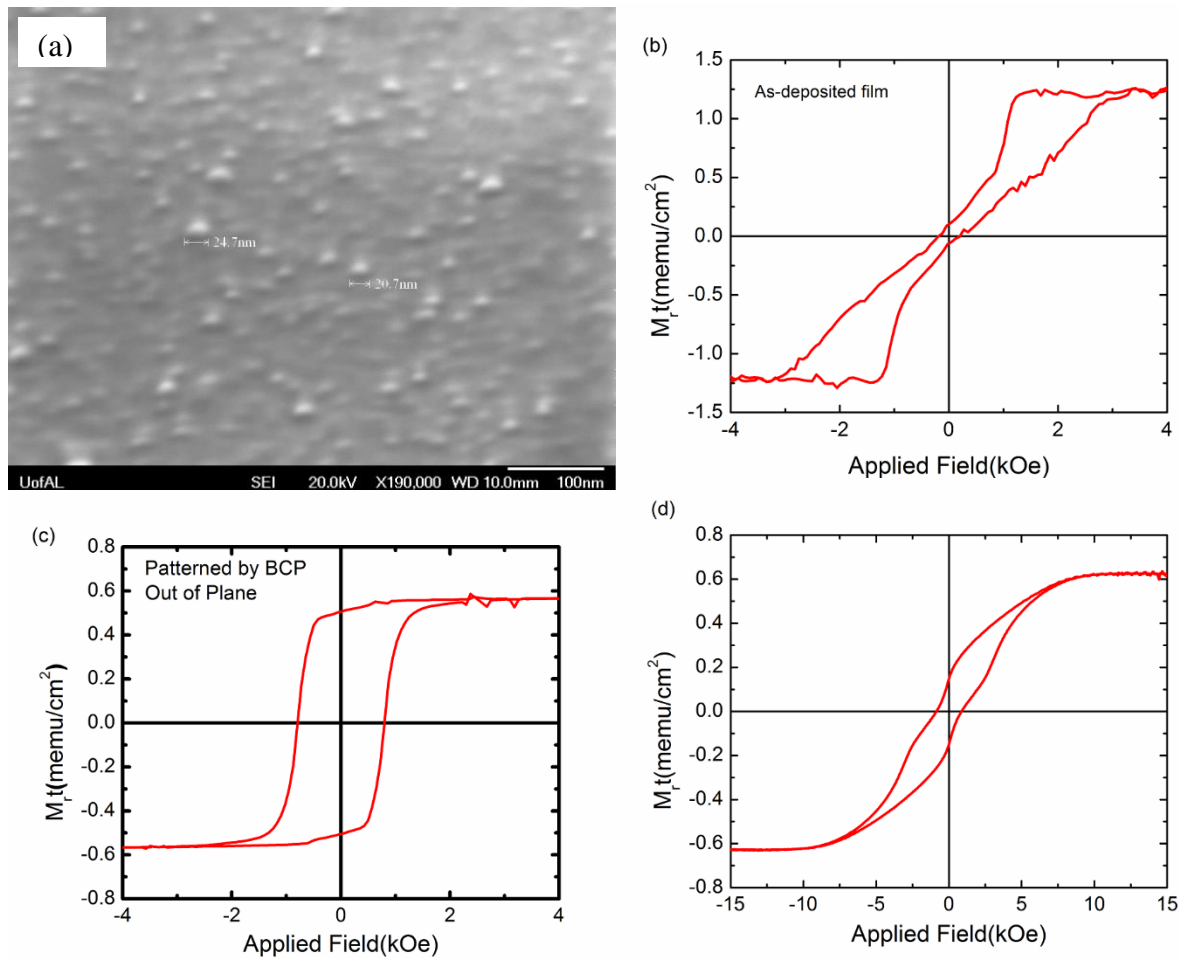


Figure 4. 22 (a) SEM image of CoPt dot array patterned with PFS-PS by ion-milling 45°-2min-80°-5min (b) out of plane M-H loops of as-deposited film, (c) out of plane and (d) in plane hysteresis loops of patterned sample.

4.3.4 Co/Pd MLs on PSS

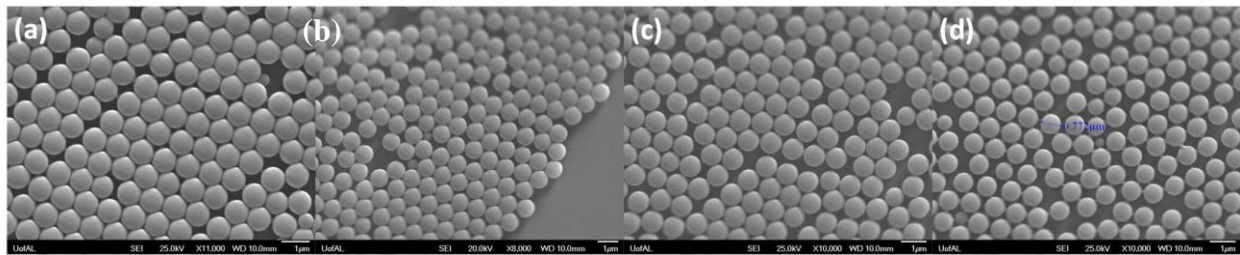


Figure 4. 23 SEM images of Co/Pd MLs on the PS which were ashed by oxygen plasma for (a) 0 s (b) 10s (c) 60s and (d) 120s.

As another method to fabricate nanopatterned media, the PSS monolayers were used as prepatterned substrate to deposit magnetic layers on top of them. Albrecht et al. have deposited Co/Pd MLs on 2-D PSS to achieve tilted media with a uniform oblique magnetic anisotropy and an unexpected switching behavior.[110,111] In this section, we studied the magnetic properties of Co/Pd MLs on PSS with different sizes. Two sets of Co/Pd MLs were deposited, Ta5/Ru10/[Co0.5/Pd0.5]x9/Ta5 and Pd10/[Co0.3/Pd1.0]x9/Pd10 (thickness in nm). Figure 4.23 showed the SEM images of MLs deposited on the PSS which were ashed by oxygen plasma for different times and resulting in different diameters. However, no significant difference was observed compared to corresponding PSS without Co/Pd MLs because the thickness of Co/Pd MLs were less than 30 nm while the diameter of PSS ranged from 600-850nm. Seen in Figure 4.24, M-H loops indicated a significant improvement in the magnetic properties, for instance, H_c and S^* . H_c increased from 60Oe for Co/Pd MLs on the silicon substrate to about 650Oe on the PSS which was ashed for 60s with a diameter of 760nm and S^* also increased from 0.2 to about 0.8, indicating enhancement of perpendicular magnetic anisotropy. H_c did not keep increasing as the PSS shrank to smaller sizes. It was also noted that the magnetization reversal for those films with PSS showed two-step switching, which is due to the continuous film between PSS switching first at smaller fields and those on PSS switching at higher fields.

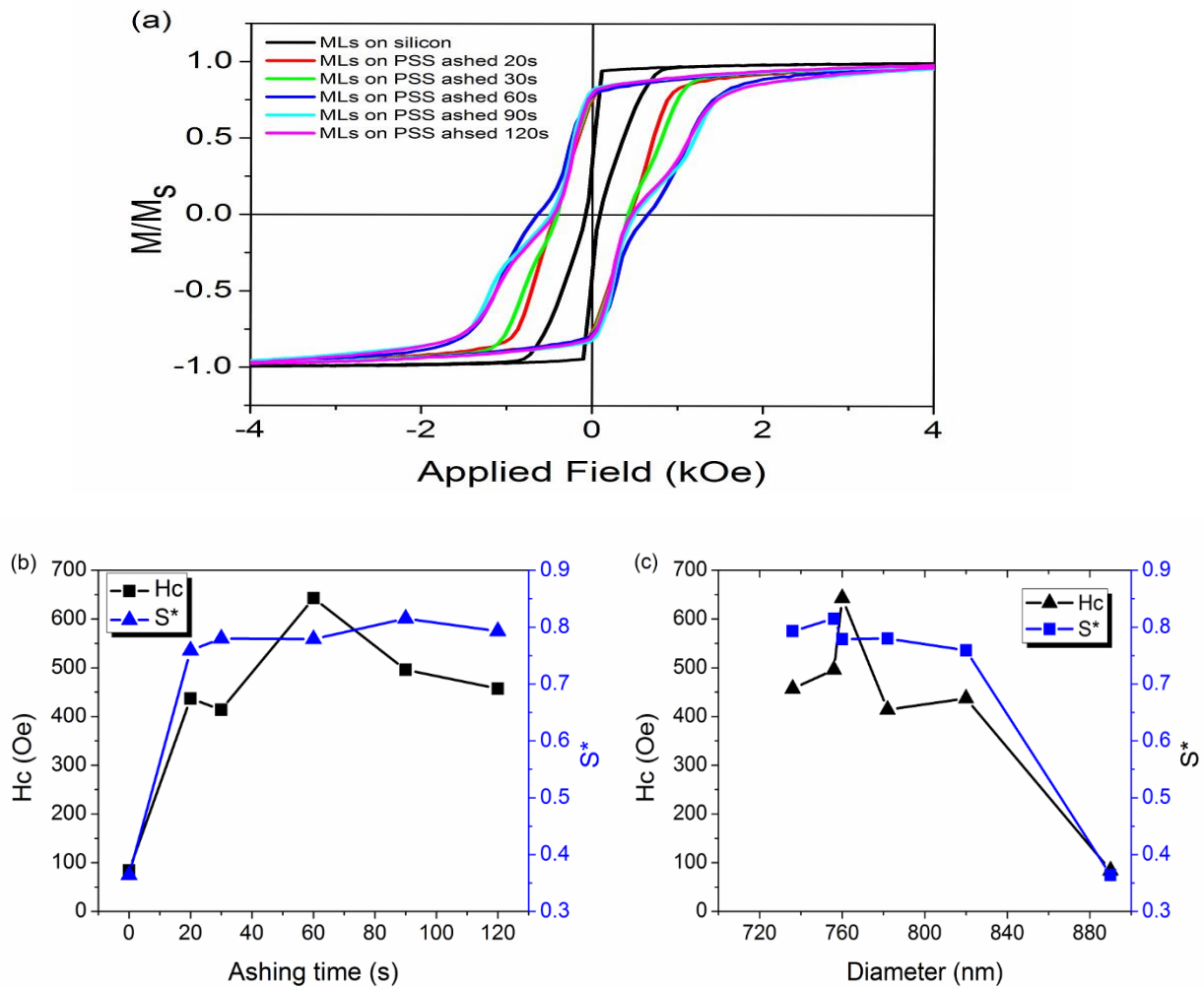


Figure 4.24 (a) out-of-plane M-H loops of Co/Pd MLs with stack of Ta5/Ru10/[Co0.5/Pd0.5]₉/Ta5 deposited on 900 nm PSS ashed for various time. (b) H_c as a function of ashing time; (c) H_c vs. PS diameter, corresponding to ashing time in (b).

4.4 Conclusions

In this work, we explored nanosphere lithography and block copolymer lithography for nanopatterning Co/Pd perpendicular multilayers and CoPt alloy. The principal findings of this study are:

- 1) For NSL, RIE tuned the size of PSS in a more controllable way than the plasma ashing.

- 2) For NSL, high power and high etch angle yielded higher coercivity, although 900 nm PSS was inadequate to serve as etching masks to pattern magnetic films for advanced media because of their large size.
- 3) For BCP, there was no difference between the plasma ashing and the RIE for eliminating the PS matrix and exposing the PFS nanospheres, which were highly resistant to the oxygen plasma.
- 4) Ion-milling was an effective tool to pattern the magnetic film over a large area. The best result showed a coercivity as high as 6.6kOe.
- 5) Annealing samples improved the magnetic properties for both continuous films and patterned ones, with the highest coercivity achieved being 2.9 kOe for a patterned film, a 93% increase over the as-etched film.
- 6) CoPt alloy films were patterned by BCP, the coercivity increased from 0.2 kOe to 0.8 kOe and S* from 0.2 to 0.9.
- 7) Deposition of Co/Pd multilayer on 900 nm PSS showed increased coercivity.

Chapter 5 Nanorods Fabricated by Glancing Angle Deposition

5.1 Introduction

Bit patterned media (BPM) is a promising technology for the next generation of information storage [14,43, 86]. Nanosphere lithography, e-beam lithography, and nanoimprint techniques have been studied to pattern magnetic films for BPM. [43-45,47,51] However, either additive patterning or subtractive patterning is a multiple-step process and cost ineffective, compared to conventional continuous media by sputtering. Therefore any method to simplify the patterning process is promising.

Glancing angle deposition (GLAD), which was first reported in 1959 [112,113] and developed in 1990s [52], is a physical vapor deposition method in which the incoming flux from the source impinges on the substrate at oblique angles , causing increased shadowing compared to normal incidence [53]. By rotating the substrate at certain speeds, it can produce nanopillars, zigzags, Y-shapes, helices [53-59,114]. However, most of these studies have focused on nonmagnetic materials with the potential application for photonic crystals [60,115], sensors [61] and optical nanoemitters [62]. Few magnetic materials have been studied for the purpose of information storage [63-65]. It will be of great importance to fabricate CoPt-AlN, Fe/Pt, FePt, Co and Co/Pd multilayered nanopillars for the purpose of high density information storage as a single-step process since nanopillars have been fabricated during the GLAD, rather than multi-steps patterning process.

5.2 Experiments

All the samples were deposited in the automated Shamrock sputtering system, which has 6 guns and 4 planets, as detailed in Chapter 2. All the metallic materials were deposited by dc sputtering, while AlN was sputtered by reactive sputtering the Al target with nitrogen. The base pressure prior to deposition was 5×10^{-8} Torr and the deposition pressure was maintained at 2mTorr. The distance between the substrate and targets was about 90mm. The sputtered atom flux was incident at angles ranging from 47° to 82° as the substrate presented itself at different angles to the target during the planetary deposition. All material fluxes were incident over the same range of angles. The sputtering power ranged from 90 W to 400W, with corresponding deposition rates of 0.02~0.83 nm/s. The thickness of the metallic layer was determined by profilometry and the thickness of the AlN was measured by spectrophotometry (Nanospec), both of which were confirmed by X-ray reflectivity (XRR). The deposition rate therefore was determined and the desired thickness of material could be deposited by varying the deposition time. It should be noted that for the flat film or normally deposited film, the wafer/substrate was placed parallel to the planet and therefore the incidence flux was perpendicular to the substrate. For the GLAD samples, the Si substrate pieces were placed normal to the planet, making an oblique angle between the incident flux and the substrate plane. Therefore the deposition rates of the GLAD films were found to be one third of those for the normal deposition. It is also worthwhile to point out that all the samples were deposited by planetary deposition unless specifically noted.

The morphologies of the samples were characterized by atomic force microscopy (AFM) and field-emission scanning electron microscopy (FE-SEM). The structures were characterized by X-ray diffraction (XRD) and roughness by X-ray reflectivity (XRR). The magnetic properties were

studied by alternating gradient force magnetometer (AGM) and vibrating sample magnetometer (VSM).

5.3 Result and Discussion

5.3.1 CoPt-AlN

We initially deposited thick CoPt and CoPt-AlN films and observed their structure as well as measured their magnetic properties.

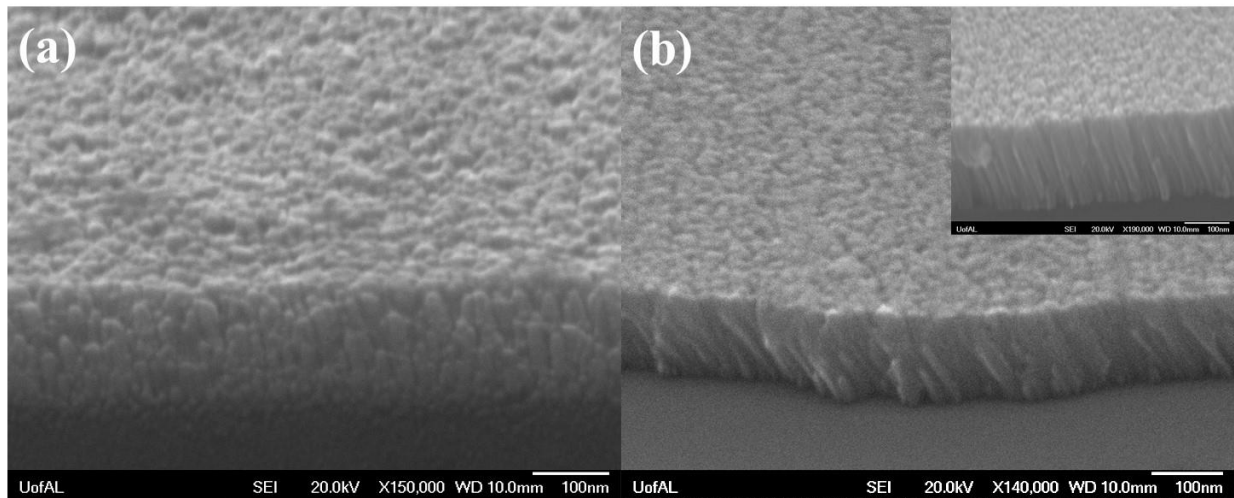


Figure 5. 1 Side-view SEM of GLAD samples of a) Ru 50/CoPt 350 nm and b) Ru 50/CoPt-AlN 350nm. The inset in Figure 5.1b showed nanorods in high magnification of 150,000.

It can be seen in Figure 5.1 that both CoPt (350nm) and CoPt-AlN (350nm) had nanocolumns, which were the desired structure. Subsequently the thickness of the magnetic film was reduced and a similar nanocolumn structure remained. Samples with stacks of Ta 5nm /Ru 50nm /CoPt-AlN(t nm)/Ta 5nm were deposited. Here Ta and Ru were employed as preseed layer and seed layer, respectively. Another 5nm Ta was used as a cap layer to protect the stack against oxidation. The volume of AlN was kept as a constant and the volume of CoPt was changed by changing the deposition power. The thickness t of CoPt-AlN layer varied from 52, 39, to 26nm, corresponding to the volume ratio of CoPt to AlN of 3:1, 2:1, and 1:1

Figure 5.2 is the side view SEM micrographs of CoPt-AlN samples with different thicknesses grown on a Si(001) substrate. It can be clearly seen that nanopillars have been formed. The diameter of the nanopillar is approximately 16 nm and the oblique angle is about 78 degrees. Three kinds of samples showed similar nanopillars. This can be explained by the atomic shadowing effect. The shadowing around the new nuclei suppresses growth, while adatoms diffuse at a relatively low rate at the deposition temperature [53].

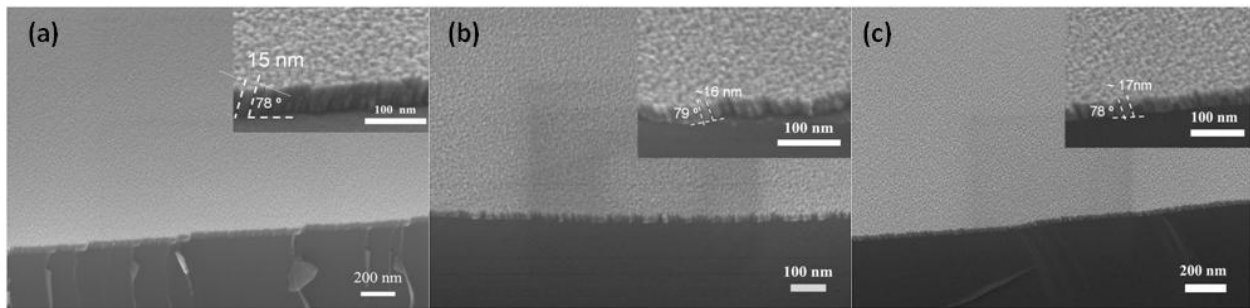


Figure 5. 2 Side-view SEM of GLAD sample of Ta 5nm /Ru 50nm /CoPt-AlN(t nm)/Ta 5nm.
(a) $t=52$ (b) $t=39$ (c) $t=26$

The EDX spectrum, shown in Figure 5.3, indicates the composition. As it was on the Si wafer, and the film was thin, EDS collected quite a large number of electrons from the silicon wafer. Therefore, the silicon content was very high. The error increased for other compositions as they were at a relatively low level. However, all the elements were detected.

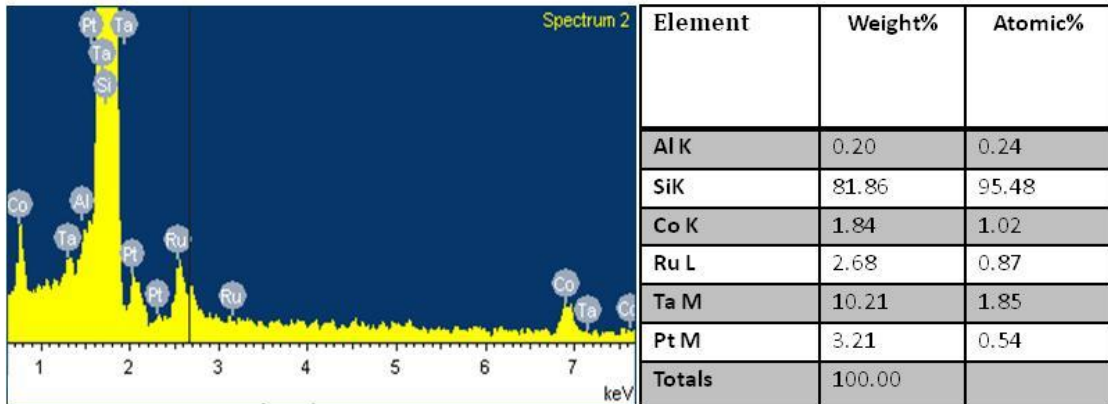


Figure 5. EDX spectrum and composition of Ta 5nm /Ru 50nm /CoPt-AlN(39 nm)/Ta 5nm

In order to gather insight into the magnetic behavior of the columns, room temperature magnetization measurements were performed on the samples using alternating gradient magnetometry (AGM). The flat sample ($t=39$), which was deposited at normal incidence, was also measured. The coercivity H_c increased from 0.152 kOe for the flat sample to 0.388 kOe for the GLAD sample. The remanence and squareness also increased significantly. This can be explained by its structure. As the GLAD sample was composed of nanopillars which induced shape anisotropy and the flat sample was a continuous film, the GLAD samples would show higher remanent magnetization and higher coercivity. The difference of saturation magnetization between the control sample and GLAD sample resulted from the fact that the flat samples were three times thicker than the GLAD samples. The squareness and coercivity of these samples are summarized in Table 5.1. It can be seen that GLAD samples have larger squareness and higher coercivity due to columnar structure. When the volume ratio of CoPt to AlN was 2:1, it yielded the highest coercivity and squareness. This may be caused by AlN distributed around the CoPt, thus decreasing the intergranular exchange coupling of CoPt.

Table 5. 1 Summary of squareness and coercivity of GLAD samples and Control samples.

Thickness	$V_{\text{CoPt}} / V_{\text{AlN}}$	Squareness		Coercivity (Oe)	
		Normal	GLAD	Normal	GLAD
t=52	1:1	0.008	0.042	9	17
t=39	2:1	0.068	0.251	152	388
t=26	3:1	0.052	0.217	204	207

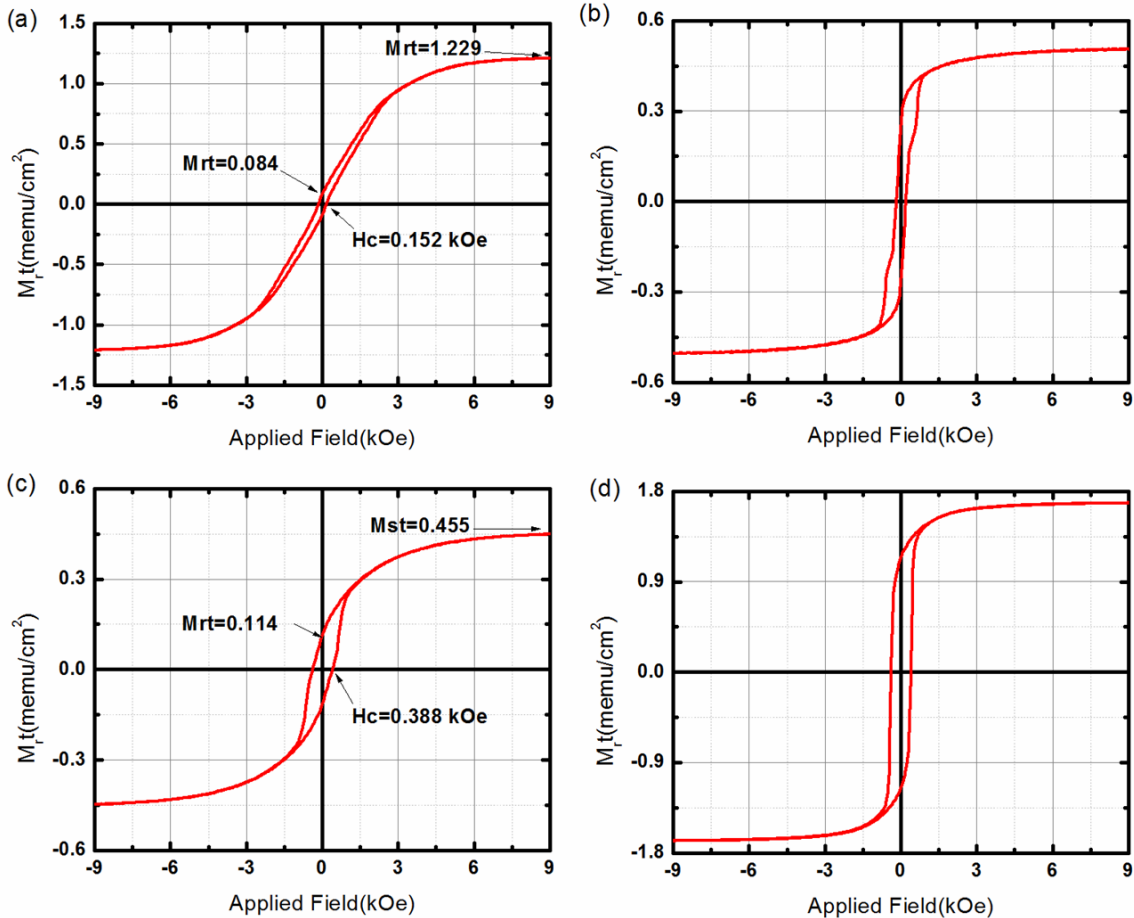


Figure 5. (a) Out-of-plane and (b) in-plane of hysteresis loop normally deposited sample (t=39) and (c) out-of-plane and (d) in-plane of hysteresis loops of GLAD sample (t=39)

5.3.2 Co/Pd Multilayered Nanorods

Nanorods with stacks of Ta 5nm/Pd 10nm/ [Co 0.3 nm/Pd 1nm]₉/Ta 5nm were used as an example to demonstrate this method [66], where Ta 5nm/Pd 10nm was used as a seed layer to

promote the fcc (111) texture of the Co/Pd multilayers for high perpendicular anisotropy [99]. The multilayers were capped with a top layer of Ta for protection against oxidation.

The GLAD deposition forms distinct nanorods, as indicated by the side, top and cross sectional SEM views of Figure 5.5 a-c, respectively. These are compared with the corresponding views of the normally deposited films in Figures 5.5 d-f. The diameter of the nanorods was measured from top-view SEM images (Figure 5.5) and estimated at about $12 \text{ nm} \pm 2 \text{ nm}$ as indicated by Figure 5.5 (g). The average distance between the nanorods was about 2 nm. The height estimated from Figure 5.5 (c) was about $31 \text{ nm} \pm 3 \text{ nm}$. In comparison, the Co/Pd multilayers deposited normally indicate dense, flat, granular films, as shown in Figure 5.5 (d)-(f). The normally deposited film thickness was estimated at 26 nm. The void percentage was estimated to be about 20% by assuming that the nanorods were uniform cylinders separated by 2 nm.

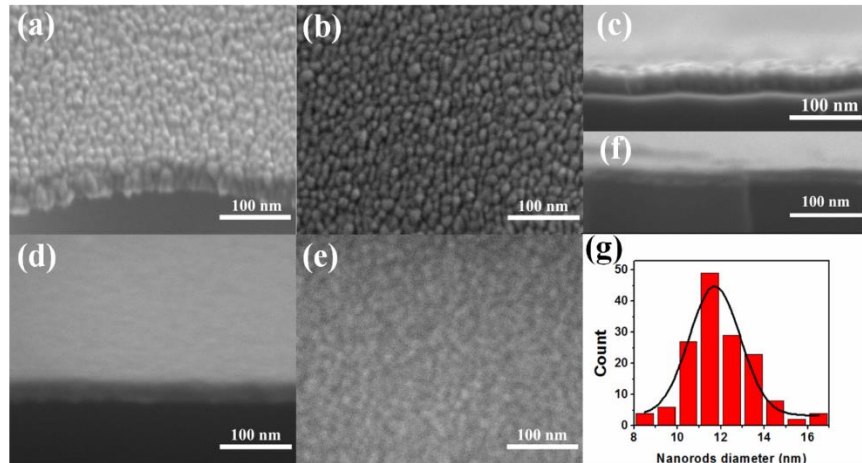


Figure 5. 5 SEM images of (a) and (d) side, (b) and (e) top, (c) and (f) cross sectional views of GLAD and normally deposited Co/Pd multilayered samples, respectively; (g) nanorod diameter distribution from Figure 5.5 b.

Nanorod formation by GLAD can be explained by an atomic self-shadowing effect [53]. Initially, the sputtered atoms condense onto the substrate and form separate nuclei. Since the substrate is at a glancing or grazing incidence to the incoming atom flux, these initial nuclei create a shadow around themselves, blocking the deposition of subsequently arriving atoms. Growth in

the self-shadowed area is suppressed because the initial nuclei capture atom flux which would have otherwise deposited as adjacent nuclei, eventually coalescing into a film [64]. The low diffusivity of adatoms at the ambient deposition temperature also contributes to this effect [53]. The initial nuclei thus grow into nanorods, leaving voids between them.

Surface-topography measurements were performed using tapping mode AFM. Since the size of the AFM tip radius is about 30nm, which is much larger than the spacing between the nanorods (~ 2 nm) or the nanorods themselves (~ 12 nm), the roughness may underestimate the height difference between the nanorods [87,116]. However, it is still useful to compare GLAD and normally deposited samples by AFM, as in Figure 5.6. Although the root-mean-square (rms) roughness for the GLAD sample was estimated at 0.9nm as compared to 0.2 nm for the normally deposited film, the GLAD sample surface roughness is still low, as seen from the side view SEM of the nanorods. This makes it a very promising potential approach for advanced nanopatterned media.

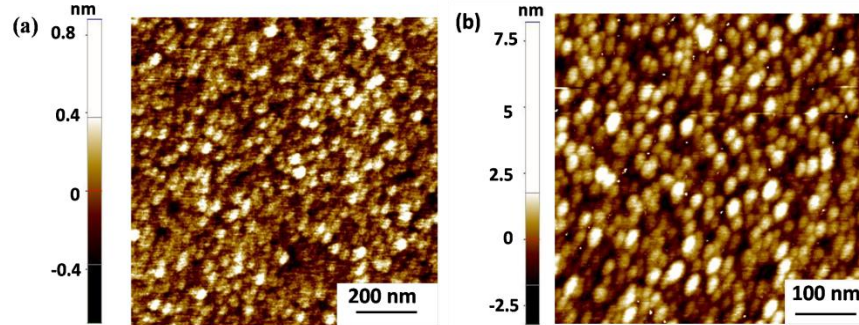


Figure 5. 6 AFM images of (a) normally deposited and (b) GLAD Co/Pd multilayered samples

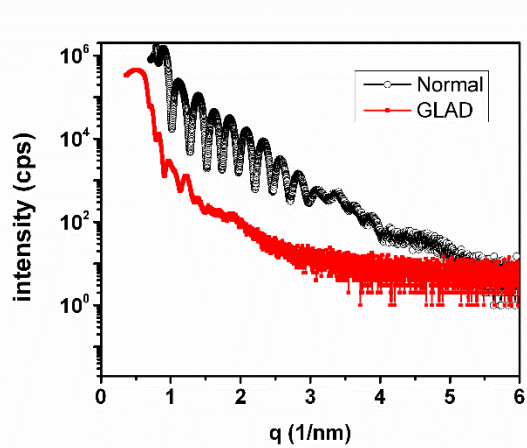


Figure 5.7 XRR spectra for normally deposited (○) and GLAD (■) Co/Pd multilayered samples

Figure 5.7 shows comparative XRR spectra for normally deposited and GLAD samples. The regular interference fringes for the normally deposited sample indicates sharp, abrupt interfaces. The irregular fringes seen for the nanorods may be representative of the surface roughness or height difference of the nanorods, and perhaps intermixing of the material layers [29]. From the X-ray diffraction pattern, shown in Figure 5.8, a single strong peak at about 41° was observed for the normally-deposited film, which confirmed the growth of fcc (111) Co/Pd multilayers [117]. For the GLAD sample, no such peak was seen. We speculate that the nanorods may have a mixture of grain orientations that will be further explored by pole figure analysis.

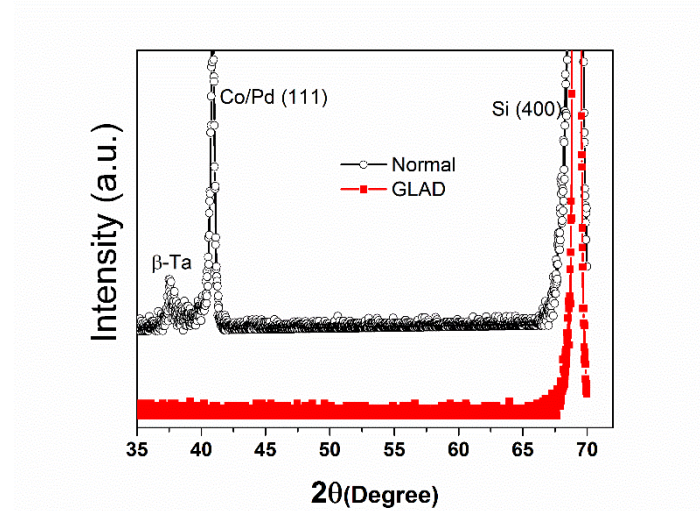


Figure 5. X-ray θ - 2θ scan for normally deposited (\circ) and GLAD (\blacksquare) Co/Pd multilayered samples

The magnetic properties of the Co/Pd multilayers were examined by alternating gradient magnetometry (AGM). Figure 5.9 shows the hysteresis loops of Co/Pd GLAD and normally deposited samples. As is expected, the out-of-plane loops are very square, clearly showing a strong perpendicular anisotropy. Given the effective magnetization of about 312 emu/cm^3 did not change between GLAD and normally deposited samples, the void density for the GLAD film was estimated to be 18% by comparing the magnetic moment from AGM measurements of the two samples divided by the effective volume.

For the normally deposited continuous film, the coercivity is about 1.3 kOe, whereas for the GLAD sample, the coercivity is as high as 2.9 kOe. In the continuous flat film, magnetization reversal starts by nucleation first, followed by domain wall propagation along the lowest energy path due to strong exchange coupling between the grains [86,118]. In contrast, for the GLAD sample we believe that the nanorods decrease exchange coupling and therefore show higher coercive fields. More detailed analysis of the magnetization reversal process will be addressed in the future.

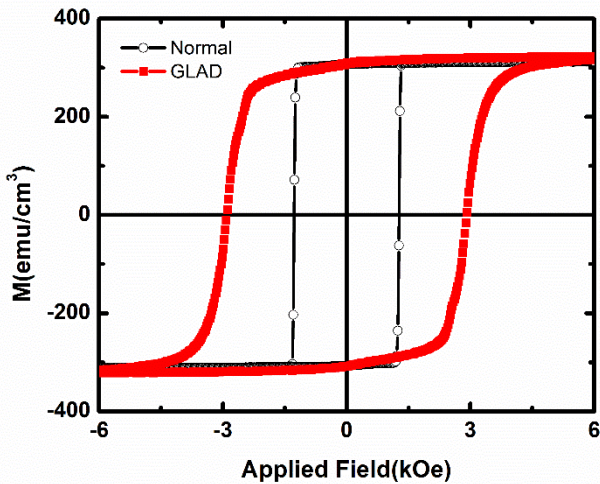


Figure 5. 9 Out-of-plane hysteresis loops for normally deposited (\circ) and GLAD (\blacksquare) Co/Pd multilayered samples measured by AGM.

So far the GLAD sample of Co/Pd multilayer discussed above was only one of several samples fabricated by this method. Similar to flat films discussed in Chapter 3, the effects of the thickness ratio, thickness of each layer and bilayer numbers on the magnetic properties were studied.

For out-of-plane M-H loops of the Co/Pd with 9 BLs shown in Figure 5.10 (a), it can be seen that the sample with a thickness ratio of 0.3/1.0 nm had the highest coercivity of 2.9 kOe, while samples with thickness ratios of 0.17/0.17 nm and 0.5/0.5 nm had very small H_c and showed hard-axis features, which was in agreement with the results of flat films. A possible reason may be that the Co thickness was so small that the Co atoms distributed in Pd matrix.

For BLs number set at 20 and thickness ratio of Co/Pd set at 1.0/3.3 nm, the Co thickness was changed from 0.1 nm to 0.3 nm. From the M-H loops shown in Figure 5.10 b and d, it was observed that all the M-H loops are square, indicating strong perpendicular anisotropy. H_c increased from 0.2kOe to 1.8kOe as the thickness of Co layer increased from 0.1nm to 0.2nm; however, further increasing Co thickness did not change H_c too much, from 1.8 kOe to 2.0 kOe.

For those samples with 40 BLs, Co/Pd with thickness of 0.1nm/0.33nm showed PMA, while Co/Pd with thickness of 0.17nm/0.17nm showed in-plane magnetization, (out-of-plane loop was hard axis), which may be a result of the change in thickness ratio.

For Co/Pd with the same thickness ratio of 0.3nm/1.0nm, samples with 9 BLs showed higher coercivity than that of 20 BLs. However, for Co/Pd with the same thickness ratio of 0.1 nm/0.33nm, the sample with 40 BLs showed H_c of 0.8 kOe, much higher than 0.2 kOe for 20BLs. It may be attributed to the change of total thickness and inter-mixing of atoms.

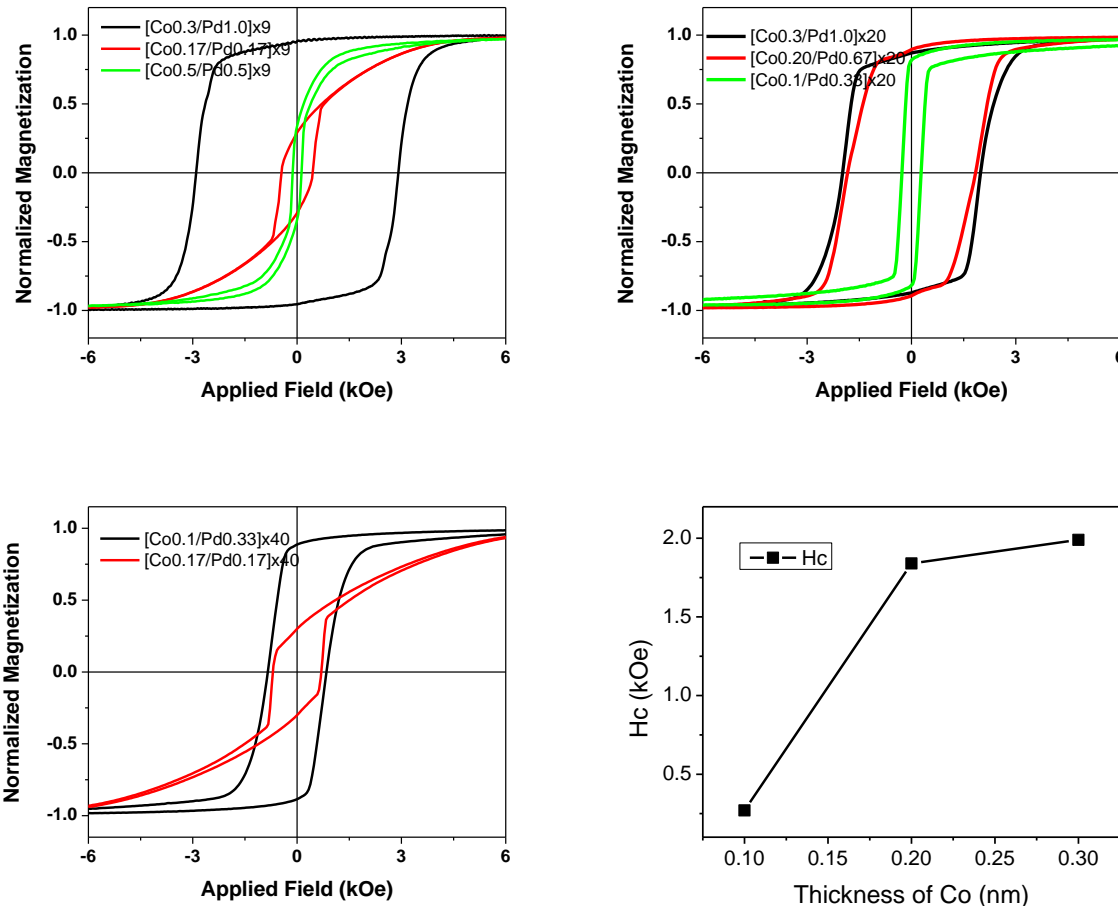


Figure 5. 10 Out of plane M-H loops of GLAD Co/Pd multilayered films with various thickness and bilayer number as indicated in the plot. Figure 5.10 d showed H_c extracted from b as a function of Co thickness.

5.3.3 Co/Pd Nanocolumn on Nanospheres

We fabricated Co/Pd nanorods by combining block co-polymer (BCP) templating technique as described in the previous chapter, with GLAD. Co/Pd samples with a stack of Ta5/Pd5/[Co0.3/Pd1.0]₂₀/Ta5 (thickness in nm) were deposited on silicon substrates and PFS nanospheres, respectively. PFS nanospheres exposed by plasma ashing acted as seeds/template, which enhanced the shadowing effect.

Figure 5.11 show typical side-view and plan-view SEM images of the film deposited on PFS nanospheres and Si substrate directly. It is clearly seen that the nanorods are tilted to a preferential direction, incident flux direction, which is from top right for Figure 5.11 a. As seen in Figure 5.11 a and b, the diameter of nanorods were about 40 nm, which was larger than 20 nm of the diameter of seeds. The materials were mostly deposited on the PFS nanospheres, while the deposition of materials between the nanorods were still visible, which may be attributed to non-directional incoming flux. With a close examination of inset pictures in Figure 5.11 a and b, it was found that the surfaces were rough with projections, which was attributed to shadowing growth instability which caused the formation of nanorods. [119]. It is believed that small surface irregularities were enhanced during the growth, as the irregularities increased capture rate of the incoming flux, thus increasing the local growth rate to yield projections. In addition, the non-directional incoming flux may also contribute the development of these projections.

In comparison, nanorods grown on the silicon substrate showed uniform and narrow size distribution, as shown in Figure 5.11 c and d. The diameter of nanorods was about 14nm, much smaller than those with PFS nanosphere seeds. It appears reasonable that, for the substrate, the incoming atoms nucleated and grew, while for the patterned substrates, nanosphere seeds acted as nuclei, with the incoming material atoms continuing to grow on the seeds. Therefore the nanorods

on unpatterned substrates showed smaller size while patterned substrates yielded larger size nanorods. [119]

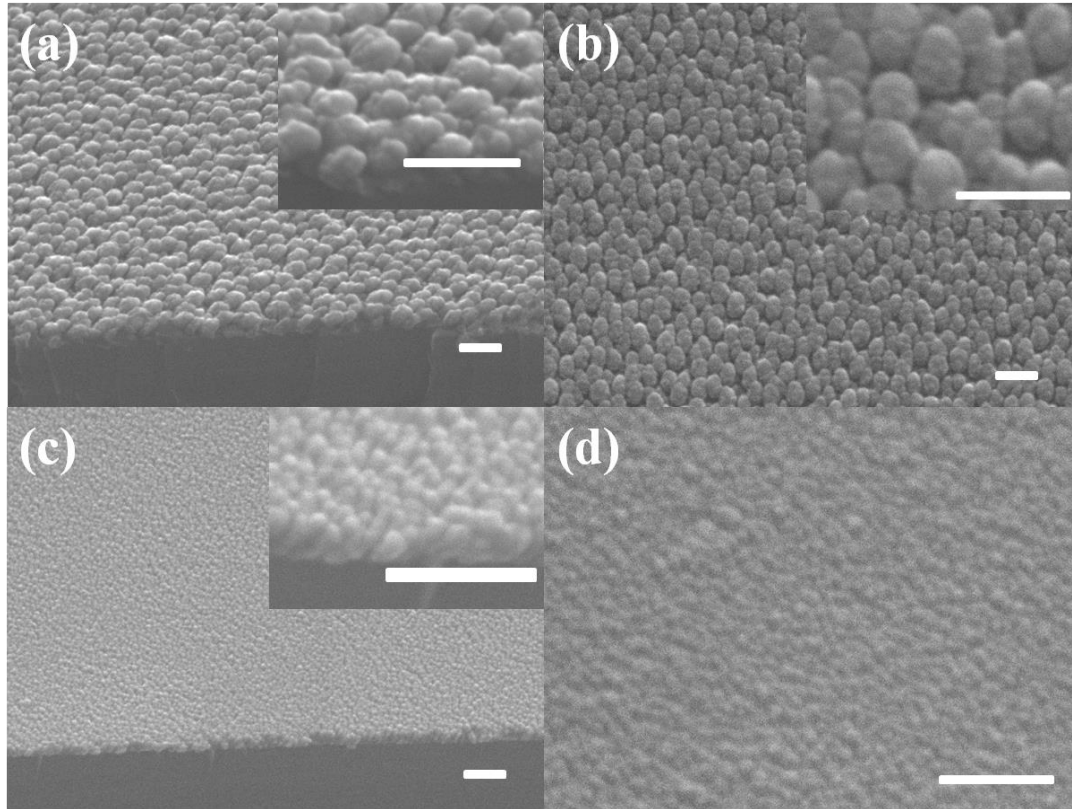


Figure 5. 11 SEM images of nano-columns grown on PFS nanospheres and bare silicon. (a) Cross-sectional view and (b) plan-view on PFS nanospheres, (c) cross-sectional view and (d) plan-view SEM images on silicon. The inset pictures are corresponding pictures at high magnification. All the scale bars are in 100 nm.

Magnetic properties were also examined by M-H loops which were measured by AGM. Figure 5.12 showed M-H loops of Co/Pd GLAD samples with stacks of Ta5/Pd5/[Co0.3/Pd1.0]₂₀/Ta5 (thickness in nm) deposited on the silicon substrates and PFS nanospheres as well as a normally deposited sample on silicon for comparison. It was observed that the GLAD sample on a pre-patterned substrate showed high coercivity of 2.0 kOe but a canted shape of loop with low squareness, while the GLAD sample on the silicon showed coercivity of 1.6 kOe and high squareness. The difference of the two GLAD samples may result from the

difference of structures due to different growth processes. However, both of them have higher coercivities than that of normally deposited sample. As discussed above, the normally deposited film was a continuous film which experienced nucleation and domain wall motion while GLAD samples switch by a different mechanism, which was because of weak exchange coupling resulting from separate nanocolumns.

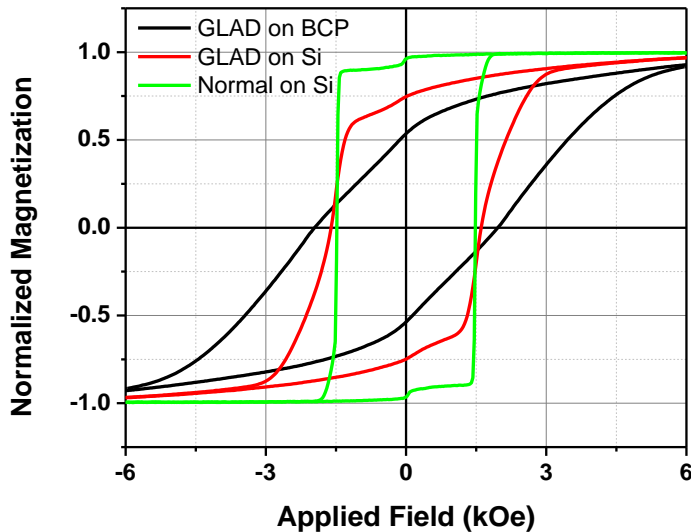


Figure 5. 12 M-H loops of Co/Pd GLAD samples with stack of Ta5/Pd5/[Co0.3/Pd1.0]_{x20}/Ta5 (thickness in nm) deposited on the silicon substrates and PFS nanospheres, respectively. For comparison, the M-H loop of normally deposited sample with same stack was also plotted.

5.3.4 FeB/Pt Multilayered Nanorods and FeBPt Composite Nanorods

FeB/Pt multilayered and FeBPt composite nanorods were deposited by GLAD and normal sputtering, with stacks and conditions shown in the Table 5.2. Annealing at 550°C for 6,15 and 30 mins was carried out in the Shamrock using rapid thermal annealing (RTA) while annealing at various temperatures for 1 hr was carried out in the vacuum annealer. It should be noted that all the samples were prepared by magnetron sputtering in the Shamrock. For multilayered samples,

FeB and Pt targets were turned on alternately while for co-sputtered samples, FeB and Pt targets were turned on simultaneously.

Table 5. 2 FeB/Pt sample details and annealing conditions

Sample ID	Film Type	Stacks	Annealing
GLAD-A	MLs, GLAD	FeB4/Pt3.3/[FeB0.4/Pt0.33] ₁₅ /Ta1.7	Rapid Thermal Annealing & Furnace Annealing
GLAD-B	Co-sputter, GLAD	FeB4/Pt3.3/FeBPt 11 /Ta1.7	
Normal-A	MLs, Normal	FeB4/Pt3.3/[FeB0.4/Pt0.33] ₁₅ /Ta1.7	
Normal-B	Co-sputter, Normal	FeB4/Pt3.3/FeBPt 11 /Ta1.7	

As shown in Figure 5.13, FeB/Pt multilayered nanorods have been fabricated by GLAD. The diameter of nanorods is about 11 nm with thickness (height) of 20 nm. No significant change was observed when the sample GLAD-A was annealed at 600°C for 1hr. It was also interesting that the co-sputtered GLAD-B showed similar morphologies as those of multilayered GLAD-A sample. It is possible that with similar composition the same thickness sample would show the same growth behavior.

In order to study the magnetic properties of these GLAD samples, the in-plane M-H loops were measured. As shown in Figure 5.14, the coercivities increased from a few Oe to hundred Oe as annealing time was increased from 0 min to 60 min at 550°C for both GLAD-A and GLAD-B, indicating the ordering increased after annealing.[120] Comparing Figure 5.14 a and c, multilayered sample GLAD-A showed higher coercivities than those of co-sputtered GLAD-B. As the annealing temperature increased, Hc increased for both type of samples. However, the M-H loops vs. annealing temperature showed different trends for GLAD-A and GLAD-B. GLAD-B showed higher Hc when annealed at 600°C for 1hr.

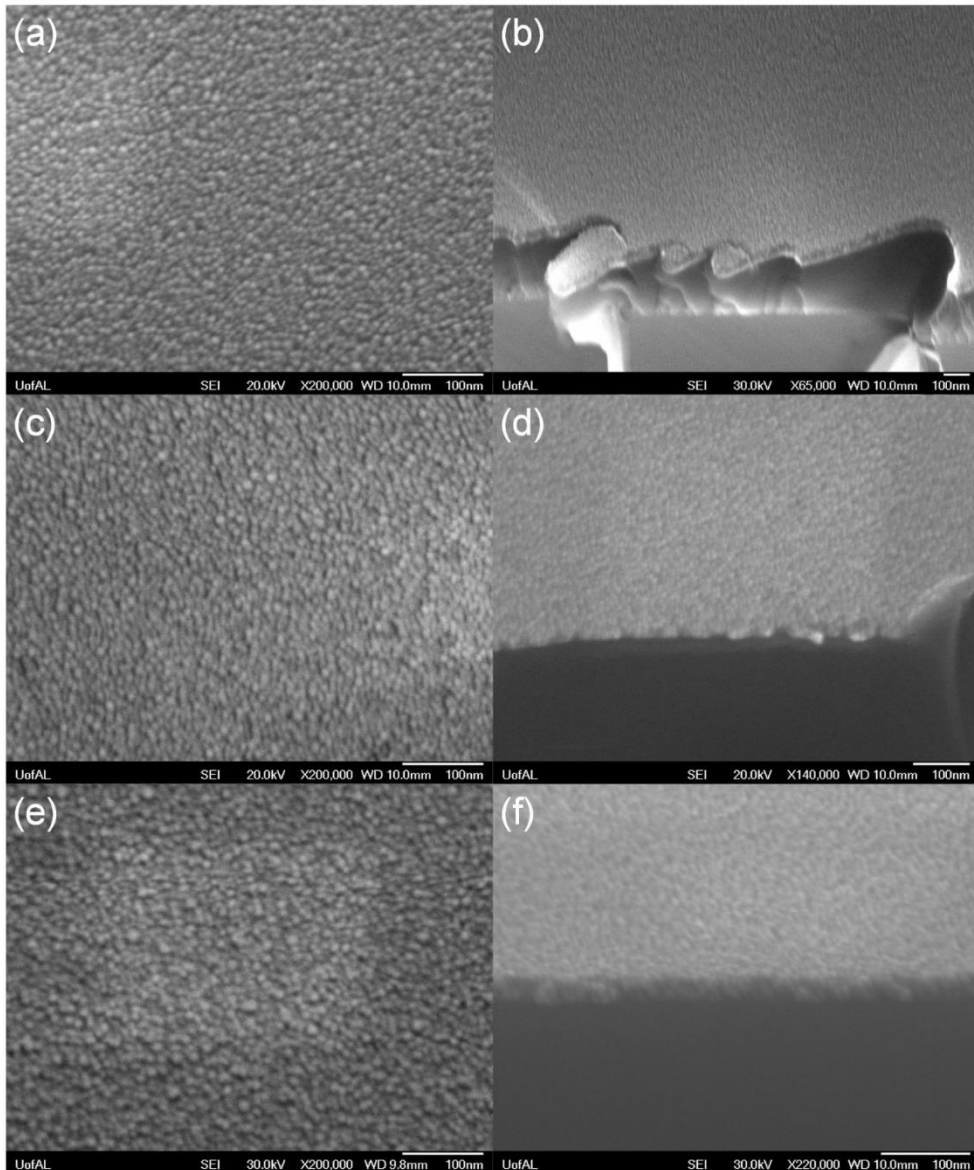


Figure 5. 13 SEM images of GLAD samples. Top-view of (a) GLAD-A as-deposited (b) GLAD-A 600°C1hr annealed and (c) GLAD-B as-deposited. (b)(d)(f) are corresponding tilt-view images.

M-H loops for Normal-A and Normal-B which have the same nominal stacks as GLAD-A and B were also measured for comparison, shown in Figure 5.15. It can be seen that Normal-B showed higher coercivities than that of Normal-A, after annealing at different conditions. It can be explained by better mixing of Fe and Pt as FeB and Pt were co-sputtered for Normal-B and thus had a shorter interdiffusion distance. Normal-B showed high ordering. The details for normally

deposited samples will be discussed in the next chapter. However, GLAD samples were found inferior to these normally deposited samples, from the viewpoint of magnetic properties. The possible reasons may lie in the fact that these GLAD samples were too thin to form separate nanorods and the energy they need to form ordered structure was thus increased. Further study will be conducted to solve these questions.

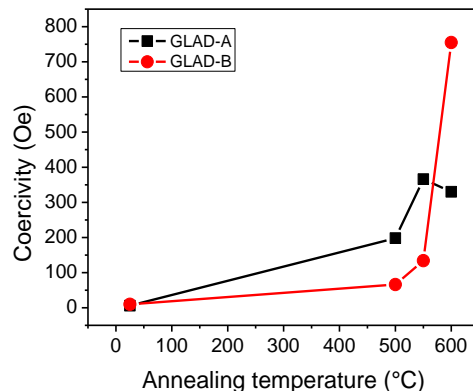
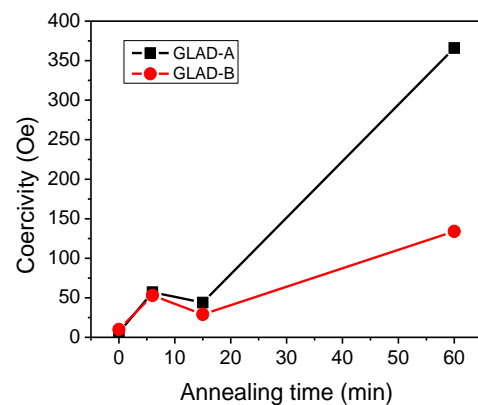
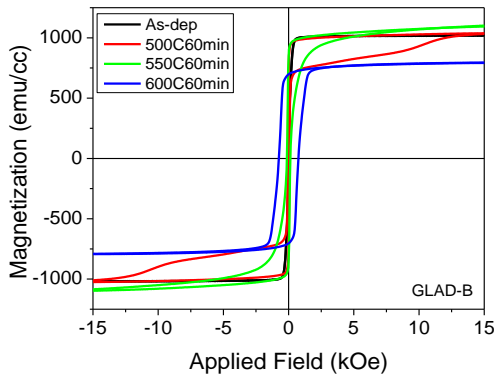
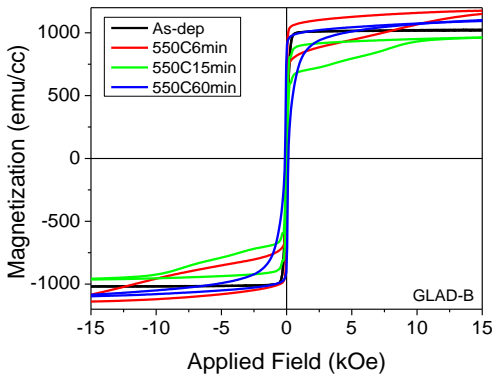
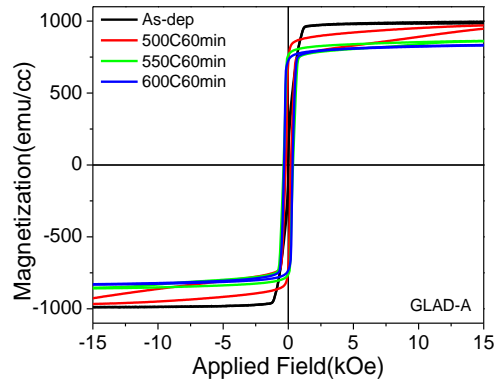
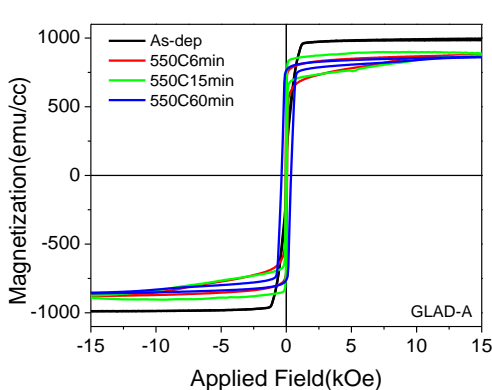


Figure 5. 14 In-plane M-H loops of (a) sample GLAD-A vs. annealing time at 550°C (b) GLAD-A annealed at different temperature (c) GLAD-B annealed at 550°C for different time and (d) GLAD-B annealed at different temperature for 1hr. (e) and (f) are coercivities extracted from (a)-(d) as functions of annealing time and annealing temperature, respectively.

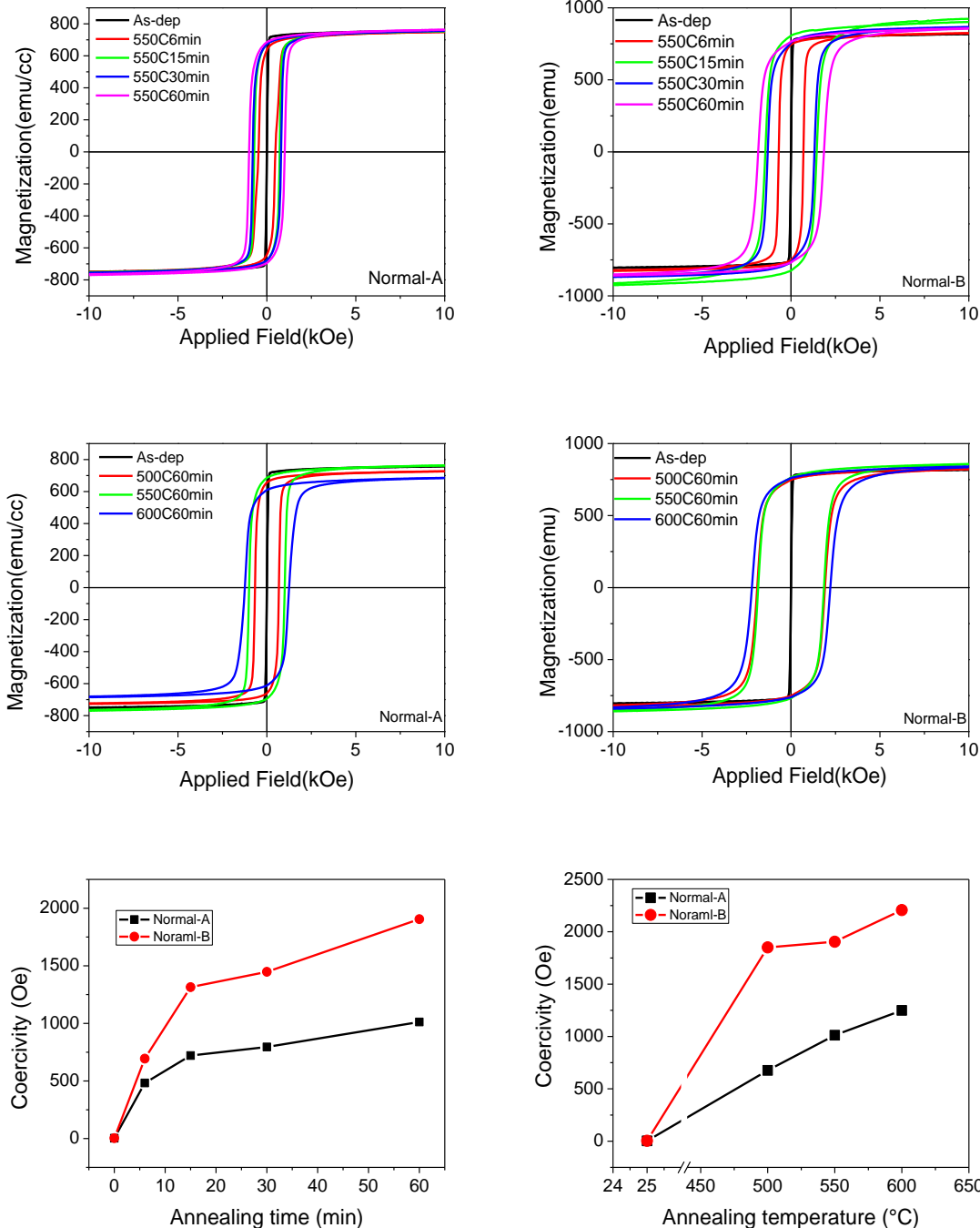


Figure 5. 15 In-plane M-H loops of (a) sample Normal-A vs. annealing time at 550°C (b) Normal-A annealed at different temperature (c) Normal-B annealed at 550°C for different time and (d)

Normal-B annealed at different temperature for 1hr. (e) and (f) are coercivities extracted from (a)-(d) as functions of annealing time and annealing temperature, respectively.

5.3.5 Co Nanorods

What has been discussed so far was GLAD by planetary deposition. Additionally, a stationary deposition of Co was also carried out. The substrate was projecting over the cobalt target and the distance was about 90mm. The deposition rate of Co was about 0.42nm/s, much higher than 0.032nm/s of planetary deposition because the deposition was continuous. As shown in Figure 5.16, it can be seen clearly that the Co nanocolumnar structures have been fabricated. The angle was about 20 degree off from the normal of the substrate which was similar to that of planetary GLAD sample. However, the diameter was about 100nm, much larger than ~18 nm planetary GLAD sample, which may be attributed to the much higher deposition rate. It also may demonstrate that the size of nanorods will increase if the nanorods grow long enough.

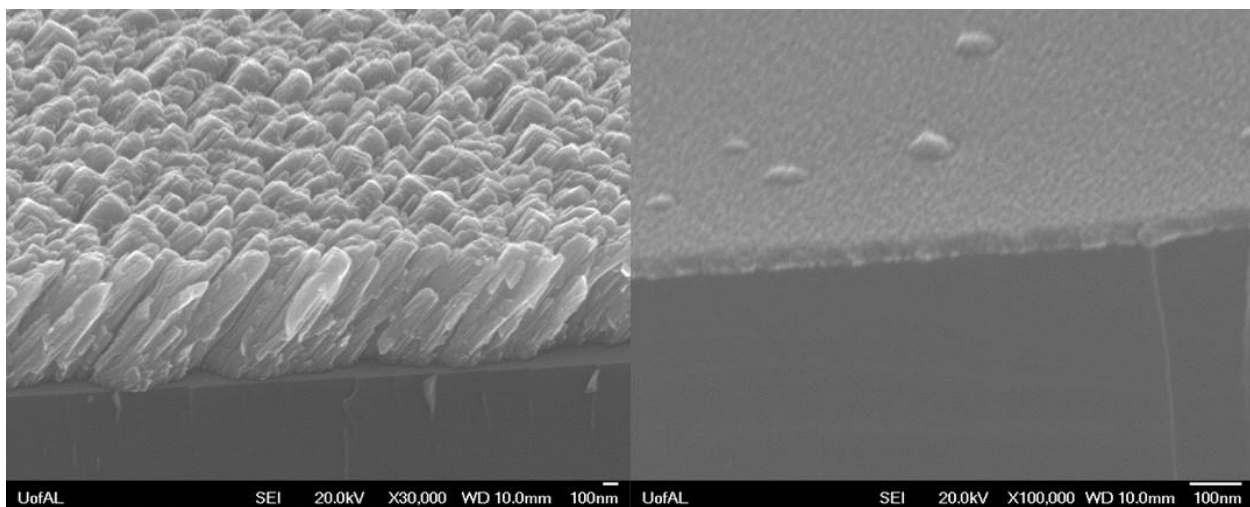


Figure 5. 16 Side-view SEM images of Co sputtered for 40min at 300W (a) stationary deposition and (b) planetary deposition

5.4 Conclusions

Magnetic nanorods of Co/Pd multilayers, CoPt, CoPt-AlN, FeB/Pt and Co have been fabricated by glancing angle deposition in a single-step process.

For CoPt_ALN, Nanorods of CoPt-AlN with diameter of ~16nm were successfully formed for the first time by GLAD. M-H loops of GLAD samples had higher remanence (more perpendicular) than that of flat films, where volume ratio of CoPt : AlN=2 yielded highest coercivity. However, the easy axis of magnetization was in-plane which was not favorable for information storage. Further work includes more structural analysis, simulation, and angle control.

For Co/Pd multilayered nanorods on silicon substrate, the dimensions for a specific stack of [Co0.3/Pd1.0] \times 9 were found to be about 31 nm \pm 3 nm in height, about 12 nm \pm 2 nm in diameter, with about 2 nm spacing. The void density was estimated to be about 20% from SEM and magnetometry. The coercivity increased from 1.3 kOe for normally deposited films to 2.9 kOe for the GLAD sample, a 123% increase. The effect of thickness ratio and bilayer numbers on the magnetic properties were also investigated. Future work will explore other multilayered materials, for instance, Fe/Pt or Co/Pt, and focus on the analysis of magnetization reversal.

For Co/Pd multilayered nanorods on PFS nanospheres, nanorods with a larger size of 40nm in diameter were fabricated. The rough projections on the nanorods were attributed to the shadowing effect and surface irregularities. It will be helpful to extend the study systematically on different size seeds.

For FeB/Pt multilayered and FeBPt composite nanorods, nanorods with diameter of 11 nm were fabricated. However, these samples did not show higher coercivities than their corresponding normally deposited samples.

For Co nanorods by stationary and planetary GLAD, it was found that the diameter of stationary GLAD sample was much larger than that of planetary GLAD sample under the same power and deposition time. The difference resulted from the huge difference of deposition rate. It also demonstrates that the size of nanorods will increase if the nanorods grow long enough.

Chapter 6 Microstructure Evolution and Magnetic Properties of Fe(B)/Pt Multilayered and Fe(B)Pt Thin Film

6.1 Introduction

Granular L₁₀ FePt is a leading candidate for next generation magnetic recording, in particular, heat assisted magnetic recording (HAMR). This is primarily because of its extremely high magnetocrystalline energy constant ($\sim 7.0 \times 10^7$ erg/cm³), which can maintain thermal stability even with a grain size reduced to 3nm. [15, 16]. Post-deposition annealing or substrate heating at high temperature is required to form the L₁₀ phase. Annealing [Fe/Pt]_n multilayered films is a promising approach to reduce the ordering temperature as it can enhance the interdiffusion of Fe and Pt atoms between thin layers.[40,121]. On the other hand, addition of a third element can also lower the temperature because of enhanced diffusivity of atoms. [17-19,122].

In this chapter [149], we used two different planetary sputtering techniques to deposit FeB/Pt multilayered films with the same total thickness but different bilayer thicknesses. The dependence of microstructure evolution and magnetic properties on annealing time and temperature and film thickness was studied. In order to study the exchange coupling effect, FeB layers were deposited on top of the annealed, high coercivity FeB/Pt multilayers. Fe/Pt multilayered films with different thickness and configurations were also studied.

6.2 Experiments

All depositions were carried out on thermally oxidized silicon substrates in a seven-target SFI Shamrock planetary sputtering system, using dc magnetron sputtering for all the layers. An infrared lamp array was placed in one of the target positions. The base pressure prior to deposition was 5×10^{-8} Torr. Depositions were carried out utilizing high purity three-inch diameter Fe₈₀B₂₀,

Fe, Pt and Ta targets, sputtered at power levels of 103-311 W, corresponding to deposition rates ranging from 0.02-0.083 nm/s. The sputtering Ar pressure was maintained at 2 mTorr. All the samples, with the details of the processing conditions, are listed in Table 6.1 and will be discussed later. The samples were annealed at temperatures ranging from 300°C to 650°C for various times in a vacuum annealer, at a pressure of about 5×10^{-5} torr. Some of the samples were also annealed for times ranging from 6 minutes to 30 minutes at 550°C using the lamp annealer in the Shamrock. The compositions of the films were confirmed by energy dispersive x-ray analysis (EDX). The crystal structure of the films was analyzed by a Philips X’Pert X-ray diffractometer (XRD) with CuK α radiation. The magnetic properties were measured at room temperature by a Princeton PMC Micromag 2000 alternating gradient force magnetometer (AGM) with maximum applied field of 18 kOe. The microstructure- of the films were characterized by a FEI Tecnai F-20 transmission electron microscope (TEM). Samples for the plan-view TEM were prepared by a standard method, including polishing, dimpling and ion-milling while cross-sectional samples were prepared by focused ion beam (FIB, FEI Quanta 3D Dual Beam).

First, two different multilayered samples with the same thickness were deposited by two different planetary sputtering techniques. For sample series A, consisting of the following stack: FeB12/Pt10/[FeB1.2/Pt1]_{x15}/Ta5 nm, the FeB and Pt layers were deposited sequentially, resulting in coarse multilayers. In the case of sample series B, the targets were simultaneously sputtered (co-sputtered), resulting in an order of magnitude reduction in individual layer thicknesses, since the substrate rotated at 22 rpm between targets. Therefore, we denote the film stack in sample B as FeB12/Pt10/[FeB0.11/Pt0.09]_{11x15}/Ta5 nm. Sample series A will be referred to as the coarse multilayered samples, while series B will be referred to as the fine multilayered samples or composite films.

Table 6. 1 Sample list with details of stacks, processing conditions and analysis

Sample Series	Stacks	Processing Conditions	Analysis
Series A	FeB12/Pt10/[FeB1.2/Pt1] ₁₅ /Ta5	Post-dep furnace annealed @300-650°C, 1hr Post-dep lamp annealed @550°C, 6-30min	Microstructural evolution and magnetic properties vs. annealing time / temperature, film thickness and sputtering conditions
Series B	FeB12/Pt10/[FeB0.11/Pt0.09] _{11x15} /Ta5		
Series C	FeB4/Pt3/[FeB0.4/Pt0.3] ₁₅ /Ta5		
Series D	FeB4/Pt3/[FeB0.036/Pt0.027] _{11x15} /Ta5		
Series E	FeB 9/Pt 10/[FeB0.9/Pt1.0] ₁₅ /Ta5	Post-dep furnace annealed @600°C, 1hr. ion milled Ta, sputtered 0-40nm FeB layers, annealed @400°C, 30min	Exchange coupling effect, annealing effect
Series F	[Fe0.47/Pt0.4] ₁₂	Post-dep lamp annealed @550°C, 20s-12min	Magnetic properties vs. composition and bilayer thickness
Series G	[Fe0.043/Pt0.036] _{11x12}		
Series H	Fe3/Pt3/ [Fe0.47/Pt0.4] ₁₂	Post-dep lamp annealed @550°C, 5 min	Magnetic properties vs. bilayer thickness
Series I	[Fe0.5/Pt0.5] ₁₂		
Series J	[Fe1/Pt1] ₆		
Series K	Fe3/Pt3/[Fe0.5/Pt0.5] ₆		

For the dependence of magnetic properties on film thickness, sample series C and D with stacks of FeB4/Pt3/[FeB0.4/Pt0.3]_{x15}/Ta5 and FeB4/Pt3/[FeB0.036/Pt0.027]_{11x15}/Ta5, respectively, were prepared.

Another multilayered film series with a stack of FeB 9/Pt 10/[FeB0.9/Pt1.0]₁₅/Ta5 nm (referred to as sample series E) was deposited, with the same procedure as that of sample series A. These samples were annealed at 600°C for 1 hour. The cap layers of Ta were removed using ion-milling immediately preceding the deposition of varying thicknesses of FeB on top of the stack. The samples were then annealed at 400°C for 30 minutes to study the change of magnetic properties.

Fe/Pt multilayered films with different thicknesses and bilayer configurations were also sputtered onto thermally oxidized silicon from elemental targets of Fe and Pt via similar techniques. The stacks are as follows: [Fe0.47/Pt0.4]₁₂, [Fe0.043/Pt0.036]_{11x12}, Fe3/Pt3/[Fe0.47/Pt0.4]₁₂, [Fe0.5/Pt0.5]₁₂, [Fe1/Pt1]₆, Fe3/Pt3/[Fe0.5/Pt0.5]₆, (thickness in nm), referred to as samples series F- K, respectively. Similarly to Samples A and B, the samples were annealed by RTA in the Shamrock.

6.3 Results and Discussion

6.3.1 Sequential and Co-sputtered FeB/Pt Multilayered Sample

6.3.1.1 Structural and Magnetic Properties of Sample Series A and B FeB/Pt Multilayered Films Annealed at 550 °C vs. Annealing Time.

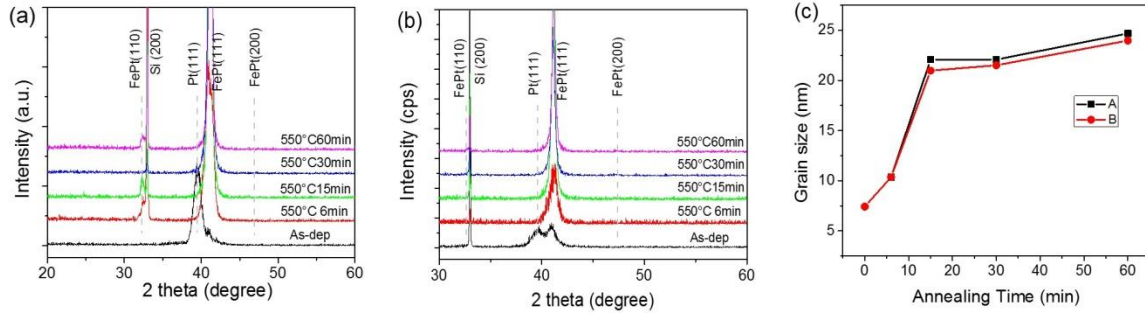


Figure 6.1 XRD patterns of (a) sample series A and (b) sample series B annealed at 550°C for various time (c) Grain size calculated by Sherrer equation as functions of annealing time for samples series A and B.

Figure 6.1 shows XRD patterns of sample series A and B annealed at 550°C for various times. From Figure 1 (a), it may be seen that the as-deposited sample A showed a strong Pt (111) peak, as it had a thick Pt seed layer, and on the right shoulder of Pt (111) was a weak FePt (111) peak, indicating the existence of FePt. Annealing at 550°C for 6 minutes, the FePt (111) peak shifted slightly to a higher angle. The FePt (110) peak was also observed. No obvious change was observed with further increasing the annealing time. Figure 6.1 (b) shows the XRD patterns of sample series B annealed under the same conditions. The as-deposited B showed both Pt (111) and FePt (111) peaks with similar intensities, which is very different from what was observed for sample A with the coarse multilayers. The annealing also intensified the FePt (111) peaks. The grain sizes were calculated by Sherrer's equation $D = \frac{B\lambda}{\beta \cos \theta}$, where B is a constant, 0.89, λ is the wavelength of the X-rays, β is full width at half maximum (FWHM) measured from the XRD peaks, and θ is the incident angle of the X-rays.[78,122]. As seen in Figure 6.1(c), the grain size

increased from about 6 nm to 22 nm when increasing the annealing time from 6 min. to 15 min. This may be attributed to the faster interdiffusion of Fe and Pt to form the FePt phase, in agreement with Zotov et al.'s report that, above 300°C, fast long-range diffusion occurs and forms FePt with strong [111] texture[123]. Further annealing increases the grain size slightly. The annealing time of 1 hr. should be more than enough for the diffusion of atoms to form an ordered structure.

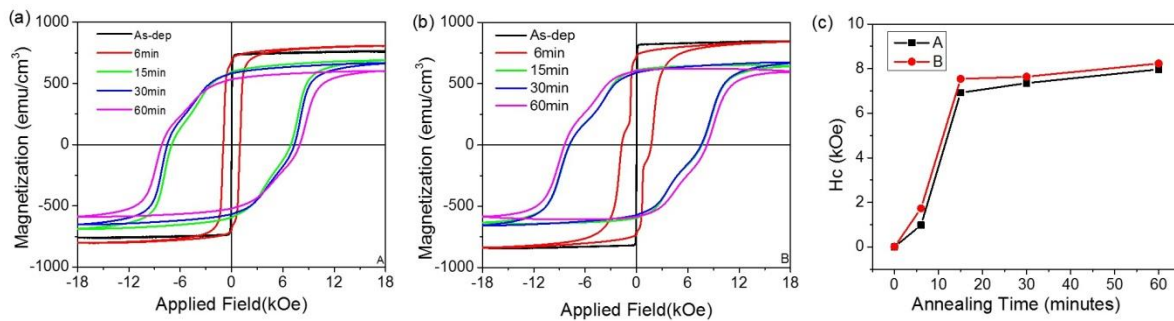


Figure 6. 2 In-plane magnetization curves of (a) sample series A and (b) sample series B annealed at 550°C for 0, 6,15,30 min and 1hr, respectively. (c) The dependence of H_c on annealing time at 550°C.

The in-plane M-H loops of A and B annealed at 550°C for various times are shown in Figures 6.2 (a) and (b) respectively. It can be seen that the as-deposited films were magnetically soft because the films were FeB/Pt multilayers for series A and randomly oriented fcc boron-doped FePt nanograins for series B. After annealing at 550°C for 6 min, the coercivity increased due to the formation of FePt. Further annealing increased the coercivities of both samples to about 8 kOe. It was noted that M-H loops showed multi-step switching, which was possibly from the thick FeB/Pt seed layer where it could not completely form the FePt phase, resulting in weak exchange coupling between the FePt-B and its seed layer. It was also observed from Figures 6.2 (a) and (b) that the saturation magnetization decreased with increasing the annealing time. This may result from the fcc to fct structural transition because of the decrease of the mean atomic magnetic moment [124]. Figure 6.2 (c) shows the dependence of H_c on annealing time at 550°C for both

samples. It can be seen that H_c increased with increasing annealing time. An interesting point is that B showed slightly higher coercivities than that of A under the same annealing time at 550°C, which was attributed to better intermixing of Fe and Pt atoms, as B had much finer layering.

6.3.1.2. Structural and Magnetic Properties of Sample Series A and B FeB/Pt Multilayered Films Annealed for one hour vs. Annealing Temperature.

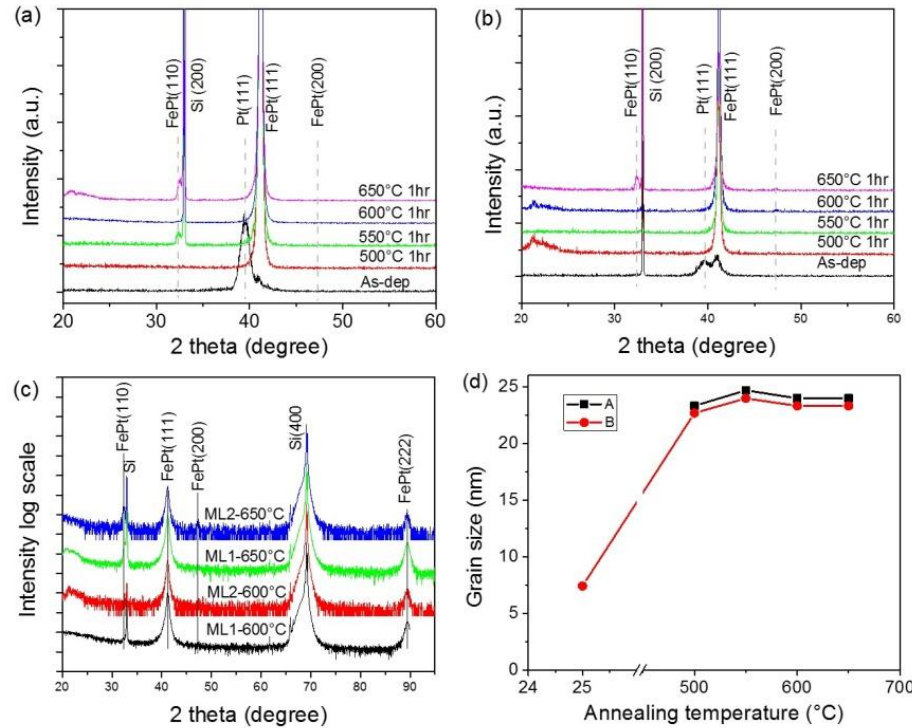


Figure 6.3 XRD patterns of (a) sample series A and (b) sample series B annealed for 1hr for various temperatures, (c) sample A and B annealed at 600°C and 650°C for 1 hr. Grain size calculated by Sherrer equation as functions of annealing temperature for A and B.

Figure 6.3 shows XRD patterns of sample A and B annealed at temperatures ranging from 500°C to 650°C for 1hr. For the sample annealed at 500 °C, the FePt (111) peak was visible while the Pt (111) peak disappeared, indicating intermixing with the Pt seed layer. Increasing the annealing temperature resulted in the intensity of the (110) peak increasing while no significant difference was observed for the FePt (111) peaks. Figure 6.3 (b) shows XRD patterns of sample series B which had a fine atomic layered structure. A careful examination shows that another peak

was observed when they were annealed above 600°C, which can be assigned to FePt (200). In order to compare these two samples, scanning at large angles was performed, as shown in Figure 6.3 (c). Both the films, after annealing at 600°C and 650°C for 1hr, show strong (111) texture [125]. For samples series A and B annealed at different temperatures, as shown in Figure 6.3 (d), the grain size was almost constant in the range of 22 to 25 nm. Higher temperature annealing does not continue to coarsen the grains.

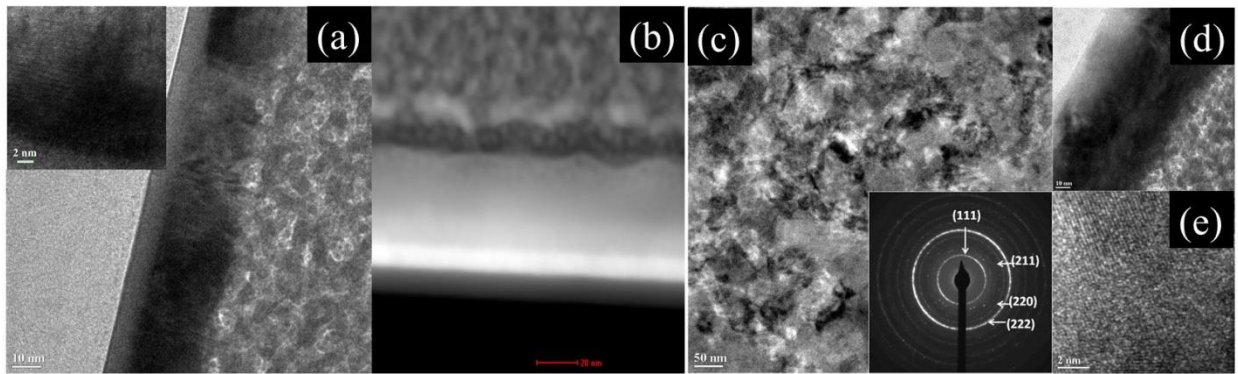


Figure 6. 4 (a) Cross-sectional view of TEM image of as-deposited sample A with the inset showing high resolution. (b) STEM image of same sample in (a) with the scale bar of 20 nm. (c) Plan view and (d) cross-sectional view of TEM image of sample A annealed at 600 °C for 1hr. The inset in (c) shows electron diffraction pattern of the same sample. (e) high resolution TEM (HR-TEM) image from (d) shows fringes.

Figure 6.4 (a) and (b) show the TEM and STEM images of as-deposited multilayered films. It is clear that 12nm FeB and 10 nm Pt layer are shown with strong contrast in the STEM image. The high resolution image in the inset show the alternate layers, confirming the multilayered structure as expected. No clear fringes were observed, as the sample was not annealed, and it may not be crystalline. Figure 6.4 (c) to (e) show the plan view and cross-sectional views of the bright field TEM image of A annealed at 600°C for 1hr. The inset in Figure 6.4 (c) shows the electron diffraction pattern of the same sample, indicating an ordered structure [126-128]. The film shows interconnected network features, as seen in Figure 6.4 (c). The average size of the cluster of grains was larger than 50 nm. The columnar structure was not observed from the cross-sectional image,

possibly because boron atoms diffused to the surface and the grains inter-connected at the high temperature. In Figure 6.4 (e) the high resolution TEM image shows regular lattice fringes, confirming the existence of an ordered structure of FePt as a result of the interdiffusion of Fe and Pt atoms during annealing. [128, 129]

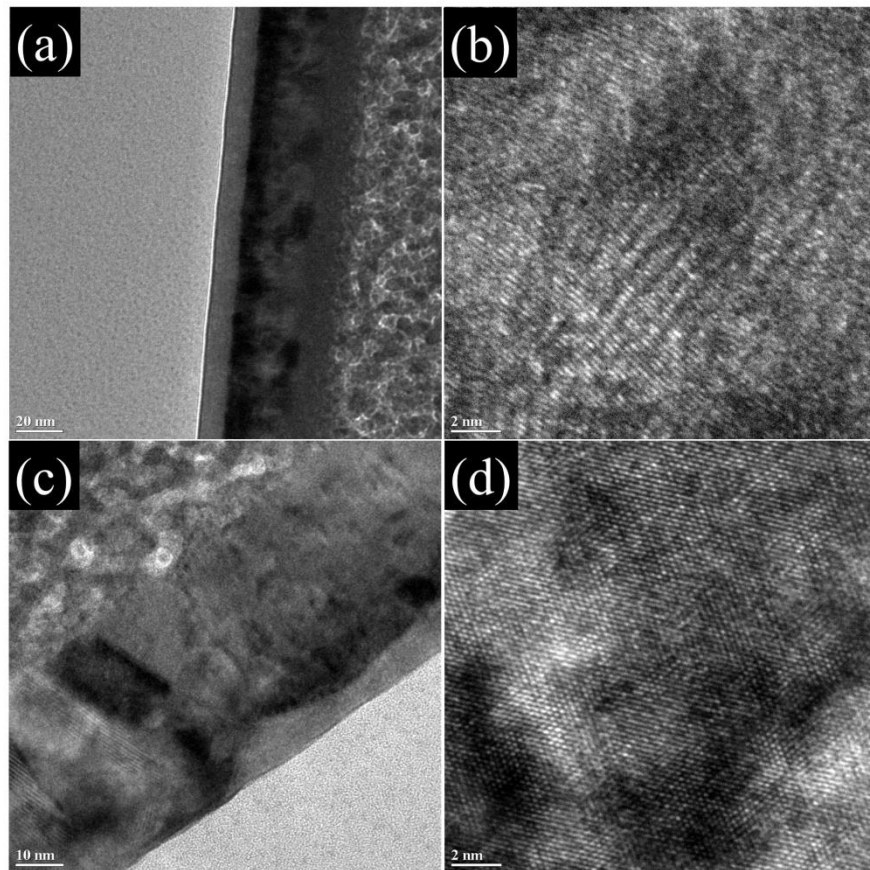


Figure 6. 5 Cross-sectional view of TEM image of sample B (a) as-deposited and (c) annealed at 600°C for 1hr. (b) and (d) shows high resolution TEM image from (a) and (c), respectively.

Figure 6.5 show cross-sectional TEM images of as-deposited and annealed sample series B. For the as-deposited sample shown in Figure 6.5 (a) and (b), the thick seed layers of FeB and Pt were observed. The HRTEM image showed that the alternating layers were much thinner than those of sample series A, confirming the existence of a finely multilayered structure. For the annealed ones, the FeB/Pt intermixed and lattice fringes were observed in HR-TEM image in

Figure 6.5 (b). Similar to Figure 6.5(e) for the sample series A, the orientations of the FePt crystals were random, indicating polycrystalline structure, rather than textured. [129]

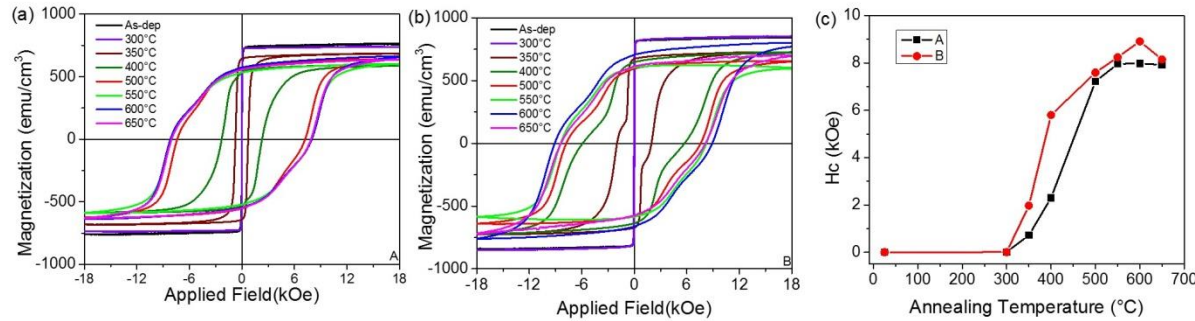


Figure 6.6 In-plane magnetization curves of (a) sample series A and (b) sample series B annealed at different temperatures for 1 hr, respectively. (c) The dependence of H_c on annealing temperatures for 1 hr is shown.

Figure 6.6 shows in-plane M-H loops of sample series A and B annealed at different temperatures. Annealing at 300°C for 1hr was not enough to form the ordered phase for FeB/Pt multilayers, even for sample series B which had very fine multilayers. Increasing the temperature to 350°C, the shape of the loop changed and the coercivity increased, indicating ordering started to occur at this temperature. When the annealing temperature was increased to 400°C, H_c for B increased from about 10 Oe dramatically to 5.9 kOe and H_c for A also increased, due to the transformation of fcc to the fct phase [127,130,131]. Increasing the annealing temperature to 550°C increased H_c , indicating the increase of the ordering phase volume fraction. [120]. However, A and B exhibited different behavior with further increase of the annealing temperature. For A, no obvious change for H_c from 550°C to 650°C was observed, while for B, H_c increased to the highest value of 8.9 kOe at 600°C, and decreased at 650°C. The M-H loops showed multiple switching for all the samples, indicating the existence of a soft phase, either FeB or fcc FeB_xPt_y.[130].

6.3.1.3. Structural and Magnetic Properties of FeB/Pt Multilayered Films Annealed for one hour vs. Film Thickness.

It was reported theoretically and experimentally that the ordering for thinner FePt films requires high annealing temperatures or longer annealing times to reach the same degree of ordering. Otherwise the ordering will be reduced, compared with thick films, when annealing at the same temperature [39,131-134]. The reasons were believed to be the segregation of Pt to the surface and the formation of other more favorable phases of FePt. [135,136]

Sample series C and D have the same composition as sample series A and B but with lower total and bilayer thicknesses. M-H loops for sample series C and D were also measured for comparison, shown in Figure 6.7. It can be seen that D showed higher coercivities than C, after annealing at different conditions. It was also because of better intermixing of Fe and Pt, since FeB and Pt were co-sputtered for sample D and thus had a shorter interdiffusion distance. However, comparing C and D with A and B, respectively, one may conclude that the total film thickness does affect the formation of L₁₀ phase. The plots in Figure 6.7 (e) and (f) clearly showed the difference in magnetic behavior. Under the same annealing conditions, thicker samples always showed higher coercivities than thinner ones. As discussed above, these may result from the diffusion of Pt atoms to the surface and the existence of other phases.

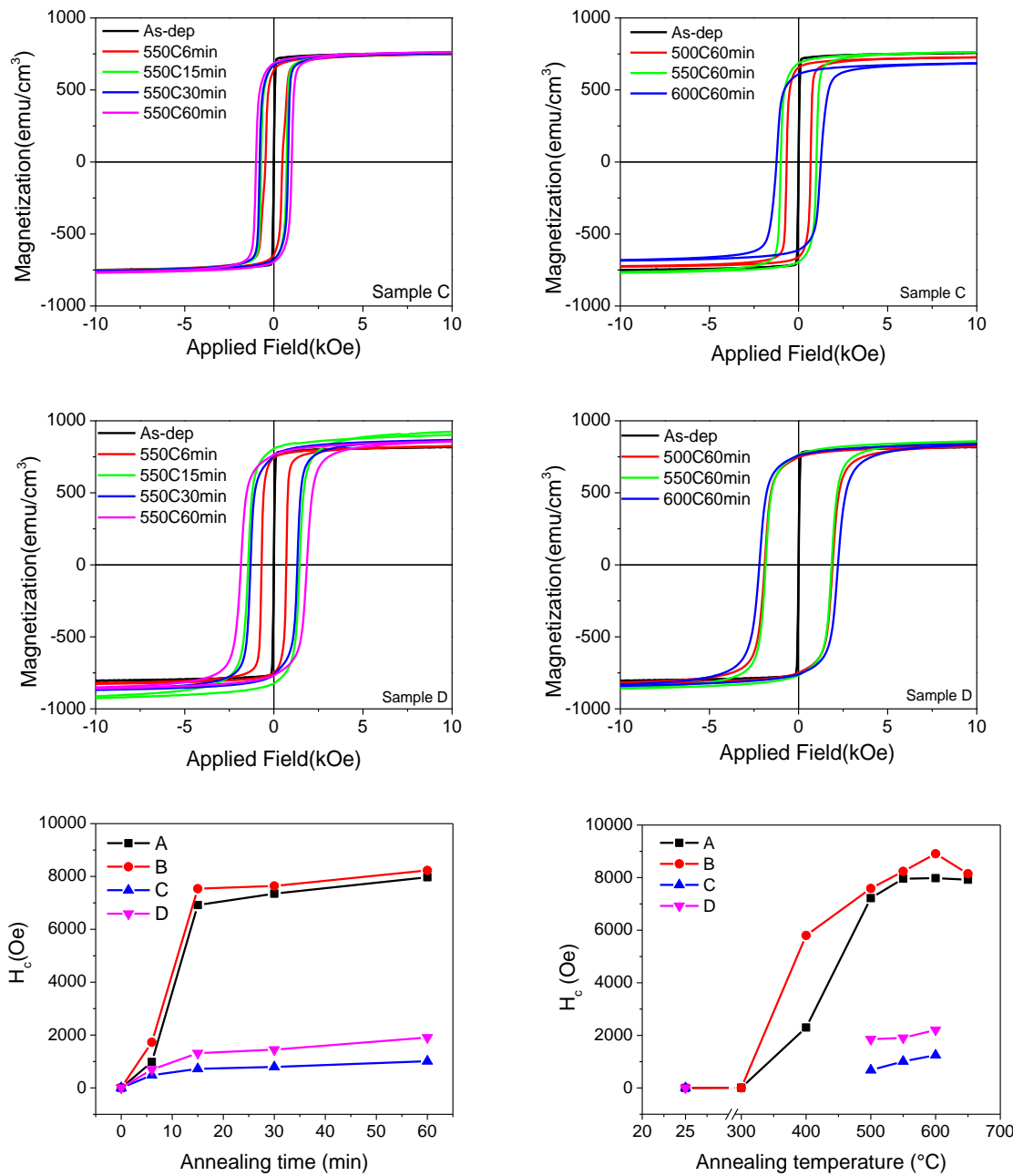


Figure 6.7 In-plane M-H loops of (a) sample series C vs. annealing time at 550°C; (b) sample series C annealed at various temperatures; (c) sample series D annealed at 550°C for various times and (d) sample series D annealed at various temperatures for 1hr; (e) and (f) are coercivities extracted from (a)-(d) and combined with Figure 6.2 (c) and Figure 6.6 (c) as functions of annealing time and annealing temperature, respectively.

6.3.2 Exchange Coupled Composite

As discussed in the above section, we have studied the annealing effect on the properties of FeB/Pt multilayers. Sample series E, with a stack of FeB 9/Pt 10/[FeB0.9/Pt1.0]₁₅/Ta5 nm, which has less Fe compared to sample-series A and B, was annealed at 600 °C for 1hr. Figure 6.8 shows the M-H loop and XRD spectrum of the sample E annealed at 600°C for 1 hr. It shows in-plane coercivity as high as 12 kOe, indicating the formation of L1₀ ordered phase FePt [137]. Meanwhile, the loop showed single-step switching, which means that the film has formed a single phase, or that the seed layer and the FeBPt were exchanged coupled [25, 138]. Similar to annealed samples A and B, the XRD pattern in Figure 6.8 (b) shows the film was (111) orientation-preferred L1₀ structure.

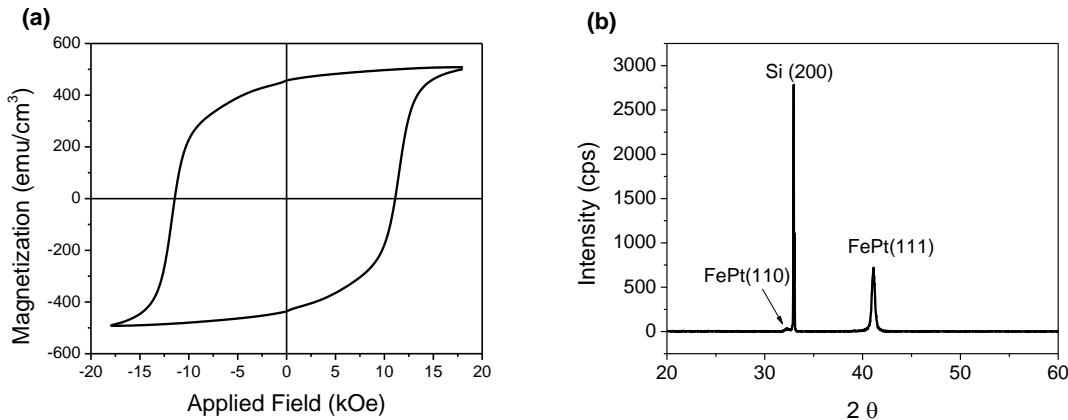


Figure 6. 8 (a) In-plane M-H loop and (b) XRD pattern of sample with stack of FeB 9/Pt 10/[FeB0.9/Pt1.0]₁₅/Ta5 nm annealed at 600 °C for 1hr.

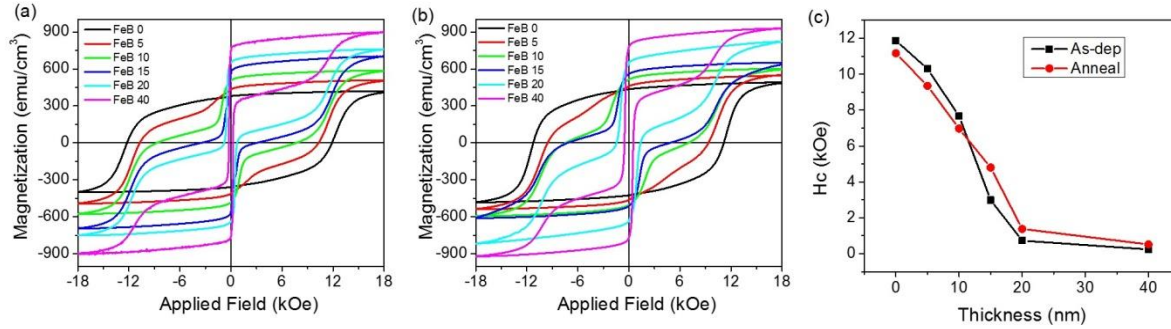


Figure 6.9 In-plane M-H loops of sample E with FeB additions (a) before annealing and (b) annealed at 400°C for 30minutes; (c) coercivity as a function of FeB layer thickness.

In order to study the exchange coupling effect, the Ta cap layer of sample C was removed by ion-milling. Then the sample was capped with an additional FeB layer with thicknesses ranging from 5-40 nm. Figure 6.9 (a) shows M-H loops of sample E with FeB -added layers, before and after annealing at 400°C for 30 min. The FeB Pt, without an additional FeB cap layer, showed high coercivity as seen in Figure 6.9. The coercivities decreased drastically, while the magnetization increased gradually from 418 to 894 emu/cm³, as FeB thickness was increased from 5 to 40 nm. A two-step reversal process was observed for M-H loops of samples with FeB additions larger than 5nm, where a sharp onset of switching was followed by a more gradual approach to saturation, indicating different coercivities of soft FeB and hard phases FePt and weak exchange coupling. [25,138,139]. It can be explained because the thickness of the FeB layer is larger than the exchange coupling length of FePt, $l_{ex} = \sqrt{A/K_u} \approx 4\text{nm}$, where $A=1\times 10^{-6}\text{erg/cm}$ is the stiffness of FePt, and K_u is the anisotropy constant $7\times 10^6\text{erg/cm}^3$. [130-140-141]. Figure 6.9 (b) shows M-H loops of sample series E with FeB-added layers after annealing at 400°C for 30 min. Annealing smoothed the M-H loop of the sample with 5nm FeB addition, which suggested improved coupling between FeB and FePt. No significant changes were observed for the 10nm FeB addition while the coercivities were increased slightly for FeB layers thicker than 10 nm.

6.3.3 Exploring Conditions for Fe/Pt Multilayers

In order to investigate the properties of Fe/Pt multilayers, a series of samples with different thickness and configuration were deposited and annealed [37,40]. Figure 6.10 and 6.11 show the M-H loops of sample series F and G with the same total thickness but deposited by different techniques. Sample series F with a stack of $[Fe0.47/Pt0.4]_{12}$ consisted of coarse multilayers, while sample series G with a stack of $[Fe0.043/Pt0.036]_{11x12}$ consisted of finely multilayered or composite films. As the annealing time increased, the loops became wider, which means the films became magnetically harder.[143] The in-plane H_c increased from tens of Oe to 1.0 kOe and out-of-plane H_c increased to 1.4 kOe. However, the in-plane loop was much squarer than the out-of-plane loop. The easy axis of magnetization was in-plane. Similar to what were observed for sample series A and B, sample series G, with finely multilayered films showed higher coercivities than those of sample series F with coarse multilayered films, due to less interdiffusion distance and better intermixing of Fe and Pt atoms during annealing. [40,121].

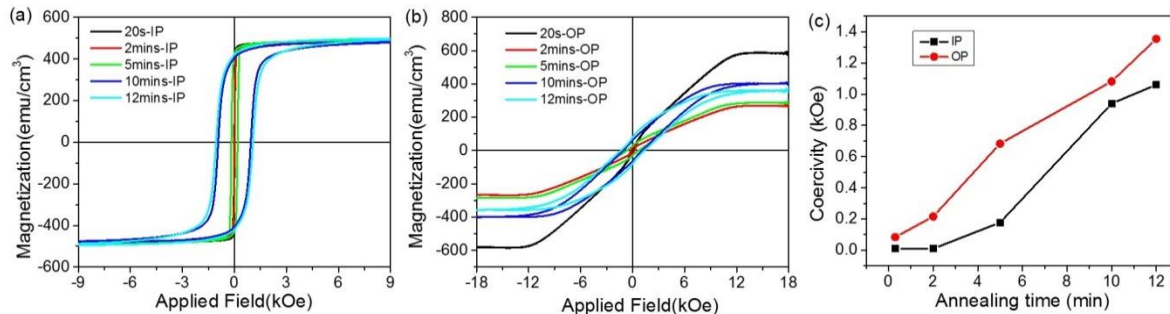


Figure 6. 10 (a) In-plane and (b) out-of-plane M-H loops of sample series F with stack of $[Fe0.47/Pt0.4]_{12}$ lamp annealed at 550°C for 20s~12 min; (c) coercivities vs. annealing time.

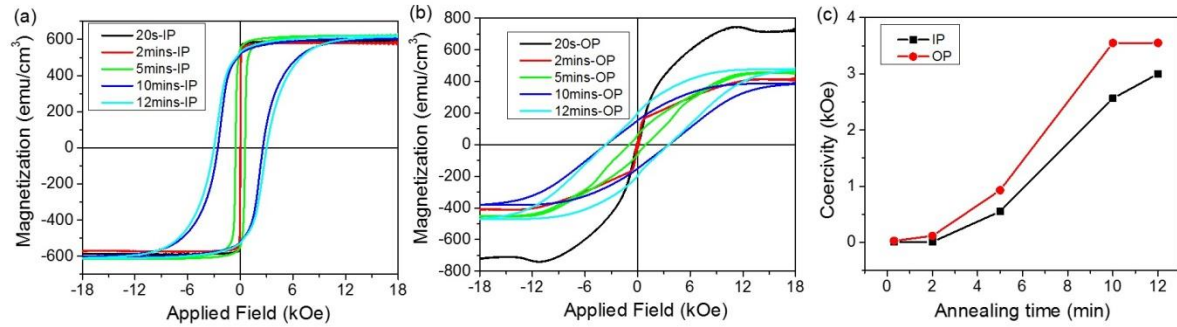


Figure 6.11 (a) In-plane and (b) out-of-plane M-H loops of sample series G with stack of $[Fe_0.043/Pt0.036]_{11\times12}$, lamp annealed at 550°C for 20s-12 min ; (c) dependence of coercivities on annealing time.

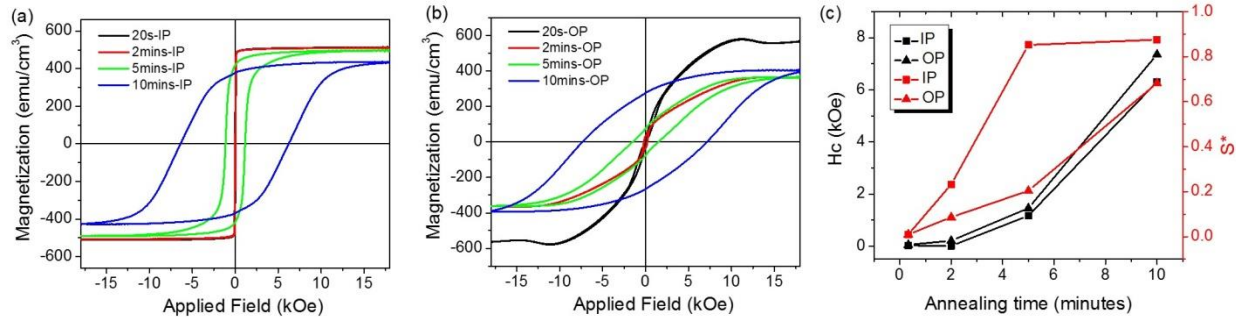


Figure 6.12 (a) In-plane and (b) out-of-plane M-H loops of sample series H with a stack of $Fe_3/Pt3/[Fe0.47/Pt0.4]_{12}$, lamp annealed at 550°C for 20s~12 min by RTA; (c) dependence of coercivities on annealing time.

Figure 6.12 (a) and (b) show the M-H loops of sample series H which have similar stacks as sample F but with a seed layer of Fe3/Pt3, and the dependence of H_c and S^* were plotted in Figure 6.12 (c). In-plane and out-of-plane coercivities increased with increasing annealing time, indicating that ordering occurred. The in-plane coercivities were slightly smaller than those out-of-plane, while S^* showed the opposite trend. [123, 143]. It was noted that the shapes of the hysteresis loops for the sample annealed at 550°C for 10 min were similar for both in-plane and out-of-plane. This effect may result from the presence of grains with different crystallographic orientations, the majority of which have their easy axis between in-plane and normal to the plane. [143]. Comparing Figure 6.11 with Figure 6.9, one may notice that H_c for sample H is much larger

than that of sample F under the same annealing conditions, due to the ordering promoted by the seed layers Fe 3nm/Pt3nm. [40].

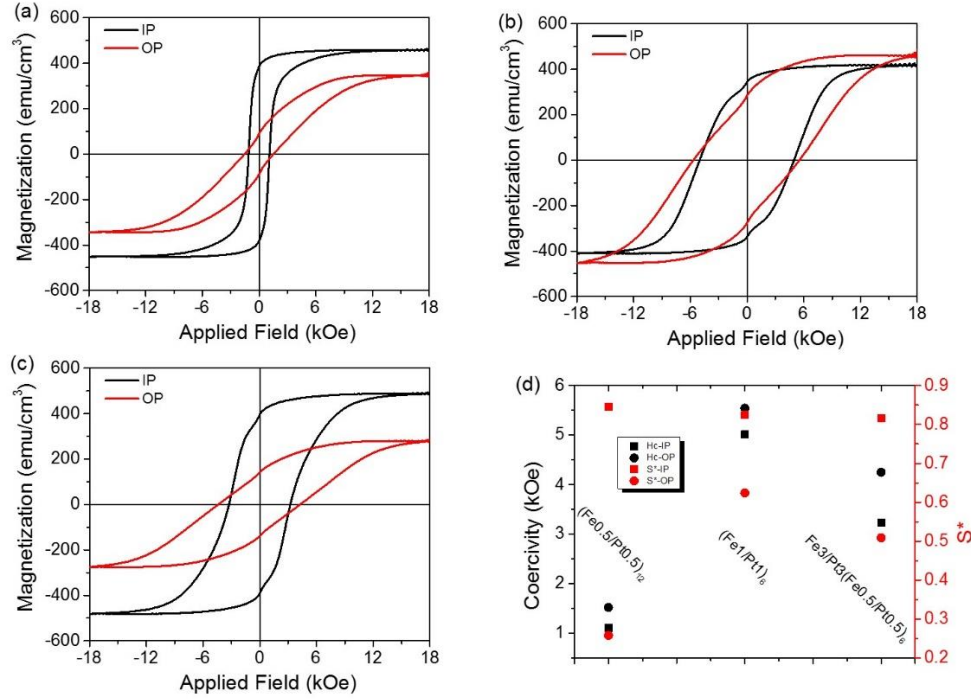


Figure 6. 13 M-H loops of samples with the same thickness but different configurations annealed at 550°C for 5 min by RTA. (a) sample I: $[Fe0.5/Pt0.5]_{12}$; (b) sample J: $[Fe1/Pt1]_6$, and (c) sample K : $Fe3/Pt3/[Fe0.5/Pt0.5]_6$. (d) The plot compares the H_c and S^* of samples I, J and K.

Figure 6.12 shows M-H loops of samples with the same total thickness but different bilayer configurations annealed at 550°C for 5 min by RTA, (a) sample I: $[Fe0.5/Pt0.5]_{12}$, (b) sample J: $[Fe1/Pt1]_6$, and (c)sample K : $Fe3/Pt3/[Fe0.5/Pt0.5]_6$. It can be seen that all the samples showed some extent of ordering, since the coercivities were 1 kOe and above, while the coercivities for as-deposited samples were only tens of Oe. Sample J showed the highest coercivity for both in-plane and out-of-plane loops, although sample K had a seed layer of Fe3nm/Pt3nm. Ogata et al. demonstrated that [Fe3 nm/ Pt3nm] layer beneath the $[Fe1/Pt1]_3$ multilayer as a seed layer promoted the attainment of perpendicular magnetic anisotropy [40]. In our case, it seems that a

simple [Fe1/Pt1] seed layer may be good enough to promote the ordering of FePt during the annealing.

6.4 Conclusions

A detailed study of Fe(B)Pt films sputter-deposited by two different techniques to produce coarse and atomically fine layered structures has been carried out. The dependence of microstructure and magnetic properties of the multilayered film on annealing time, annealing temperature and film thickness were discussed. Annealing these samples at various times and temperatures has produced L1₀ ordering in both types of stacks. However, the ordering is much more pronounced for the atomically fine layered structure, as evidenced by the XRD and magnetometry studies. This can be attributed to the smaller diffusion length in the atomically fine layered sample. This is a significant result, and we can further explore it by going to higher rotation speeds during co-deposition to achieve even finer layers for improved atomic intermixing. It was more difficult to form the L1₀ phase for samples with lower total thickness, compared with thicker samples of the same composition, under the same annealing conditions, as evidenced by the magnetic properties.

For exchange coupled composites, FeB layers thinner than 5nm were coupled with L1₀-FePtB which were pre-annealed, whereas the samples with thicker FeB layers did not show single-step switching behavior. Annealing at 400°C for 30 min did not improve the coupling effect significantly.

For Fe/Pt multilayered films, samples with finer alternating layers yield higher coercivities than samples with coarse layers, for specific thicknesses without seed layers. The sample with [Fe1/Pt1]₆ showed the highest coercivity, which may be a result of the [Fe1/Pt1] layer being thick

enough to serve as a seed layer. Further annealing is desired as coercivities for these samples showed continual increase with annealing time.

Further work will include the optimization of annealing conditions, addition of a third element or oxide to segregate the FePt grains.

Chapter 7 FeBPt Patterned by Block Copolymer Lithography

7.1 Introduction

In order to solve the “trilemma” of perpendicular magnetic recording, heat assisted magnetic recording (HAMR) and bit patterned media (BPM) have been proposed and studied [4,8,9,13-46,42]. In a BPM, one bit of information is stored in a single island of magnetic material. The space between them makes these nanodots naturally exchange decoupled [9, 42]. Co/Pd multilayers patterned by block copolymers (BCP) have been demonstrated as a BPM with areal density of 1Tb/in² [50,51]. To reach higher areal density, higher magnetic anisotropy materials are required. L1₀ FePt with K_u as high as 7x10⁷ erg/cm³ is one of the most promising candidates [4, 7]. Recently, a concept combining HAMR and BPM has attracted much attention [139,144]. A theoretical study predicted that, for such a HAMR-BPM system, the maximum possible areal density range could reach 20 ~ 100 Tb/in² using FePt-X media, and even up to 300 Tb/in² using SmCo media [145-148].

Based on our work on BPM and FePt described in the previous chapters [149], we carried out a study of patterning FeB/Pt multilayers over a range of etch conditions before and after annealing to form an ordered FePtB alloy.

7.2 Experiments

All depositions were carried out on thermally oxidized silicon substrates in a seven-target SFI Shamrock planetary sputtering system, using dc magnetron sputtering for all the layers. An infrared lamp array was placed in one of the target positions. The base pressure prior to deposition was 5 x 10⁻⁸ Torr. Depositions were carried out utilizing high purity three-inch diameter Fe₈₀B₂₀, Fe, Pt and Ta targets, sputtered at power levels of 103-311 W, corresponding to deposition rates ranging from 0.02-0.083 nm/s. The Ar sputtering pressure was maintained at 2 mTorr. The first

series of FeB/Pt multilayered films with a stack of FeB 4/Pt 5/[FeB0.9/Pt1.0]_{x15}/Ta5 nm were *in situ* lamp annealed at 550°C for 30 min. Then they were patterned by the BCP templating method using PFS-PS which was also detailed in Chapter 4. Filtered PS-*b*-PFS solutions (1.5 wt. % in toluene) were spin-coated on magnetic films at a speed of 400rpm-6s-4000 rpm-10s and then annealed at 140 °C for 48 hours. The annealing caused formation of PFS spheres in a PS matrix. Then the PS was mostly removed using a reactive ion etch system with an oxygen plasma at a power of 350 W and a pressure of 17 mTorr to expose the PFS spheres as an etch mask. The patterns were transferred to the magnetic films by ion milling. Here we used Ar⁺ milling in an Intevac system using an 8 cm Veeco ion source. The beam voltage was set at 200V, with the beam current at 65.4 mA. The angle of the ion beam to the substrate surface was varied from 55° to 85° in 10° increments, and etch times were varied from 2 minutes to 5 minutes in 1 minute increments. The patterned samples were treated in an O₂ plasma in a plasma ash at a power of 50 W to remove the residual organics before they were annealed at 600°C for 1 hr in a vacuum furnace with a pressure of about 5 x 10⁻⁵ torr. Another series of simultaneously sputtered or finely multilayered samples with a stack of FeB 4/Pt 4/[FeB0.09/Pt0.09]_{11x10}/Pt 4 (thickness in nm) were annealed at 600°C for 1 hr to form an ordered FePt structure, and then were patterned by BCP with the same procedure.

The morphology of the patterned samples was imaged by scanning electron microscopy (SEM) on a JEOL F7000 FEG-SEM. The crystal structure of the films was analyzed by a Philips X'Pert X-ray diffractometer (XRD) with CuK α radiation. The magnetic properties were measured at room temperature by a Princeton PMC Micromag 2000 alternating gradient force magnetometer (AGM) with a maximum applied field of 18 kOe.

7.3 Results and Discussion

7.3.1 Series 1: Annealing to Form FeBPt after Patterning

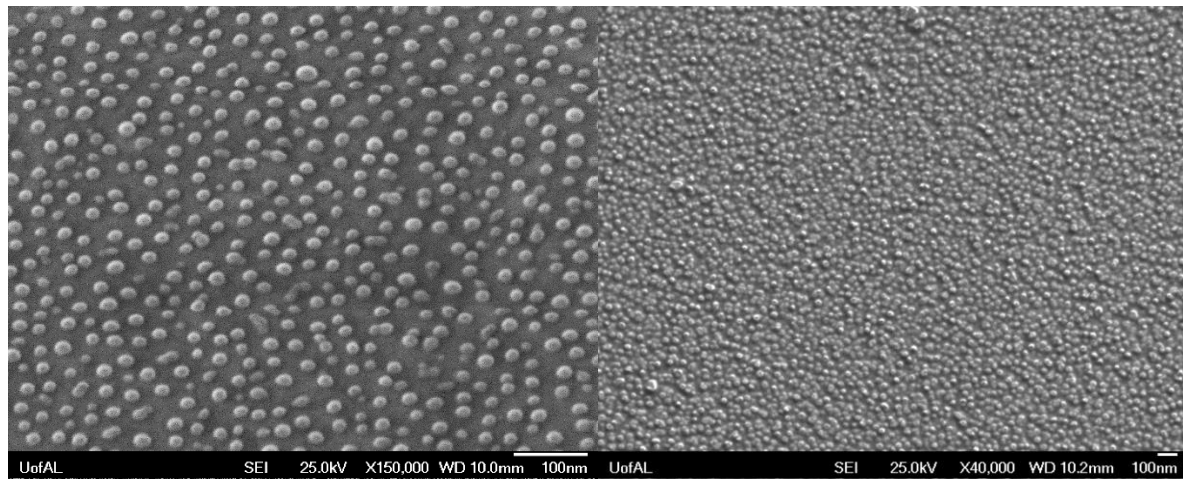


Figure 7. 1 Tilted view SEM (at about 45°) of (a) PFS nanospheres and (b) FeBPt nanopillars after ion milling at 55° for 5min.

Figure 7.1 (a) shows that a monolayer of PFS nanospheres with diameters of about 20 nm have been formed and exposed after removal of the PS matrix by the O₂ plasma, as noted in Chapter 4. A typical SEM of nanopatterned thin films is shown in Figure 7.1 (b). The diameter is about 30 nm, larger than that of the PFS nanospheres, which may result from self-shadowing effect during the ion-milling process.

M-H loops of the continuous film and those patterned by ion-milling at 55° to 85° for 2 to 5 minutes are shown in Figure 7.2 for comparison. It can be seen that, except for the sample milled at 85° for 5 min, all other milled samples show enhancement of coercivity. It appears that an etch time of 3 min. was the optimal etch time for all the etch angles tested, while 75° was the best milling angle for all the etch times. This can be seen more clearly in the contour plot of coercivity as functions of etch time and etch angle in Figure 7.3. The reason that the sample milled at 85° for 5 minutes (near-normal incidence and longest etch time) had the lowest coercivity is that the PFS nanospheres were etched away and the nanopillar features were smoothed out, as shown in Figure 7.4.

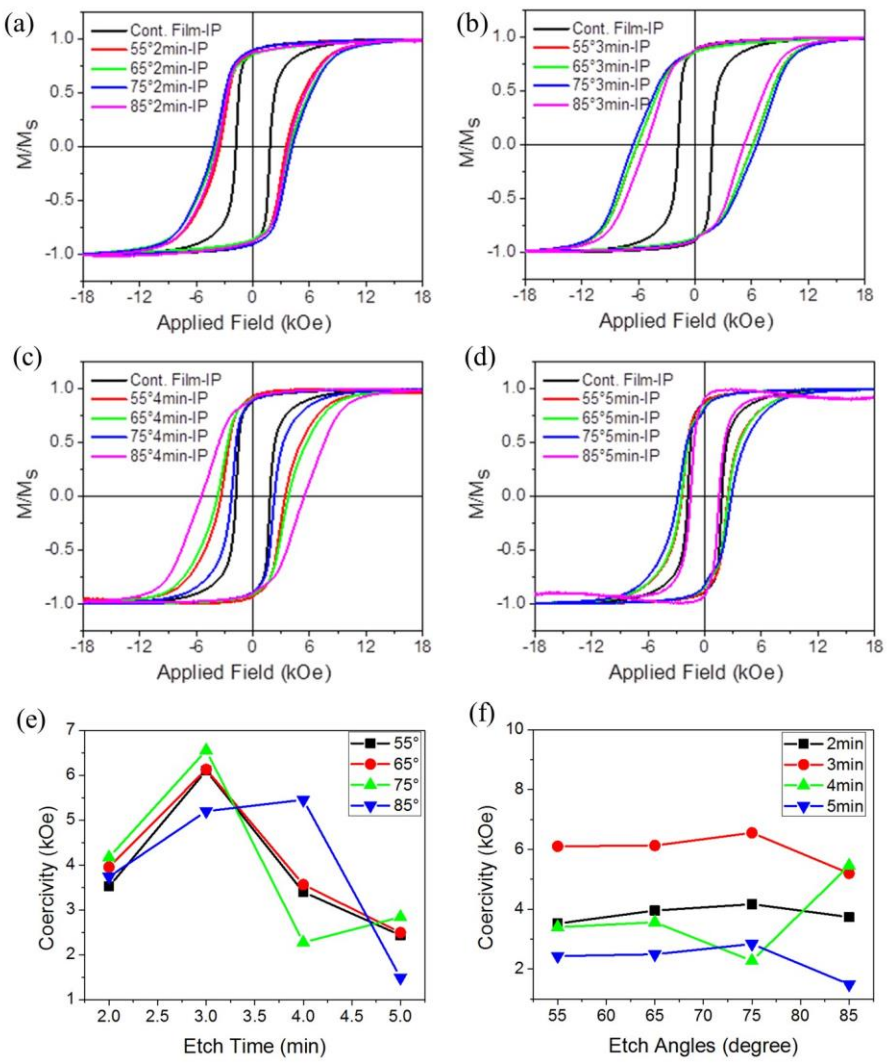


Figure 7. 2 M-H loops of FeB Pt ion milled at 55°, 65°, 75° and 85° for (a) 2 min, (b) 3 min, (c) 4 min, and (d) 5 min. The coercivity, H_c , was plotted as functions of (e) etch time and (f) etch angle.

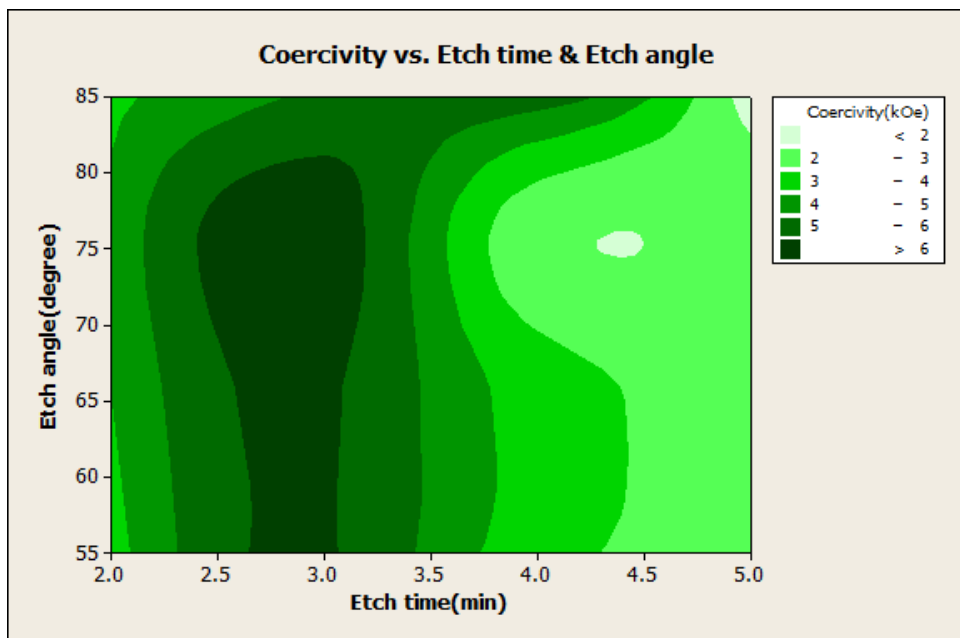


Figure 7. 3 Contour plot of coercivity of FeBPt as functions of etch time and etch angle

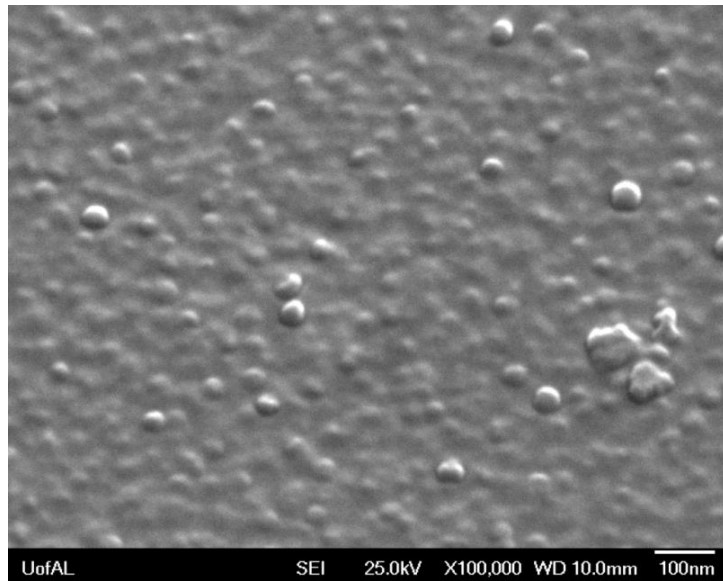


Figure 7. 4 SEM image of FeBPt after ion milling at 85° for 5min.

The samples ion milled at, 65° , 75° and 85° for 3 minutes were annealed at 600°C for 1 hr.

As can be seen in Figure 7.5, H_c increased from 1.8 kOe to 10.8 kOe for continuous films and 13.5 kOe for patterned films. Figure 7.6 shows the XRD spectra of the continuous film and the 55° , 3 min. patterned sample after annealing. It may be observed that both the continuous and patterned

samples show (111) peaks with similar intensity, indicating that there was little or no damage to the sample, or that the damage has been reversed by annealing at high temperature [144, 150].

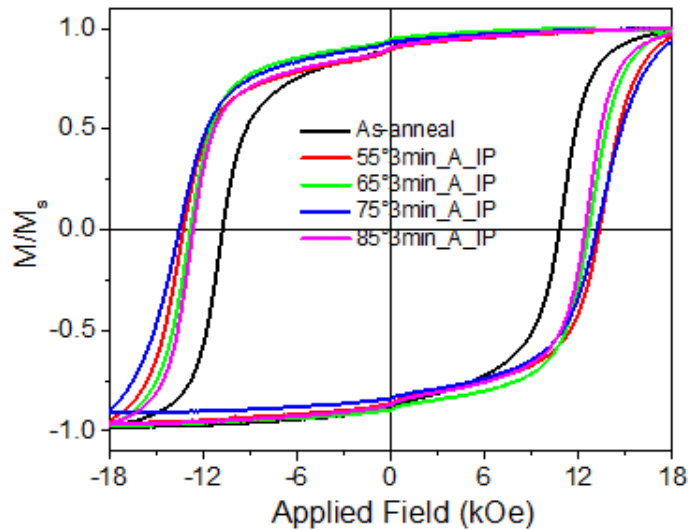


Figure 7.5 M-H loops of FeBPt samples ion-milled for 3min at 55°~85° and annealed 600°C for 1hr.

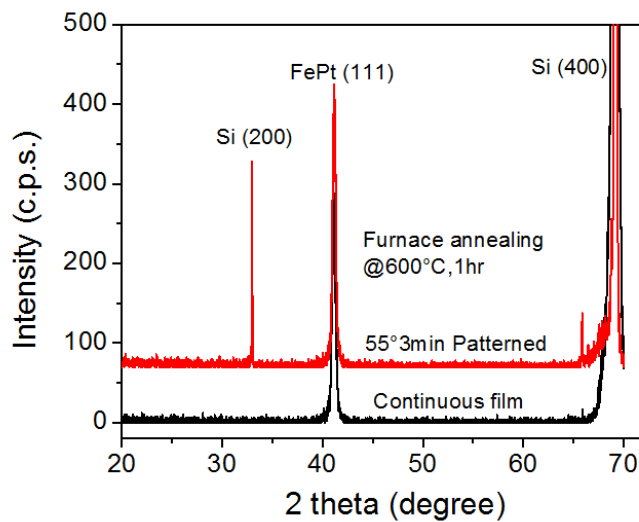


Figure 7.6 XRD spectra of continuous film and patterned sample being annealed 600°C1hr

7.3.2 Series 2 Annealing to Form FeBPt before Patterning

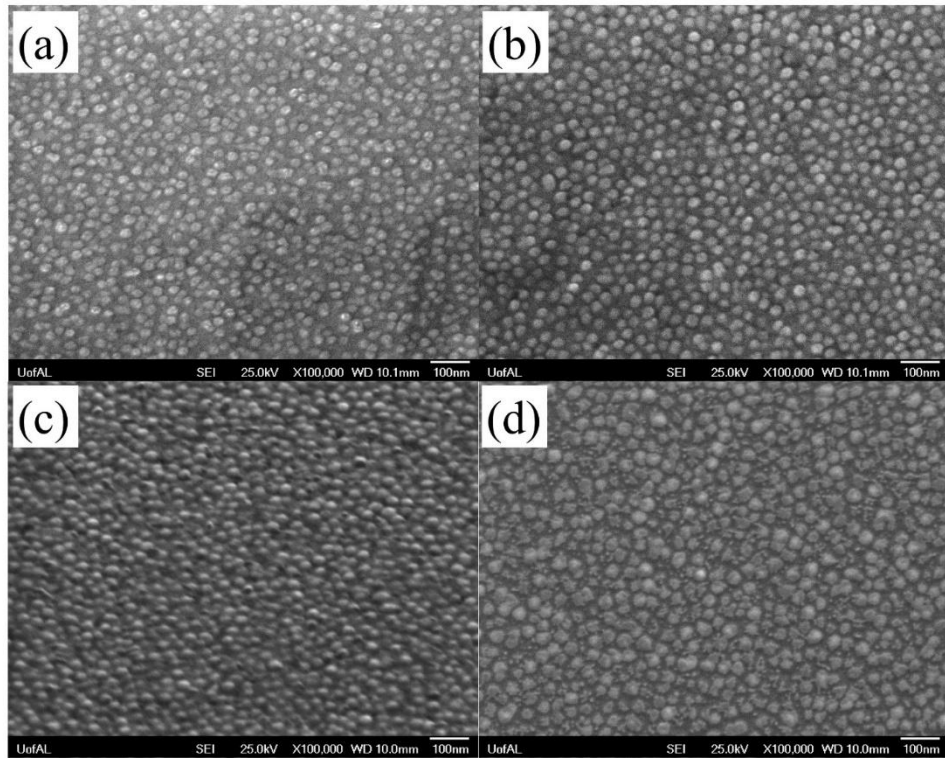


Figure 7.7 45° tilted view SEM images of FeBPt ion-milled at 55° for (a) 2 min, (b) 3min, (c) 4min, and (d) 5min.

Figure 7.7 shows the morphology evolution as a function of etch time. It may be seen that the nanopillars were formed gradually. The diameter of the nanopillars increased from 25 nm to about 34 nm with increasing etch time from 2 min to 4 min. However, further increasing the etch time to 5 min. seemed to cause severe damage to the sample as seen in Figure 7.7 (d).

Figure 7.8 shows the XRD spectra of these samples ion-milled as well as the continuous film. The continuous film showed (111) textured FePt and no other film peaks were observed in the scanning range of 24° to 72° except the substrate peaks of Si (200) and (400). The intensities of (111) peaks decreased with increasing etch time. After 4 min etch, the (111) peak became broadened and weak. An additional one minute etch removed the peak completely. These are the results of ion milling damage, which are also reported in the literature [144, 150].

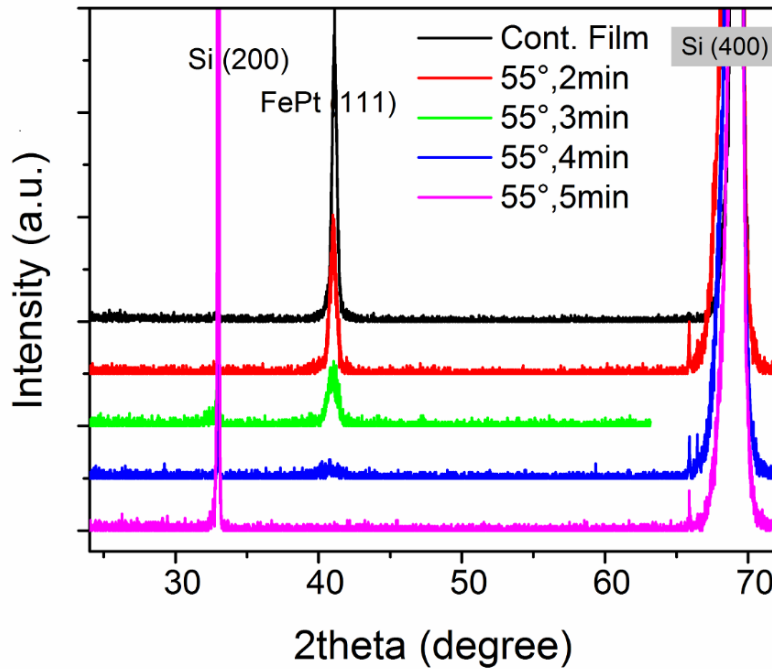


Figure 7. 8 XRD spectra of FeB Pt continuous film and those ion-milled at 55° for 2~5min

Magnetic properties of these samples were examined by M-H loops measured by AGM, as shown in Figure 7.9. The continuous FeB Pt film showed a coercivity as high as 13.8 kOe for both in-plane and out-of-plane loops. It may be observed that the out-of-plane magnetization is smaller than the in-plane value, indicating that the out-of-plane loop is not saturated at 18kOe, the maximum field available for the AGM. M_{st} values decreased with increasing the milling time since the ion milling patterned (removed magnetic material) as well as damaged the films. For the sample etched for 4 min, the in-plane H_c decreased to 7.9 kOe while the out-of-plane H_c decreased to 9.8 kOe. Further milling the degraded magnetic properties completely. It has been reported that this damage during ion-milling is reversible and the coercivity can be increased after post-patterning annealing [150]. Re-annealing and characterizing these patterned samples will be carried out in the future.

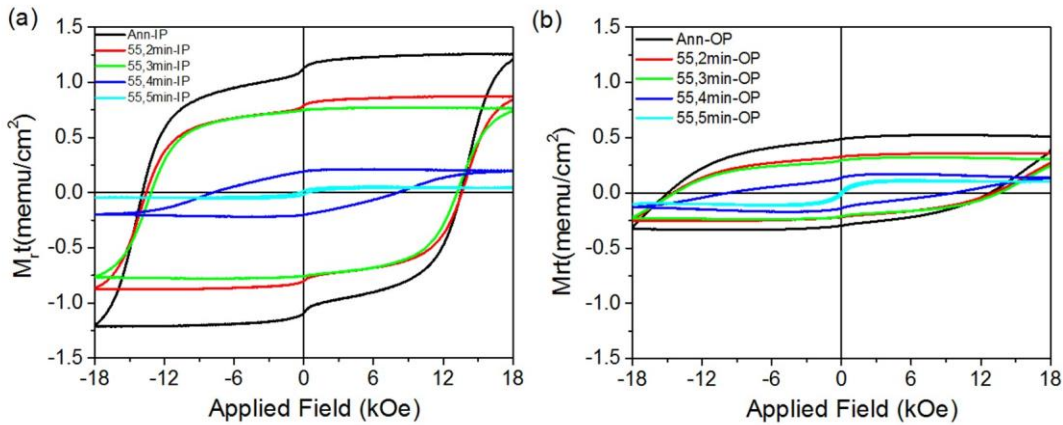


Figure 7.9 (a) In-plane and (b) out-of-plane of M-H loops of FeB/Pt ion-milled at 55° for 2, 3, 4 and 5minutes.

7.4 Conclusions

In this chapter, FeB/Pt films deposited by simultaneous sputtering were annealed before or after patterning by block copolymer templating.

For Series 1, the films were *in situ* lamp annealed at 550°C for 30 min and then patterned by ion-milling the thin films with PFS nanospheres as etch masks. The coercivity increased for all the patterned samples except the one milled at 85° for 5 min. For this sample, the nanopillar features appeared smoothed out, probably caused by removal of the PFS mask during milling. The post-patterning vacuum furnace annealing increased the coercivity to about 14 kOe, which may be a result of reversing the damage caused by milling.

For Series 2, the films annealed at 600°C for 1hr were also successfully patterned by the same techniques. SEM images, XRD spectra and magnetometry showed that the films have been damaged by ion-milling. Post etch annealing is known to reverse ion milling damage, and these experiments will be conducted in the future.

Chapter 8 Conclusions and Future Work

In this dissertation, a study of magnetic multilayers of Co/Pd, FeB/Pt, and Fe/Pt was carried out as a function of growth conditions, nanopatterning processes, and annealing conditions. The goal was to research high coercivity, high perpendicular anisotropy nanostructured media for data storage applications.

8.1 Conclusions

1. A systematic study has been carried out to investigate the effects of Co thickness, Pd thickness, Co/Pd thickness ratio, seed layers and number of bilayers on the magnetic properties of Co/Pd multilayers (MLs). The magnetic properties can be tuned and optimized by varying these parameters. A seed layer of Ta 5/Pd 5 nm was found to promote the most strongly textured fcc (111) Co/Pd MLs, which is known to be responsible for the perpendicular magnetic anisotropy of these MLs. With this seed layer, Co/Pd MLs with t_{Co} 0.2~0.45 nm and t_{Pd} 0.4~1.2 nm showed high perpendicular anisotropy with narrow switching field distribution. With the same total thickness of Co and Pd, magnetic properties depended not only on the number of bilayers but also on each individual layer thickness.

2. Conditions of nanopatterning Co/Pd perpendicular multilayers and CoPt alloy by nanosphere lithography (NSL) and block copolymer lithography (BCP) were optimized using a statistical Design of Experiments. NSL was found not to be a practical means of patterning media, since it was very difficult to get a uniform array of less than 40 nm diameter nanopillars over a large area. Block copolymer templating, utilizing ion milling for etching the magnetic layers, was an effective method for patterning the magnetic film uniformly over a large area. Co/Pd bit patterned media (BPM) with a nanopillar size of 31 nm and size distribution of 9.5% has been successfully fabricated by this method, showing coercivity as high as 6.6kOe. Annealing the

samples improved the magnetic properties for both continuous films and patterned ones, with the highest coercivity achieved being 2.9 kOe for a patterned film, a 93% increase over the as-etched film.

3. A single-step process for fabricating magnetic Co/Pd and FeB/Pt multilayered nanorods for advanced media was experimentally demonstrated by glancing angle deposition (GLAD). This is a novel and much more efficient means of producing nanostructured media than multiple-step patterning. Nanorods of CoPt-AlN with a diameter of ~16 nm formed by GLAD showed increased perpendicular magnetic anisotropy compared with flat films. On the bare silicon substrate, Co/Pd multilayered nanorods with dimensions of $31\text{ nm} \pm 3\text{ nm}$ in height, about 12 nm $\pm 2\text{ nm}$ in diameter, with about 2 nm spacing, have been fabricated. The coercivity increased from 1.3 kOe for normally deposited flat films to 2.9 kOe for the GLAD nanorods, a 123% increase. On a silicon substrate, using PFS nanospheres as a template, a dense, periodic array of 40 nm diameter Co/Pd multilayered nanorods were formed by GLAD. FeB/Pt multilayered and FeBPt composite nanorods, with a diameter of 11 nm, have been fabricated. Further optimization and characterization is being conducted on these.

Co nanorods formed by stationary GLAD were found to be larger in diameter than those of samples by planetary GLAD under the same power and deposition time. The difference resulted from the huge difference in the deposition rates, a factor of about 10. It also demonstrates that the size of the nanorods will increase if the nanorods grow long enough.

4. A detailed study of Fe(B)Pt films sputter-deposited by two different techniques to produce coarse and atomically fine layered structures has been carried out. The dependence of microstructure and magnetic properties of the multilayered film on annealing time, annealing temperature and film thickness was discussed. Annealing these samples at various times and

temperatures has produced L₁₀ ordering in both types of stacks. However, the ordering is much more pronounced for the atomically fine layered structure, as evidenced by the XRD and magnetometry studies. This can be attributed to the smaller diffusion length in the atomically fine layered sample. This is a significant result, and we can further explore it by going to higher rotation speeds during co-deposition to achieve even finer layers for improved atomic intermixing. It was more difficult to form the L₁₀ phase for samples with lower total thickness, compared with thicker samples of the same composition, under the same annealing conditions, as evidenced by the magnetic properties.

For exchange coupled composites, FeB layers thinner than 5nm were coupled with L₁₀-FePtB which were pre-annealed, whereas the samples with thicker FeB layers did not show single-step switching behavior. This demonstrated that we can fabricate exchange coupled composite media when we deposit thin FeB layer on top of ordered FePt.

For Fe/Pt multilayered films, samples with finer alternating layers yield higher coercivities than samples with coarse layers, for specific thicknesses without seed layers. [Fe1 nm /Pt1 nm] layer can serve as a seed layer to promote the ordering of FePt. Further annealing above 650°C is desired as coercivities for these samples showed continual increase with annealing time.

FeBPt BPM have also been fabricated by patterning magnetic hard FePtB with BCP and ion milling at various angles and times. These experiments have been conducted in two ways: 1) patterning nanopillar and then furnace annealing; 2) furnace annealing the FeBPt films prior to patterning.

8.2 Future Work

There are still many topics of interest remaining for further study.

1. Co/Pd BPM by BCP: The ordering of the nanopillars was not high enough to be applicable to industry. A templated or directed block copolymer assembly will be of importance to attain high uniformity of nanopillar arrays.
2. FePt: Further work will include the optimization of annealing conditions to obtain the highly ordered and fully perpendicular L₁ phase FePt. Addition of a third element or oxide to segregate the FePt grains will be attempted.
3. Fe(B)Pt by GLAD: Further optimization is being conducted. Stationary GLAD using FePt alloy target may be a choice. Higher annealing temperatures are required to achieve perpendicular magnetic anisotropy.

References

1. <http://www.magneticdiskheritagecenter.org/MDHC/RAMACBrochure.pdf>
2. R. H. Victora, X. Shen, *IEEE Trans. Magn.* **41**, 537 (2005).
3. D. Suess, T. Schrefl, M. Kirschner, G. Hrkac, F. Dorfbauer, O. Ertl, J. Fidler, *IEEE Trans. Magn.* **41**, 3166(2005).
4. S. N. Piramanayagam, K. Srinivasan, *J. Magn. Magn. Mater.* **321**, 485 (2009).
5. R. Wood, *J. Magn. Magn. Mater.* **321**, 555 (2009).
6. http://www.wdc.com/wdproducts/library/company/investor/PDF_4_Cain_Munce_FINAL.pdf
7. http://www.semicon.toshiba.co.jp/product/storage/pdf/ToshibaReview_vol66n8_02.pdf
8. H. J. Richter, *J. Phys. D: Appl. Phys.* **40**, R149 (2007).
9. D. Goll, T. Bublat, *physica status solidi (a)*, **210**, 1261(2013).
10. R. F. L. Evans, R. W. Chantrell, U. Nowak, A. Lyberatos and H.-J. Richter, *Appl. Phys. Lett.* **100**, 102402 (2012).
11. R. Wood, M. Williams, A. Kavcic and J. Miles, *IEEE Trans. Magn.*, **45**, 917(2009).
12. S. Greaves, Y. Kanai and H. Muraoka, *IEEE Trans. Magn.*, **45**, 823(2009).
13. M. H. Kryder, E. C. Gage, T. W. McDaniel, W. A. Challener, R. E. Rottmayer, G. Ju, Y.-T. Hsia, and M. F. Erden, *Proc. IEEE* **96**, 1810 (2008).
14. H. J. Richter, A. Y. Dobin, O. Heinonen, K. Z. Gao, R. J. M. v. d. Veerdonk, R. T. Lynch, J. Xue, D. Weller, P. Asselin, M. F. Erden, and R. M. Brockie, *IEEE Trans. Magn.* **42**, 2255 (2006).
15. D. Weller, A. Moser, L. Folks, M. E. Best, W. Lee, M. F. Toney, M. Schwickert, J.-U. Thiele, and M. F. Doerner, *IEEE Trans. Magn.* **36**, 10 (2000).
16. J. S. Chen, C. J. Sun, and G. M. Chow, *Int. J. Prod. Dev.*, **5**, 238. (2008).
17. Y. K. Takahashi, M. Ohnuma and K. Hono, *J. Magn. Magn. Mater.*, **246**, 259(2002).
18. C. L. Platt, K. W. Wierman, E. B. Svedberg, R. van de Veerdonk, J. K. Howard, A. G. Roy, and D. E. Laughlin, *J. Appl. Phys.* **92**, 6104 (2002).
19. K. Nishimura, K. Takahashi, H. Uchida and M. Inoue, *J. Magn. Magn. Mater.*, **272-274**, 2189(2004).

20. C.Y. You, Y.K.Takahashi and K. Hono, *J. Appl. Phys.*, **100**, 056105(2006).
21. B. Wang, K.Barmak and T.J.Klemmer, *IEEE Trans. Magn.*, **46**, 1773(2010).
22. Y.M. Lee, B.S. Lee, C.G.Lee, H.H. Koo and Y. Shimada, *J. Magn. Magn. Mater.*, **10**, e918 (2007).
23. S.U.Jang, J.H. Him, *Microelectronic Engr.* **88**, 589(2011).
24. B.-H Li, C. Feng and T. Yang, *J. Phys. D: Appl. Phys.* **39**, 1018(2006).
25. R. K. Dumas, C. Zha and Y. Fang, *IEEE Trans. Magn.* **47**, 1580(2011).
26. C. Brombacher, H. Schletter and M. Daniel, *J. Appl. Phys.* **112**, 07392(2012).
27. D. A. Gilbert, L.-W. Wang, and T. K. Klemmer, et al, *Appl. Phys. Lett.* **102**, 132406(2013).
28. S. D. Granz, K. Barmak and M. H. Kryder, *Eur. Phys. J.B*, **86**:81(2013).
29. R.V. Chepulkii and S. Curtarolo, *Appl. Phys. Lett.* **97**, 221908 (2010).
30. J. C. Lodder, and L.T. Nguyen, (2005) FePt Thin Films: Fundamentals and Applications. In: Encyclopedia of Materials: Science and Technology. Elsevier, Amsterdam, pp. 1-10. ISBN 9780080431529.
31. E. Yang and D. E. Laughlin, *J. Appl. Phys.* **104**, 023904(2008).
32. E. Yang, H. Ho, D. E. Laughlin and J.-G Zhu, *J. Appl. Phys.* **111**, 07B720(2012).
33. H. Ho, E. Yang, D. E. Laughlin and J.-G Zhu, *Appl. Phys. Lett.* **102**, 112411(2013).
34. A. Perumal, Y .K. Takahashi and K. Hono, *Appl. Phys. Express*, **1**, 101301(2008).
35. B.S.D.Ch, S. Varaprasad, M. Chen, Y. K. Takahashi and K. Hono, *IEEE Trans. Magn.* **49**, 718 (2013).
36. L. Zhang, Y. K. Takahashi and K. Hono, et al, *IEEE Trans. Magn.* **47**, 4062(2011).
37. M. L. Yan, N. Powers and D. J. Sellmyer, *J. Appl. Phys.* **93**, 8292(2003).
38. Y.-C. Wu, L.-W. Wang and C.-H Lai, *Appl. Phys. Lett.* **91**, 072502 (2007).
39. D. H. Wei and C.H. Chao, *Nanosci. Nanotechnol. Lett.* **4**, 611(2012).
40. Y. Ogata, Y. Imai and S. Nakagawa, *J. Appl. Phys.* **107**, 09A715 (2010).
41. Y. Ding, D. H. Wei and Y. D. Yao, *J. Appl. Phys.*, **103**, 07E145(2008).
42. B. D. Terris and T. Thomson, *J. Phys. D: Appl. Phys.* **38**, R199 (2005)

43. X. Li, Z. R. Tadisina, G. Ju and S. Gupta, *J. Vac. Sci. Technol. A* **27**, 1062 (2009)
44. J. R. Jeong, S. Kim, S.H. Kim, J.A.C. Bland, S.C. Shin and S. M. Yang, *small*, **3**, 1529(2007)
45. D. Smith, V.Parekh, C. E, S. Zhang, W. Donner, T. R. Lee, S. Khizroev and D. Litvinov, *J. Appl. Phys.*, **103**, 023920(2008).
46. X. Yang, S. Xiao, W. Wu, Y. Xu, K. Mountfield, R. Rottmayer, K. Lee, D. Kuo, and D. Weller, *J. Vac. Sci. Technol. B* **25**, 2202(2007).
47. G. Hu, C.T. Tettner, T. Thomson, M. Albrecht, S. Raoux, G. M. McClelland, M. W .Hart, M. E. Best, and B. D. Terris, *J. Appl. Phys.* **95**, 7013 (2004)
48. J. Y. Cheng, C. A. Ross, E.L.Thomas H. I. Smith, and G. J. Vancso. *Adv. Mater.***15**, 1599(2003)
49. J. Y. Cheng, F. Zhang, H. I. Smith, G. J. Vancso, and C. A. Ross, *Adv. Mater.* **18**, 597(2006);
50. O. Hellwig, T. Hauet, T. Thomson, E. Dobisz, J. D. Risner-Jamtgaard, D. Yaney, B. D. Terris, and E. E. Fullerton, *Appl. Phys. Lett.* **95**, 232505(2009);
51. O. Hellwig, J. K. Bosworth, E. Dobisz, D. Kercher, T. Hauet, G. Zeltzer, J. D. Risner-Jamtgaard, D. Yaney and R. Ruiz, *Appl. Phys. Lett.* **96**, 052511 (2010)
52. K. Robbie and M. J. Brett, *J. Vac. Sci. Technol. A* **15**, 1460 (1997).
53. M. M. Hawkeye and M. J. Brett, *J. Vac. Sci. Technol. A* **25**, 1317 (2007).
54. T. Smy, D. Vick, M. J. Brett, S. K. Dew, A. T. Wu, J. C. Sit, and K. D. Harris, *J. Vac. Sci. Technol. A* **18**, 2507 (2000).
55. M. T. Taschuk, K. M. Krause, J. J. Steele, M. A. Summers, and M. J. Brett, *J. Vac. Sci. Technol. B* **27**, 2106 (2009).
56. A. Dolatshahi-Pirouz, D. S. Sutherland, M. Foss, and F. Besenbacher, *Appl. Surf. Sci.* **257**, 2226 (2011).
57. B. Dick, M. J. Brett, T. J. Smy, M. R. Freemen, M. Malac, and R. F. Egerton, *J. Vac. Sci. Technol. A* **18**, 1838 (2000).
58. J. Wang, H. Huang, S. V. Kesapragada, and D. Gall, *Nano Lett.* **5**, 2505 (2005).
59. K. Robbie, M. J. Brett, and A. Lakhtakia, *Nature* **384**, 616 (1996).
60. A. C. V. Popta, M. M. Hawkey, J. C. Sit, and M. J. Brett, *Opt. Lett.* **29**, 2545 (2004).
61. S. V. Kesapragada, P. Victor, O. Nalamasu, and D. Gall, *Nano Lett.* **6**, 854 (2006).

62. J. P. Singh, F. Tang, T. Karabacak, T. M. Lu, and G. C. Wang, *J. Vac. Sci. Technol. B* **22**, 1048 (2004).
63. F. Liu, M. T. Umlor, L. Shen, J. Weston, W. Eads, J. A. Barnard, and G. J. Mankey, *J. Appl. Phys.* **85**, 5486 (1999).
64. S. Thomas, S. H. Al-Harthi, I. A. Al-Omari, R. V. Ramanuja, V. Swaminathan, and M. R. Anantharaman, *J. Phys. D: Appl. Phys.* **42**, 215005 (2009).
65. A. K. Kar, P. Morrow, X. T. Tang, T. C. Parker, H. Li, J. Y. Dai, M. Shinma, and G. C. Wang, *Nanotechnology* **18**, 295702 (2007).
66. H. Su, A. Natarajarathinam and S. Gupta, *J. Appl. Phys.* **113**, 203901 (2013).
67. M. Ohring, Materials Science of Thin Films, 2nd edition, Academic Press, 2006.
68. <http://www.webzeest.com/article/511/thin-film-growth>
69. B. A. Movchan, A. V. Demchishin, *Phys. Met. Metallogr.* **28**, 83(1969)
70. J. A. Thornton, *Ann. Rev. Mater. Sci.* **7**, 239(1977)
71. Z. R. Tadisina, Ph.D. Dissertation, Tuscaloosa, AL(2010).
72. A. Natarajarathinam, Ph.D. Dissertation, Tuscaloosa, AL(2012).
73. J. Hopwood and T. D. Mantei, *J. Vac. Sci. Technol. A* **21**, S139 (2003).
74. http://mint.ua.edu/wp-content/uploads/2010/07/fall2007_48.pdf
75. <http://nanolab.berkeley.edu/labmanual/chap7/7.23sts-oxide.pdf>
76. <http://www.home.agilent.com/agilent/editorial.jspx?cc=US&lc=eng&ckey=1774141&nid=-33986.0&id=1774141>
77. B. D. Cullity, Elements of X-Ray Diffraction, 3rd edition, Prentice Hall (2002).
78. P. Scherrer, *Göttinger Nachrichten Gesell.*, **2**, 98(1918).
79. <http://mint.ua.edu/facilities/>
80. <http://encyclopedia2.thefreedictionary.com/x-ray+diffraction>
81. D. B. Williams, C. B. Carter, Transmission Electron Microscopy-A Textbook for Materials Science, 2nd edition, Springer (2009),
82. <http://www.pdx.edu/cemn/fib-gallery>

83. http://link.springer.com/referenceworkentry/10.1007%2F978-1-4020-4423-6_204/fulltext.html,
84. <http://www.teknik.uu.se/ftf/magnetism/bilder/magnetometer.gif>,
85. P. He, Z. S. Shan, J. A. Woollam and D.J. Sellmyer, *J. Appl. Phys.* **73**, 5954(1993);
86. T. Thomson, G. Hu, B. D. Terris, *Phys. Rev. Lett.* **96**, 257204(2006);
87. J. M. Shaw, H. T. Nembach, T. J. Silva, S. E. Russek, R. Geiss, C. Jones, N. Clark, T. Leo and D. J. Smith, *Phys. Rev. B*, **80**, 184419 (2009);
88. T. Koda, H. Awano, H. Hieda, K. Naito, A. Kikitsu, T. Matsumoto, K. Nakamura, and T. Nishida, *J. Appl. Phys.* **103**, 07C502 (2008);
89. Z. R. Tadisina, A. Natarajathinam, B .D .Clark, A. L. Highsmith, T. Mewes, S. Gupta, E. Chen and S. Wang, *J. Appl. Phys.* **107**, 09C703(2010);
90. A. Natarajathinam, R. Zhu, P. B. Visscher and S. Gupta, *J. Appl. Phys.* **111**, 07C918(2012);
91. B. Hu, N. Amos, Y. Tian, J. Butler, D. Litvinov, and S. Khizroev *J. Appl. Phys.* **109**, 034314 (2011);
92. S. Lee, S. Kim, J. Kang, J. Hong, *thin solid films*, **519**, 8363 (2011);
93. N. Kikuchi, Y. Murayama, Y. Murakami, S. Okamoto, D. Shindo and O. Kitakami, *Jpn.J.Appl. Phys.* **51**, 103002(2012);
94. S. Mohanan and U. Herr, *J. Appl. Phys.* **102**, 093903 (2007);
95. N. Thiagarajah, S. Bae, H. W. Joo, Y. C. Han and J. Kim, *Appl. Phys. Lett.* **92**, 062504 (2008);
96. A.S. H. Rozatian, C. H. Marrows, T. P. A. Hase and B. K. Tanner, *J. Phys.: Condens. Matter* **17**, 3759(2005);
97. R. Sbiaa, Z. Bilin, M. Ranjbar, H.K.Tan, S. J. Wong, S. N. Piramanayagam and T.C. Chong, *J. Appl. Phys.* **107**, 103901(2010);
98. G. Hu, T. Thomson, C. T. Rettner and B.D. Terris, *IEEE Trans. Magn.* **41**, 3589(2005).
99. J. M. Shaw, W. H. Rippard, S. E. Russek, T. Reith and C. M. Falco, *J. Appl. Phys.* **101**, 023909 (2007)
100. F. J. A. den Broeder, E. Janssen, W. Hoving and W. B. Zeper, *IEEE Trans. Magn.* **28**, 2760 (1992).
101. G. H. O. Daalderop, P. J. Kelly, and F. J. A. den Broeder, *Phys. Rev. Lett.* **68**, 682 (1992).

102. J. K. W. Yang, Y. Chen, T. Huang, H. Duan, N. Thiagarajah, H. K. Hui, S. Leong and V. Ng, *Nanotechnology* **22**, 385301 (2011).
103. C. L. Cheung, R.J. Nikolic, C. E. Reinhardt and T. F.Wang, *Nanotechnology*, **17**, 1339(2006);
104. Z. Sun, D. Li, A. Natarajarathinam, H. Su and S.Gupta, *J. Vac. Sci. Technol. B* **30**, 031803 (2012);
105. J. Fassbender, D. Ravelosona and Y. Samson, *J. Phys. D: Appl. Phys.* **37**, R179 (2004).
106. A. R. Neureuther, C. Y. Liu, and C. H. Ting, *J. Va. Sci. Technol.* **16**, 1767 (1979).
107. H. Yamane, Y. Maeno, M. Kobayashi, *Appl. Phys.Lett.* **62**, 1562 (1993).
108. W. F. Egelhoff, R. D. McMichael, J. J. Mallett, A. J. Shapiro, C. J. Powell et al.,*J. Appl. Phys.* **97**, 10J105 (2005).
109. <http://ecee.colorado.edu/~bart/book/mobility.htm>
110. M. Albrecht, G. Hu, I. L. Guhr, T. C. Ulbrich, J. Boneberg, P. Leiderer and G. Schatz, *Nat. Mater.* **4**, 203 (2005);
111. T. C. Ulbrich, D. Makarov,G. Hu, I. L. Guhr, D. Suess, T. Schrefl, and M. Albrecht, *Phys. Rev. Lett* **96**, 077202 (2006)
112. D. O. Smith, *J. Appl. Phys.* **30**, S264(1959)
113. T. G. Knorr and R.W. Hoffman, *Phys. Rev.* **113**,1039(1959)
114. B. Dick, M. J. Brett, T. Smy, M. Blov and M. R. Freemen, *J. Vac. Sci. Technol. B* **19**, 1813(2001).
115. S.R. Kennedy and M.J.Brett, *J. Vac. Sci. Technol. B* **22**, 1184(2004).
116. M. Backholm, M.Foss and K. Nordlund, *Nanotechnology*, 23,385708 (2012)
117. S. Kim, S. Lee, J. Kim, J. Kang and J. Hong, *J. Appl. Phys.* **109**,07B766(2011)
118. J.E. Davies, P.Morrow, C.L.Dennis, J.W.Lau, B.McMorran, A. Cochran, J.Unguris, R.K.Dumas, P.Greene and K. Liu, *J.Appl. Phys.*, 109 07B909(2011)
119. S. V. Kesapragada and D. Gall, *Thin Solid Films*, **494**, 234(2006)
120. R. A. Ristau, K. Barmak, L. H. Lewis, K. R. Coffey, and J. K. Howard, *J. Appl. Phys.* **86**, 4527 (1999).
121. S. Imada, A. Yamasaki, S. Suga, T. Shima, and K. Takanashi, *Appl. Phys. Lett.* **90**, 132507 (2007).

122. T. Ichitsubo, S. Tojo, T. Uchihara, E. Matsubara, A. Fujita, K. Takahashi and K. Watanabe, *Phys. Rev. B* **77**, 094114 (2008).
123. N. Zotov, J. Feydt, A. Savan, and A. Ludwig, *J. Appl. Phys.* **100**, 073517 (2006).
124. C. P. Luo, and D. J. Sellmyer, *IEEE Trans. Magn.* **31**, 2764(1995).
125. Y. Wang, P. Sharma and A. Makino, *J. Phys.: Condens. Matter.* **24**, 076004(2012).
126. Y. K. Takahashi, T. O. Seki, K. Hono, T. Shima and K. Takanashi, *J. Appl. Phys.* **96**, 475(2004).
127. B. Yao and K.R. Coffey, *J. Appl. Phys.* **105**, 033901(2009).
128. T. Kaiser, W. Sigle, D. Goll, N. H. Goo, V. Srot, P. A. van Aken, E. Detemple and W. Jäger, *J. Appl. Phys.* **103**, 063913 (2008).
129. J. Wang , B.Yang, W. Pei, G. Qin, Y. Zhang, C. Esling, X. Zhao, L. Zuo *J. Magn. Magn. Mater.* **345**, 165(2013).
130. F. Casoli, F. Albertini, L. Nasi, S. Fabbrici, R. Cabassi, F. Bolzoni and C. Bocchi, *Appl. Phys. Lett.*, **92**, 142506 (2008).
131. D. C. Berry, K. Barmak, *J. Appl. Phys.*, **99**, 08G901(2006)
132. K. Barmak, B. Wang, A. T. Jesanis, D. C. Berry, J. M. Rickman, *IEEE Trans. Magn.* **49**, 3284 (2013)
133. M. Albrecht and C. Brombacher, *Phys. Status Solidi A*, **210**, 1272(2013).
134. Y. H. Fang, P.C. Kuo, S. C.Chen, S. L.Hsu, G. P. Lin, *Thin Solid Films* **517**, 5185(2009)
135. L. Han, U Wiedwald, B. Kuerbanjiang, and P.Ziemann, *Nanotechnology*, **20**, 285706(2009)
136. M. E. Gruner, G. Rollmann, P. Entel, and M. Farle, *Phys. Rev. Lett.* **100**, 087203 (2008)
137. Y. Endo, N. Kikuchi, S. Kitakami, and Y. Shimada, *J. Appl. Phys.* **89**, 7065(2001).
138. H. H. Guo, H.G.Chu, B. Ma, Z.Z.Zhang, Q.Y. Jin, H.Wang and J. P. Wang, *Appl. Phys. Lett.* **102**, 252410(2013).
139. A. T. McCallum, P. Krone, F. Springer, C. Brombacher, M. Albrecht, E. Dobisz, M. Grobis, D. Weller and O. Hellwig, *Appl. Phys. Lett.* **98**, 242503 (2011).
140. F. Casoli, F. Albertini, S. Fabbrici, C. Bocchi, L. Nasi, R. Cabassi, and L. Paret, *IEEE Trans. Magn.* **41**, 3877(2005)

141. S. Okamoto, N. Kikuchi, O. Kitakami, T. Miyazaki and Y. Shimada, *Phys. Rev. B*, **66**, 024413(2002).
142. G Varvaro, F Albertini, E Agostinelli, F Casoli, D Fiorani, S Laureti, P Lupo, P Ranzieri, B Astinchap and A M Testa, *New J. Phys.* **14** 073008 (2012).
143. N. Zotov, R. Hiergeist, A. Savan and A. Ludwig, *thin solid films*, **518**, 4977(2010)
144. T. Bublat and D. Goll, *Nanotechnology*, **22** 315301(2011)
145. H. J. Richter, A. Lyberatos U. Nowak, R. F. L. Evans and R. W. Chantrell, *J. Appl. Phys.* **111**, 033909 (2012)
146. T.W. McDaniel, *J. Appl. Phys.* **112** 093920(2012)
147. T.W. McDaniel, *J. Phys.: Condens. Matter.* **17**,R315(2005)
148. R. A. Griffiths, A. Williams, C. Oakland, J. Roberts, A.Vijayaraghavan and T. Thomson, *J. Phys. D: Appl. Phys.* **46**, 503001(2013).
149. H. Su, S. C. Schwarm, R. L. Martens, S. Gupta, **115**, *J. Appl. Phys.* 17B717 (2014); H. Su, A. G. Owen, R. Douglas and S. Gupta, “Optimization of Co/Pd Multilayers Patterning by Block Copolymer Templating”, under review.
150. P. Tiberto, G. Barrera, L. Boarino, F. Celegato, M. Coisson, N. DeLeo, F. Albertini, F. Casoli, and P. Ranzieri. *J. Appl. Phys.* **113**, 17B516 (2013)